Nonlinear Response Theory of Active Brownian Particles

Inaugural-Dissertation

zur Erlangung des Doktorgrades

der Mathematisch-Naturwissenschaftlichen Fakultät

der Heinrich-Heine-Universität Düsseldorf

vorgelegt von

Marcel Unger

aus Düsseldorf

Cologne, October 2023

aus dem Institut für Theoretische Physik II weicher Materie
der Heinrich-Heine-Universität Düsseldorf

Gedruckt mit der Genehmigung der
Mathematisch-Naturwissenschaftlichen Fakultät der
Heinrich-Heine-Universität Düsseldorf

Berichterstatter:

1. Prof. Dr. Thomas Voigtmann

2. Prof. Dr. Hartmut Löwen

Tag der mündlichen Prüfung:

15. 04. 2024

Eidesstattliche Versicherung

Ich, Marcel Unger, versichere an Eides Statt, dass die Dissertation von mir selbständig und ohne unzulässige fremde Hilfe unter Beachtung der „Grundsätze zur Sicherung guter wissenschaftlicher Praxis an der Heinrich-Heine-Universität Düsseldorf“ erstellt worden ist.

Ort, Datum	Unterschrift

Abstract

The mode-coupling theory (MCT) equations have been adapted to describe chiral active Brownian particles (CABP), which possess a swim velocity and exhibit an additional directed rotation with fixed frequency. This frequency accounts for structural deviations from a perfect sphere or impaired locomotion characteristics of the particle. A detailed recapitulation is presented on how to derive the partial integro-differential equation for the intermediate (ISF) and self-intermediate (SISF) scattering function.

Through systematic tracking of particle positions and orientations, an orientation-position-dependent density function is formulated. This function undergoes Fourier transform, culminating in a density mode encompassing phase aspects encapsulating this information. Consequently, the ISF materializes as the ensemble average of a pair of such density modes, evaluated once initially and once subsequently. The expression of the density function at a later time is obtained by applying the matrix exponential of the adjoint Smoluchowski operator, comprising the adjoint of the differential operator embedded in the Fokker-Planck formulation of the problem, to the function at its initial state. This strategy transcends the confines of linear response.

Theoretical outcomes from MCT are contrasted with results from event-driven Brownian dynamics (ED-BD) simulations. To achieve this, a density mapping is performed, which is required due to the fact that MCT exaggerates the impact of dynamical arrest, resulting in a glass transition that occurs at densities that are too low. The numerical framework has been implemented using the Julia programming language, and it employs an analytical expression for the inverse frequency matrix, which is a significant enhancement over prior implementations. The SISF, as well as the relaxation time, are compared and demonstrate a generally satisfactory agreement between the two methods.

The techniques and findings elucidated in this study are additionally used to probe ABP and their variations. A further aspect to explore lies in the application of the analytical derivations across a broader spectrum of system parameters. From an experimental standpoint, the oscillatory patterns inherent in the correlation functions, as well as the disparate relaxation behaviors of the ISF and the SISF in the regime of small wave numbers, corresponding to long-wave-length fluctuations, appear as relevant theoretical predictors.

Zusammenfassung

Die Moden-Kopplungstheorie (MCT) Gleichungen wurden angepasst, um chirale aktive Brown'sche Teilchen (CABP) zu beschreiben, die eine Schwimmgeschwindigkeit aufweisen und die rotierende Eigenschaft einer Rotationsfrequenz aufzeigen. Diese Frequenz berücksichtigt strukturelle Abweichungen von einer perfekten Kugel oder beeinträchtigte Fortbewegungseigenschaften des Teilchens. Es wird eine detaillierte Zusammenfassung präsentiert, wie man die partielle Integro-Differentialgleichung für die intermediäre Streuungsfunktion (ISF) und die selbstintermediäre Streuungsfunktion (SISF) herleitet.

Durch systematische Verfolgung der Teilchenpositionen und Teilchenorientierungen wird eine orientierungspositionsabhängige Dichtefunktion formuliert. Diese Funktion durchläuft eine Fourier-Transformation und mündet in eine Dichtemode, die Phasenfaktoren einschließt, die diese Information beinhalten. Folglich kristallisiert sich die ISF als das Ensemblemittel eines Paares solcher Dichtemodi heraus, ausgewertet einmalig zu Beginn und einmalig zu einem späteren Zeitpunkt. Die Dichtefunktion zu dem späteren Zeitpunkt ist durch Anwendung der Matrixexponentialfunktion des adjungierten Smoluchowski-Operators auf die Funktion in ihrem Anfangszustand bestimmt, der dem adjungierten des in der Fokker-Planck-Formulierung des Problems entsprechenden Differentialoperators umfasst. Diese Strategie übertrifft die Grenzen der linearen Antwort.

Theoretische Ergebnisse aus der MCT werden mit Ergebnissen aus der ereignisgetriebenen Brown'schen Dynamik (ED-BD) Simulationen kontrastiert. Um dies zu erreichen, wird ein Dichtemapping durchgeführt, das aufgrund der Tatsache erforderlich ist, dass MCT den Einfluss der Käfigbildung übertrieben darstellt, was zu einem Glasübergang führt, der bei zu niedrigen Dichten auftritt. Das numerische Framework wurde unter Verwendung der Programmiersprache Julia implementiert und verwendet einen analytischen Ausdruck für die inverse Frequenzmatrix, was eine bedeutende Abweichung von früheren Implementierungen darstellt. Die SISF sowie die Relaxationszeit werden verglichen und zeigen im Allgemeinen eine zufriedenstellende Übereinstimmung zwischen den beiden Methoden.

Die in dieser Dissertation erläuterten Techniken und Ergebnisse werden zusätzlich genutzt, um aktive Brown'sche Teilchen (ABP) und deren Variationen zu untersuchen. Eine interessante Möglichkeit besteht darin, diese analytischen Erkenntnisse auf ein breiteres Spektrum von Systemparametern anzuwenden. Aus experimenteller Sicht sind die oszillatorischen Muster in Korrelationsfunktionen sowie die unterschiedlichen Relaxationsverhalten der ISF und der SISF im Bereich der winzigen Wellenzahlen und folglich erhöhten räumlichen Ausdehnungen von beträchtlichem Interesse.

Contents

1. Introduction

Active Brownian motion is an extension of Brownian motion [1] where each particle is endowed with a self propulsion in the form of a constant swim velocity that requires energy from the environment and leads to a non-equilibrium dynamics, as opposed to an equilibrium one [2]. Chiral active Brownian particles (CABP), also known as active circle swimmers, are a further generalization that incorporate circular motion resulting from a propelling force that is not aligned with the particle's orientation [3, 4]. An example of a CABP is a biological micro swimmer with an inherent asymmetry [5, 6].

Models of active particles play a crucial role in comprehending the behavior of microorganisms like bacteria and Chlamydomonas [7]. They also aid in developing concepts for drug delivery and biomarkers [8–10]. Upon cooling of such a system effects such as a drastic slowing down of transport coefficients like the viscosity, a two-step relaxation process of the intermediate scattering function, or the stretching of response functions over large time intervals can be observed both experimentally [11–21] and in molecular-dynamics simulations [22–33]. Biological microswimmers use flagellae for locomotion, which possess intricate geometry, making it arduous to study their collective behavior through mathematical models [7]. Consequently, colloidal systems of artificial active swimmers are utilized to simulate their behaviors. Colloidal particles, propelled in circular trajectories owing to various forms of asymmetry or deformations, have undergone theoretical scrutiny in two distinct scenarios: the single particle case [3, 34–36] and the collective behavior exhibited within a multi-particle system [37–41]. In the latter scenario, the intricate nature of the equations necessitates numerical investigations, given the rarity of analytical solutions. Notably, experiments exploring the dynamics of these circular swimmers have also been undertaken [42–44]. In this study, two dimensional chiral active Brownian particles are used to model a colloidal system of artificial active swimmers. The system is described by the following parameters: the translational diffusion coefficient D_t, the rotational diffusion coefficient D_r, the self-propulsion velocity v, the packing fraction η, the diameter σ of each particle, and the rotational frequency ν. Although these systems have already been extensively studied at low packing fractions, the dynamics at high densities is still not widely studied [6, 45].

The mathematical depiction of the model is accomplished through a partial integro-differential equation that governs the intermediate scattering function (ISF), a quantity evaluated through mode-coupling theory (MCT) in conjunction with the integration through transients (ITT) formalism. This is the central departure from prior investigations. To derive this MCT-equation, the initial step involves the formulation of an overdamped Langevin equation for the system. This assumption implies a highly viscous system and particle masses of small proportions, with "small" denoting the typical scale of microswimmers, spanning several micrometers. This classification effectively excludes objects of greater dimensions, such as larger dust grains. Recent investigations have shifted towards the adoption of a Langevin dynamics framework as opposed to a Brownian one [46, 47]. In this context, the particle's motion cannot be viewed as overdamped due to the presence of more pronounced inertial effects. Consequently, the complete Langevin equation must be

employed, as opposed to the overdamped variant. Given that the primary focus of this study revolves around elucidating the behavior of CABP within a viscous solution, and not in a gaseous medium, the findings of these aforementioned investigations remain outside the scope of the current study. The overdamped Langevin equation, functioning as a type of stochastic differential equation [48], can be transformed into a corresponding Fokker-Planck equation [49, 50]. This latter equation characterizes the temporal evolution of the probability density. The solution to this equation is governed by an exponential operator, wherein the exponent encompasses the operator housing the derivative terms. Termed the Smoluchowski operator within this context, this operator has central significance. By systematically recording the positions and orientations of particles, this density function reliant on orientation and position can be established. Through Fourier transform, this function transmutes into a density mode, replete with phase components encapsulating said information. Thus, the ISF emerges as the ensemble average of a pair of such density modes, assessed both at the initial time and a subsequent moment [51]. The density function at a subsequent time is obtained by applying the matrix exponential of the adjoint Smoluchowski operator to said function at the initial time. This approach transcends the boundaries of linear response. Through the act of projection onto density modes via a suitable projector, often referred to as the Mori-Zwanzig formalism [52], a preliminary differential equation governing the ISF is deduced. A further projection engenders superior convergence behavior [53], while a third leads to the MCT-approximation [54]. This last projection is an approximation, achieved through projection onto density pairs and the subsequent approximation of a four-point function as a summation of two multiplicative pairs of two-point functions, is tailored to account for the emergence of transient confinement structures, colloquially termed "cages," that enclose and confine adjacent particles.

The fundamental aim of this study is the exploration of dense systems of CABP. A comprehensive juxtaposition of findings derived from mode-coupling theory and event-driven Brownian dynamics simulations is made. This progression necessitates the adoption of a novel equation implementation while scrutinizing extant challenges, particularly numerical tasks. The core of this inquiry lies in the focus on the intermediate scattering function (ISF) and self-intermediate scattering function (SISF). Moreover, a fresh analysis to discern their disparities, particularly in relation to one another and with respect to their relaxation times, is imperative. Furthermore, an examination is warranted to discern how analytical explorations, such as the reinterpretation of the memory kernel and the inversion of the frequency matrix, might help to improve numerical stability.

Prior investigations, particularly the work of Liluashvili [55] and Reichert [23–25], have primarily revolved around the realm of mode-coupling theory (MCT) and event-driven Brownian dynamics simulations (ED-BD) applied to active Brownian particles. Liluashvili's work delved into the ramifications of swim velocity and rotational diffusion constants, as well as motility-induced phase separation (MIPS) within such systems. Reichert, on the other hand, embarked on a broader endeavor by extending the theoretical framework to encompass particle mixtures, thereby facilitating the scrutiny of the self-intermediate scattering function. This endeavor bore fruit, given that ED-BD simulations, as of now, can only proficiently describe the SISF and not the ISF. Within Reichert's corpus of work, scrutiny was directed towards the conduct of a passive Brownian particle (PBP) within a host environment of ABP, and conversely, as well as the behavior of ABP within a system of identical particles. Both lines of inquiry unveiled the emergence of numerical instabilities when dealing with high swim speeds and elevated rotational diffusion constants. It emerged that MCT tends to overestimate the influence of dynamical arrest, leading to an overestimation of the critical packing fraction. Additionally, MCT seemingly underestimated the effect

of swim speed, a bias accentuated at packing fractions proximate to the glass transition. Reichert highlighted and delved into the complications that arise during the inversion of the translational frequency matrix, which stands as the matrix counterpart of the translational Smoluchowski operator. Notably, the numerical investigation mandates the introduction of an angular index cutoff, derived from the Fourier transform of the angle between an ABP and the x-axis, a value intrinsically denoted by integer values devoid of constraints. It's pertinent to note that the act of matrix inversion in conjunction with an index cutoff is a non-commutative operation, introducing an additional layer of complexity. Concerning the reciprocal, wave number q-dependent matrix, a transition becomes evident, from a $1/q^2$ trend, reminiscent of that exhibited by a passive tracer, to a $1/q$ pattern occurring at approximately $q \approx v^s/D_t^s$, where v^s denotes the swim speed and D_t^s the translational diffusion constant of the tagged particle, as delineated by the SISF. This distinctive transition finds its explanation within the movement dynamics of an unencumbered ABP, wherein the ballistic regime solely manifests on specific length scales. In this work an analytic expression for the inverse translational frequency matrix is found, making any numerical inversion redundant and excluding this entity from the list of suspects, yielding numerical instabilities.

The dissertation follows the subsequent structure:

Chapter (2) elucidates the adaptations made on the partial integro-differential equation for the intermediate scattering function, tailored to encompass the nuances between two-dimensional active Brownian particles and two-dimensional chiral active Brownian particles. These adaptations encompass revisions to the self-intermediate scattering function and the frequency matrix. In doing so, this chapter revisits the bedrock of the mathematical depiction and the tools used to describe this system. The exposition commences by unraveling the modifications made to the overdamped Langevin equation, subsequently explicating its counterpart, the Fokker-Planck equation. The discourse proceeds to unravel the underpinning principles of the ITT-formalism, followed by the derivation of the MCT-equation, both for the ISF and the SISF. Herein, the significance of the static correlation function is underscored.

In Chapter (3), an investigation is made upon to perform the analytic inversion of the translational component of the frequency matrix, a result subsequently used within the numerical framework. Additionally, a methodology is outlined to facilitate the transformation of all entities in the x-direction, thereby simplifying the wave vector dependence to a real-valued wave number. This chapter culminates in the analytic derivation of the memory kernel, encompassing both real and imaginary components, that is a feature that augments numerical stability.

Chapter (4) delves into a comprehensive delineation of the coding implementation underpinning this thesis. Primarily, the numerical discretization scheme is expounded upon, emphasizing a format tailored to the programming language Julia. The programming structure and intricacies specific to Julia are expounded upon. Afterwards, a succinct overview of the enhanced integration scheme is presented, coupled with a discussion of unresolved issues. Finally, an exposition is presented concerning a specific non-uniform integration technique. This approach proves instrumental in enhancing computational efficiency, albeit exclusively within the context of PBP. The elucidation underscores that when considering extensions such as ABP and CABP, the intricate vertex architectures inherent in these models render the utilization of this technique unreliable.

Chapter (5) offers an expansive survey of MCT-derived findings for CABP. The chapter

embarks by contrasting the outcomes with the passive Brownian particle limit before delving into the realm of CABP. The scrutiny extends to investigating the impact of rotational frequency across a broad parameter spectrum. Furthermore, the effects of rotational diffusion and swim speed for CABP are juxtaposed against the corresponding impacts on ABP. Subsequently, a comparison is drawn between data from ED-BD-simulations and MCT-results. The chapter culminates in an exploration of relaxation times vis-à-vis packing fraction and wave number.

Chapter (6) concludes this thesis by succinctly summarizing the accomplishments of this research and providing a roadmap for unresolved questions.

2. Theory and Extensions of ABP

The mode coupling theory [54] for passive Brownian particles, was expanded by Liluashvili [55] to encompass active Brownian particles. Reichert [23–25] further generalized this theory to mixtures of such particles, which may exhibit differences in their parameters, such as their diffusion constants. In this work, Reichert's theory is reexamined extending it to CABP. This revised framework highlights the previously underutilized symmetry properties of the dynamical correlation function, the friction kernel, and the frequency matrix. The focus of this investigation is restricted to two-dimensional particles.

2.1 The Model of Chiral Active Brownian Particles

A *chiral active Brownian particle* (CABP) is an extension of an *active Brownian particle* (ABP), which itself is a generalization of a *passive Brownian particle* (PBP). The defining characteristic of this extension is a rotation of each particle around an axis perpendicular to its center of mass, accompanied by the feature of an ABP of a self-propelled movement in a dissipative environment. When the rotational frequency approaches zero, an ABP and if that also looses its self-propelled movement, a PBP, is obtained. The parameters that describe the model of a CABP include the particle's diameter σ, packing fraction η, a translational diffusion constant D_t, a rotational diffusion constant D_r, swim speed v, and rotational frequency ν. Figure (2.1a) and Figure (2.1b) provide a schematic representation of these particles. The swim velocity, which accounts for the self-propelled motion, acts on the center of mass of each particle and is directed along a fixed intrinsic body axis. It can be expressed as $\boldsymbol{v} = (v\cos\varphi, v\sin\varphi)^T$, where v is the previously mentioned speed and φ is the angle between the body axis and the x-coordinate axis of the system.

The following discussion employs units that are expressed in terms of the translational diffusion constant D_t and the particle's diameter σ. Therefore, all dependent variables can be denoted as dimensionless variables. Thus, the expression of the relevant quantities is

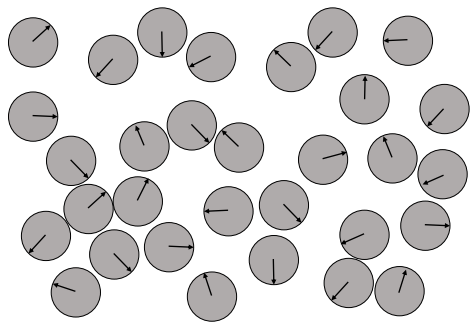

(a) Schematic illustration of 2D active Brownian particles (ABP)

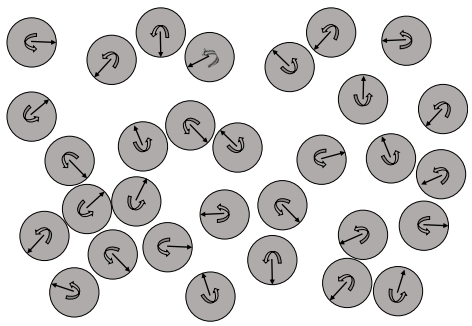

(b) Schematic illustration of 2D chiral active Brownian particles (CABP)

given by

$$[D_r] = \left[\frac{D_t}{\sigma^2}\right], \quad [v] = \left[\frac{D_t}{\sigma}\right], \quad [\nu] = \left[\frac{D_t}{\sigma^2}\right], \quad [\tau] = \left[\frac{\sigma^2}{D_t}\right]. \tag{2.1}$$

In this regard, the parameter τ is associated with a timescale, such as a relaxation time. The model of ABP and CABP aims to provide a comprehensive understanding of both natural and artificial microswimmers that are tiny organisms or particles that are capable of self-propulsion, typically on the micrometer scale, as highlighted in the introduction. Examples of natural microswimmers include bacteria, algae, and sperm cells [7]. These organisms can move through a fluid by using different mechanisms, such as flagella or cilia. On the other hand, artificial microswimmers are man-made particles that can move autonomously in a fluid, driven by external stimuli such as magnetic or electric fields. These particles can have various shapes, such as spheres, rods, or helices, and can be made of different materials, such as polymers, metals, or magnetic materials. These swimmers have characteristic speeds ranging from one to ten times their body size per second, which can be approximated by a diameter of one micrometer [7]. Therefore, the ratio $v\sigma/D_t \sim 1 - 10$ defines the domain that this theory endeavors to explain. Moreover, the present study focuses on high-density systems, characterized by high packing fractions close to the glass transition point.

To determine an appropriate theoretical framework for this model, several length scales must be considered. The goal is to identify a classical theory that adequately describes the model, assuming that quantum mechanical effects can be disregarded. This condition is satisfied when the thermal de Broglie wavelength is much smaller than the mean nearest-neighbor separation. This is typically the case for microscopic particles and especially true for the experimental realizations of this work. The time-dependent processes to be studied here are easily on a time scale larger than $\beta\hbar$, which supports the use of a classical description of the model. Specifically, an overdamped Langevin equation has been selected to characterize the system, neglecting the inertia terms and hydrodynamic interactions. This approximation can be justified by evaluating the contribution of the inertia terms to the equation for typical microswimmers, which is encapsulated in the relaxation time $\tau = m/\gamma$, where γ is the friction constant. For instance, silica particles exhibit relaxation times of 0.1 microseconds, similar to those observed for microswimmers. These time scales are several orders of magnitude shorter than those typically encountered in experiments, which are on the order of a few milliseconds [56]. Furthermore, this model distinguishes itself from dilute gases due to its short-range behavior, and from crystalline solids due to its lack of long-range order. At short ranges, the collisional processes and short-range positional correlations are more significant than in a dilute gas.

To formulate an equation for CABP, each particle should be identified by an index $i \in 1, \ldots, N$, where N denotes the total number of particles. The particles may not vary in their model parameters, represented by $\{\eta, D_t, D_r, v, \nu\}$, where $\eta = \varrho\pi\sigma^2/4$ is the packing fraction, and $\varrho = N/V$ is the particle number density, the ratio of the number of particles N to the volume V. Therefore, this study neglects mixtures of ABP and CABP and focuses on the dynamics of particles of the same type. The equations for CABP for multi-component systems are a trivial extension to the equations for multi-component systems for ABP and therefore are omitted for clarity. With this information, the overdamped Langevin equation of that system is a generalization of that of ABP [55] and can be written as

$$\begin{aligned} \mathrm{d}\boldsymbol{r}_i(t) &= \sqrt{2D_t}\mathrm{d}\boldsymbol{W}_{\boldsymbol{r}_i}(t) + v\boldsymbol{o}_i(t)\mathrm{d}t + D_t\beta\boldsymbol{F}_i(t)\mathrm{d}t, \\ \mathrm{d}\varphi_i(t) &= \sqrt{2D_r}\mathrm{d}W_{\varphi_i}(t) + \nu\mathrm{d}t. \end{aligned} \tag{2.2}$$

Here, $\mathrm{d}\boldsymbol{W}_{\boldsymbol{r}_i}(t) = \boldsymbol{\xi}_{\boldsymbol{r}_i}(t)\mathrm{d}t$ and $\mathrm{d}W_{\varphi_i}(t) = \xi_{\varphi_i}(t)\mathrm{d}t$ denote the Wiener differentials that can

be associated with the fluctuation force $\boldsymbol{\xi}_{\boldsymbol{r}_i}(t)$ or $\xi_{\varphi_i}(t)$. The concept of incorporating such a force term into the equation originated with Einstein [57] and reflects random impacts from neighboring particles. As a result, the force is unpredictable. This property is mathematically known as the white noise property. It states that the expected value of a realization of a Wiener process, calculated as a time average, must equal zero, has a zero variance and a constant power spectral density [58]. The time averages can be expressed as follows

$$\begin{aligned} \langle \xi_i(t) \rangle &= 0, \quad i \in \{x_i, y_i\}, \\ \langle \xi_i(t)\xi_j(t') \rangle &= \delta_{ij}\delta(t-t'), \quad i,j \in \{x_i, y_i\}. \end{aligned} \tag{2.3}$$

The terms in the Langevin equation that pertain to diffusion constants are indicative of diffusive dynamics. The prefactor can be rephrased in terms of the fluctuation strength and the friction coefficient, as prescribed by the fluctuation dissipation theorem [59]. The term featuring the swim speed v pertains to the self-propelled motion of the particle. The vector $\boldsymbol{o}_i(t) = (\cos\varphi_i, \sin\varphi_i)^T$ reflects the orientation of the particle. The force term pertains to interactions. Upon examination of the equation for the angle, one can discern a diffusive term and a term that confers chirality to the system by adding a rotational frequency that contributes to the particle's driven rotational motion, may it be caused by a defect in the particle's shape or may it be artificially driven. The interaction force is related to an interaction potential by $\boldsymbol{F}_i = -\boldsymbol{\nabla}_i \sum_{j\neq i} U_{ij}$. The potential is defined to reflect hard-core interactions, though this is a simplification of the observations made in experiments [9], and can be expressed as

$$U_{ij}(|\boldsymbol{r}_i - \boldsymbol{r}_j|) = \begin{cases} \infty, & \text{if } |\boldsymbol{r}_i - \boldsymbol{r}_j| < \sigma, \\ 0, & \text{else.} \end{cases} \tag{2.4}$$

The Langevin equation is a general stochastic differential equation [48] of the form

$$\mathrm{d}\boldsymbol{X} = \boldsymbol{A}(\boldsymbol{X}, t)\mathrm{d}t + B(\boldsymbol{X}, t)\mathrm{d}\boldsymbol{W}(t), \tag{2.5}$$

well known for its ability to be transformed into a Fokker-Planck equation [49, 50], that reads

$$\partial_t \mathcal{P}(\boldsymbol{X}, t) = -\sum_i \partial_{X_i}\left[A_i \mathcal{P}(\boldsymbol{X}, t)\right] + \frac{1}{2}\sum_{ijk} \partial_{X_i} B_{ik} \partial_{X_j} B_{jk} \mathcal{P}(\boldsymbol{X}, t), \tag{2.6}$$

which describes the time evolution of the probability $\mathcal{P}(\boldsymbol{X}, t)$ of finding the system in a certain configuration at a certain time. Here, the summation corresponds to that of a Stratonovich integration instead of an Ito integration, thereby preserving the standard chain rule for the probability density and explaining the ordering of partial derivative terms in the last term of the Fokker-Planck equation. The use of the Fokker-Planck equation is deemed advantageous to the Langevin formulation due to the ease of defining equilibrium and nonequilibrium averages. These averages, allow to study observables like the dynamical correlation function or transport coefficients like the effective swim velocity, from a microscopic point of view. As an illustration, the case of a single active circle swimmer is investigated, yielding an equation

$$\begin{pmatrix} \mathrm{d}x \\ \mathrm{d}y \\ \mathrm{d}\varphi \end{pmatrix} = \underbrace{v \begin{pmatrix} \cos\varphi \\ \sin\varphi \\ \nu/v \end{pmatrix}}_{\boldsymbol{A}(\boldsymbol{X},t)} \mathrm{d}t + \underbrace{\begin{pmatrix} \sqrt{2D_t} & 0 & 0 \\ 0 & \sqrt{2D_t} & 0 \\ 0 & 0 & \sqrt{2D_r} \end{pmatrix}}_{B(\boldsymbol{X},t)} \begin{pmatrix} \mathrm{d}W_x \\ \mathrm{d}W_y \\ \mathrm{d}W_\varphi \end{pmatrix}, \tag{2.7}$$

which in that context can also be referred to as the Smoluchowski equation

$$\partial_t \mathcal{P} = -v(\cos\varphi\ \partial_x + \sin\varphi\ \partial_y + \nu/v\partial_\varphi)\mathcal{P} + (D_t\partial_x^2 + D_t\partial_y^2 + D_r\partial_\varphi^2)\mathcal{P}. \tag{2.8}$$

The extension to encompass many chiral active Brownian circle swimmers and mixtures thereof is a straightforward process. The Smoluchowski equation, i.e. the Fokker-Planck equation, can be written as

$$\partial_t \mathcal{P}(\{\boldsymbol{r}_i\},\{\varphi_i\},t) = \Omega \mathcal{P}(\{\boldsymbol{r}_i\},\{\varphi_i\},t), \tag{2.9}$$

using the so-called Smoluchowski operator

$$\Omega = \sum_{i=1}^{N} \left[D_t(\boldsymbol{\nabla}_i - \beta \boldsymbol{F}_i)\cdot\boldsymbol{\nabla}_i + D_r \partial_{\varphi_i}^2 - v_0 \boldsymbol{o}_i \cdot \boldsymbol{\nabla}_i - \nu \partial_{\varphi_i} \right]. \tag{2.10}$$

Here, the inner products are standard $\mathbb{R}^2$ inner products, and thus symmetric and positive definite. By introducing the phase space $\Gamma = (\Gamma_{\boldsymbol{r}}, \Gamma_{\varphi})$, the Smoluchowski equation can be expressed as

$$\partial_t \mathcal{P}(\Gamma, t) = \Omega \mathcal{P}(\Gamma, t). \tag{2.11}$$

To describe the time evolution of an observable, the adjoint Smoluchowski operator is required instead of the usual one. Before showing its expression one should note that the configuration space differential is defined as

$$\mathrm{d}\Gamma = \prod_{i=1}^{N} \mathrm{d}\boldsymbol{r}_i \mathrm{d}\varphi_i \equiv \mathrm{d}\Gamma_{\boldsymbol{r}} \mathrm{d}\Gamma_{\varphi}. \tag{2.12}$$

The equilibrium average can be expressed like $\langle\cdot\rangle \equiv \int \mathrm{d}\Gamma \mathcal{P}_{\mathrm{eq}}(\cdot)$, while the non-equilibrium average is expressed as $\langle\cdot\rangle_{\mathrm{neq}} \equiv \int \mathrm{d}\Gamma \mathcal{P}(\cdot)$. Furthermore, an unweighted average can be defined as $[\cdot] \equiv \int \mathrm{d}\Gamma(\cdot)$, and the corresponding inner product between two scalar observables can be defined as $\langle A|B\rangle \equiv \int \mathrm{d}\Gamma \mathcal{P}_{\mathrm{eq}} A^*(\Gamma) B(\Gamma)$, $\langle A|B\rangle_{\mathrm{neq}} \equiv \int \mathrm{d}\Gamma \mathcal{P} A^*(\Gamma) B(\Gamma)$, and $[A|B] \equiv \int \mathrm{d}\Gamma A^*(\Gamma) B(\Gamma)$. The formal solution of the Smoluchowski equation is given by

$$\mathcal{P}(\Gamma, t) = \mathrm{e}^{\Omega t}\, \mathcal{P}(\Gamma, t=0), \quad \text{with} \quad \mathcal{P}(\Gamma, t=0) = \mathcal{P}_{\mathrm{eq}} = \frac{1}{\mathcal{Z}} \mathrm{e}^{-\beta U(\Gamma_{\boldsymbol{r}})}.$$

This assumes that the probability distribution is the formal solution of the Smoluchowski equation and that the system is initially in a state of equilibrium. The partition function is defined as

$$\mathcal{Z} = \int \mathrm{d}\Gamma\, \mathrm{e}^{-\beta U(\Gamma_{\boldsymbol{r}})} = \int \mathrm{d}\Gamma_{\boldsymbol{r}} \mathrm{d}\Gamma_{\varphi}\, \mathrm{e}^{-\beta U(\Gamma_{\boldsymbol{r}})} = (2\pi)^N \int \mathrm{d}\Gamma_{\boldsymbol{r}}\, \mathrm{e}^{-\beta U(\Gamma_{\boldsymbol{r}})}. \tag{2.13}$$

It is worth noting that the property of the potential being angle independent is often utilized in the calculations. The Smoluchowski operator is adjoint with respect to the unweighted inner product. It turns out to be

$$\Omega^{\dagger} = \sum_{i=1}^{N} \left[D_t(\boldsymbol{\nabla}_i + \beta \boldsymbol{F}_i)\cdot\boldsymbol{\nabla}_i + D_r \partial_{\varphi_i}^2 + v \boldsymbol{o}_i \cdot \boldsymbol{\nabla}_i + \nu \partial_{\varphi_i} \right]. \tag{2.14}$$

For later purposes it is noteworthy that the Smoluchowski operator can be divided into an equilibrium part and a non-equilibrium part, both of which can further be divided into translational and rotational parts

$$\begin{aligned} \Omega(\{D_t, D_r, v, \nu\}) &= \Omega_{\mathrm{eq}}(\{D_t, D_r\}) + \Omega_{\mathrm{neq}}(\{v, \nu\}) \\ &= \Omega_{\mathrm{eq},t}(\{D_t\}) + \Omega_{\mathrm{eq},r}(\{D_r\}) + \Omega_{\mathrm{neq},t}(\{v\}) + \Omega_{\mathrm{neq},r}(\{\nu\}), \end{aligned} \tag{2.15}$$

that read

$$\begin{aligned} \Omega_{\mathrm{eq},t} &= \sum_{i=1}^{N} D_t(\boldsymbol{\nabla}_i - \beta \boldsymbol{F}_i)\cdot\boldsymbol{\nabla}_i, \quad \Omega_{\mathrm{eq},r} = \sum_{i=1}^{N} D_r \partial_{\varphi_i}^2, \\ \Omega_{\mathrm{neq},t} &= -\sum_{i=1}^{N} v \boldsymbol{o}_i \cdot \boldsymbol{\nabla}_i, \quad \Omega_{\mathrm{neq},r} = -\sum_{i=1}^{N} \nu \partial_{\varphi_i}. \end{aligned} \tag{2.16}$$

The non-equilibrium parts consume energy from the environment and lack the feature of detailed balance.

To find the time description for observables, the integration through transients (ITT) formalism will be utilized. The calculation starts by computing the non-equilibrium average of a scalar observable

$$\langle A(\Gamma)\rangle_{\mathrm{neq}} = \int \mathrm{d}\Gamma \mathcal{P}(\Gamma,t)A(\Gamma) = \int \mathrm{d}\Gamma \mathcal{P}_{\mathrm{eq}}A(\Gamma) + \int \mathrm{d}\Gamma \int_0^t \mathrm{d}t' \Big[\mathrm{e}^{\Omega t'}\,\Omega\mathcal{P}_{\mathrm{eq}}(\Gamma)\Big]A(\Gamma), \quad (2.17)$$

where the identity

$$\mathrm{e}^{\Omega t} = 1 + \int_0^t \mathrm{d}t'\,\mathrm{e}^{\Omega t'}\,\Omega$$

is inserted in the equation. The final calculation in the derivation utilizes the commutativity of phase space and time integrals, as well as the definition of the unweighted inner product and the property $\Omega\mathcal{P}_{\mathrm{eq}} = \Omega_{\mathrm{neq}}\mathcal{P}_{\mathrm{eq}}$. The equation

$$\begin{aligned}\int \mathrm{d}\Gamma \int_0^t \mathrm{d}t' \Big[\mathrm{e}^{\Omega t'}\,\Omega\mathcal{P}_{\mathrm{eq}}(\Gamma)\Big]A(\Gamma) &= \int_0^t \mathrm{d}t' \left[\Big(\mathrm{e}^{\Omega t'}\,\Omega\mathcal{P}_{\mathrm{eq}}(\Gamma)\Big)^* \Big| A(\Gamma)\right] \\ = \int_0^t \mathrm{d}t' \left[(\Omega_{\mathrm{neq}}\mathcal{P}_{\mathrm{eq}}(\Gamma))^* \Big| \mathrm{e}^{\Omega^\dagger t'}\,A(\Gamma)\right] &= \int_0^t \mathrm{d}t' \left\langle \frac{\Omega_{\mathrm{neq}}\mathcal{P}_{\mathrm{eq}}}{\mathcal{P}_{\mathrm{eq}}}\,\mathrm{e}^{\Omega^\dagger t'}\,A(\Gamma)\right\rangle.\end{aligned} \quad (2.18)$$

as a result, presents a means of expressing a non-equilibrium average of a scalar observable as a combination of an equilibrium average and a time integral of that average. If one adds the missing first term, the final equation is obtained to be

$$\langle A(\Gamma)\rangle_{\mathrm{neq}} = \langle A(\Gamma)\rangle + \int_0^t \mathrm{d}t' \left\langle \frac{\Omega_{\mathrm{neq}}\mathcal{P}_{\mathrm{eq}}}{\mathcal{P}_{\mathrm{eq}}}\,\mathrm{e}^{\Omega^\dagger t'}\,A(\Gamma)\right\rangle. \quad (2.19)$$

It is further established that the time evolution of an observable can be expressed as $A(\Gamma,t) = \mathrm{e}^{\Omega^\dagger t}\,A(\Gamma,t=0)$. In the study of transient correlation functions, it is imperative to consider the regime beyond linear response. This can be accomplished through the definition

$$\langle B(0)A(t)\rangle = \int \mathrm{d}\Gamma A(\Gamma,t)\mathcal{P}(\Gamma,t)B(\Gamma) = \langle B\,\mathrm{e}^{\Omega^\dagger t}\,A\rangle. \quad (2.20)$$

Here, an equilibrium average is utilized instead of a transient ensemble average, because the later one describes the quenched dynamics from an equilibrated state when the effect of activity comes into account. The time evolution of the probability distribution is governed by the initial equilibrium distribution and the time evolution operator. Therefore the average is time independent, thus explaining why a transient ensemble average in this case translates into an equilibrium ensemble average.

2.2 The MCT-Equation

The *mode-coupling theory* (MCT) is an approximation that results in a differential equation for the dynamical correlation function, thus governing its time evolution. In the context of a CABP, the calculation of Liluashvili [55] is revisited.

The Fourier convention

$$\begin{aligned} f(\boldsymbol{r},t) &\xrightarrow{\mathcal{F}} \tilde{f}(\boldsymbol{q},\omega) = \int \mathrm{d}\boldsymbol{r} \int \mathrm{d}t\,\mathrm{e}^{\mathrm{i}(\boldsymbol{q}\cdot\boldsymbol{r}-\omega t)}\,f(\boldsymbol{r},t), \\ \tilde{f}(\boldsymbol{q},\omega) &\xrightarrow{\mathcal{F}^{-1}} f(\boldsymbol{r},t) = \int \frac{\mathrm{d}\boldsymbol{q}}{(2\pi)^2} \int \frac{\mathrm{d}\omega}{2\pi}\,\mathrm{e}^{-\mathrm{i}(\boldsymbol{q}\cdot\boldsymbol{r}-\omega t)}\,\tilde{f}(\boldsymbol{q},\omega), \end{aligned} \quad (2.21)$$

is used to transform a scalar function $f : \mathbb{R}^2 \times \mathbb{R} \to \mathbb{C}$. One of the most fundamental properties of the system, besides its model parameters, is its density. Not the number density, proportional to the packing fraction, but rather the number of particles of a certain type at a particular position $\boldsymbol{r}$ with a specified orientation φ. The expression

$$\rho(\boldsymbol{r}, \varphi, t) = \frac{1}{\sqrt{N}} \sum_{i=1}^{N} \delta(\boldsymbol{r} - \boldsymbol{r}_i(t)) \; \delta(\varphi - \varphi_i(t)) \tag{2.22}$$

describes this behavior through a formula that sums these quantities. The density can be Fourier transformed into the form

$$\rho_l(\boldsymbol{q}, t) = \int \mathrm{d}\boldsymbol{r} \int \mathrm{d}\varphi \; \mathrm{e}^{\mathrm{i}(\boldsymbol{q}\cdot\boldsymbol{r} + l\varphi)} \, \rho(\boldsymbol{r}, \varphi, t) = \frac{1}{\sqrt{N}} \sum_{i=1}^{N} \mathrm{e}^{\mathrm{i}\,\boldsymbol{q}\cdot\boldsymbol{r}_i(t)} \, \mathrm{e}^{\mathrm{i}\,l\varphi_i(t)} \, . \tag{2.23}$$

Here, the angular index is denoted by $l \in \mathbb{Z}$. To facilitate implementation, a cutoff Λ_L must be established such that $l \in [-\Lambda_L, \Lambda_L]$. This should be taken into consideration while proceeding, and any effects of the cutoff will be noted.

2.2.1 The Static Structure Factor

Before delving into the definition of the intermediate scattering function of the system, it is appropriate to revisit the static density correlators [51]. The limit of a passive Brownian hard disk is considered in this context, and the static correlation is referred to as the *static structure factor* $S(q)$. Figure (2.2) displays the static structure factor obtained through a DFT method [60]. This method shows divergent behavior for packing fractions $\eta > 0.74$, as illustrated in Figure (2.3). The static structure factor represents the density response of a system, initially in equilibrium, to a weak external perturbation with a wavelength of $2\pi/q$. The main peak position of $S(q)$ approximately corresponds to a wavenumber of one inverse particle diameter, $q = 2\pi/\sigma$. The oscillatory pattern indicates that certain distances exhibit higher correlation than others, implying the presence of local order. This is typified by shells of neighboring particles and next-nearest neighboring particles. A liquid, as a disordered system, only exhibits local order, and the function approaches

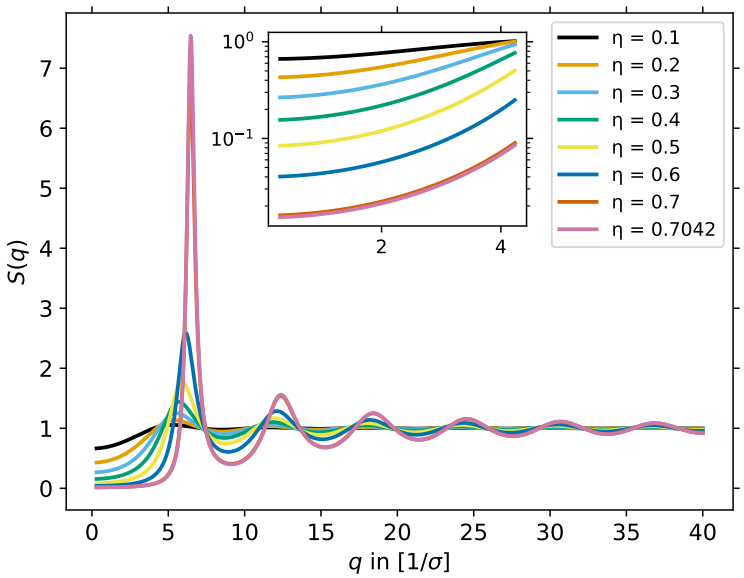

Figure 2.2: The figure highlights the static structure factor, obtained by a DFT-approximation, for a wave number grid of $M = 1000$ values. The set of system parameters comprises $\{D_t = 1.0, \sigma = 1.0\}$.

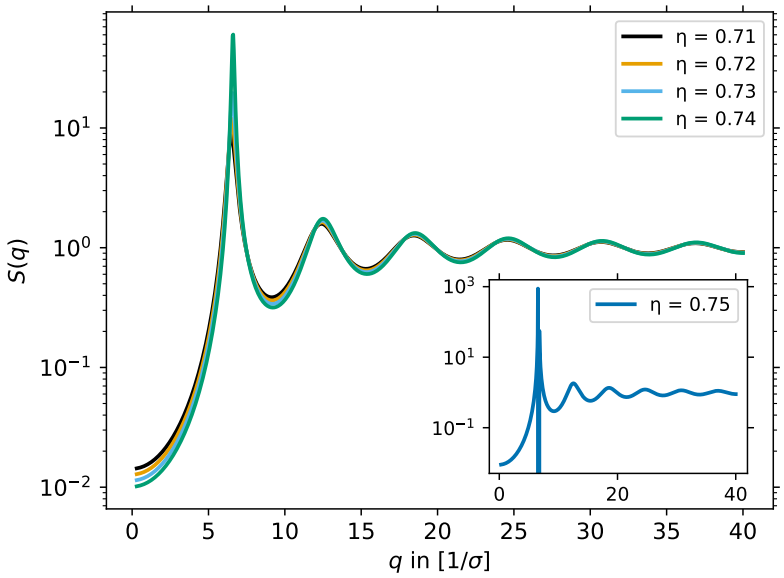

Figure 2.3: The figure highlights the divergent regime of the static structure factor, obtained by a DFT-approximation, for a wave number grid of $M = 1000$ values. The set of system parameters comprises $\{D_t = 1.0, \sigma = 1.0\}$.

a constant value of one for small distances, i.e. $\lim_{q\to\infty} S(q) = 1$. As q approaches zero, the feature of $S(q)$ as a measure of the response in the macroscopic number density to a change in the applied pressure becomes apparent $\lim_{q\to 0} S(q) = \varrho\kappa_T k_B T$, where T is the temperature, ρ the number density, and κ_T the isothermal compressibility [56].

The static structure factor is related to the *direct correlation function*, $c(q)$, through the algebraic relationship

$$S(q) = \frac{1}{1 - \varrho c(q)}. \tag{2.24}$$

The direct correlation function can then be obtained through the *Ornstein-Zernike equation*

$$h(r) = c(r) + \rho \int \mathrm{d}\boldsymbol{r}' c(|\boldsymbol{r} - \boldsymbol{r}'|)h(|\boldsymbol{r}'|), \tag{2.25}$$

which links it to the *total correlation function*, $h(r) = g(r) - 1$. This total correlation function is expressed by the *radial distribution function*, $g(r)$, written in a form that exclusively depends on the distance r and that is therefore only valid for isotropic and uniform liquids. An analytic expression for $c(q)$ can be obtained through a DFT calculation [60] and is expressed using Bessel functions of the first kind of order zero and one, $J_0(x)$ and $J_1(x)$, respectively

$$\begin{aligned} c(q) = \frac{\pi}{6(1-\phi)^3 q^2}\Bigg\{ &-\frac{5}{4}(1-\phi)^2 q^2\sigma^2 J_0^2(q\sigma/2) + \\ &\left[4((\phi-20)\phi)+7) + \frac{5}{4}(1-\phi)^2 q^2\sigma^2\right] J_1^2(q\sigma/2) + \\ &2(\phi-13)(1-\phi)q\sigma J_1(q\sigma/2)J_0(q\sigma/2)\Bigg\}. \end{aligned} \tag{2.26}$$

The static structure factor, as shown in Figure (2.2), is derived from the DFT expression for the direct correlation function. The Ornstein-Zernike equation provides insight into

the physical significance of $c(q)$ and $h(q)$. While $c(q)$ only accounts for direct correlations between particles, $h(q)$ takes into account both direct and indirect correlations that are propagated through numerous intermediate particles, thus having a larger range than the direct correlation function.

To grasp the derivation of these equations [56], a system consisting of N particles in a phase space of $6N$ dimensions is considered. A Hamiltonian can be constructed, comprising a kinetic term, a potential term represented by V_N, and an external field term that modifies the potential, which is set to zero for the purpose of this explanation. The partition function

$$\mathcal{Z}_N = \int \prod_{i=1}^{N} \mathrm{d}\boldsymbol{r}_i \, \mathrm{e}^{-\beta V_N} \tag{2.27}$$

is then written to define the n-particle density

$$\rho_N^{(n)}(\{\boldsymbol{r}\}) = \frac{N!}{(N-n)!} \frac{1}{\mathcal{Z}_N} \int \prod_{i=n+1}^{N} \mathrm{d}\boldsymbol{r}_i \, \mathrm{e}^{-\beta V_N}, \tag{2.28}$$

with $\{\boldsymbol{r}\} = \{\boldsymbol{r}_1, \ldots, \boldsymbol{r}_n\}$. The integration of this density yields the probability of finding n particles within the defined integration domain. Precisely, the following identity holds

$$\int \prod_{i=1}^{n} \mathrm{d}\boldsymbol{r}_i \rho_N^{(n)}(\{\boldsymbol{r}\}) = \frac{N!}{(N-n)!}, \quad \int \mathrm{d}\boldsymbol{r} \rho_N^{(1)}(\boldsymbol{r}) = N. \tag{2.29}$$

This highlights that the single-particle density is equal to the number density in a uniform fluid, i.e. $\rho_N^{(1)}(\boldsymbol{r}) = N/V = \varrho$. For an ideal gas, the relation $\mathcal{Z}_N = V^N$ holds, and the two-particle density can be expressed as $\rho_N^{(2)}(\boldsymbol{r}) = \varrho^2(1 - 1/N)$. With these definitions, it becomes possible to define the n-particle distribution function

$$g_N^{(n)}(\{\boldsymbol{r}\}) = \frac{\rho_N^{(n)}(\{\boldsymbol{r}\})}{\prod_{i=1}^{n} \rho_N^{(1)}(\boldsymbol{r}_i)}, \tag{2.30}$$

which for a uniform system, reads $\varrho^n g_N^{(n)}(\{\boldsymbol{r}\}) = \rho_N^{(n)}(\{\boldsymbol{r}\})$. If the system is isotropic as well, the pair distribution function, denoted by $g_N^{(2)}(\boldsymbol{r}_1, \boldsymbol{r}_2)$, only depends on the distance between particles, i.e. $r = |\boldsymbol{r}_2 - \boldsymbol{r}_1|$, and is referred to as the radial distribution function, denoted by $g(r)$, previously mentioned. For the limit in which the distance r exceeds the length scale specified by the interparticle potential, the system is in the ideal gas regime. As shown by the above formula, the radial distribution function approaches a value of one in the ideal gas limit, as $\lim_{r\to\infty} g(r) = 1$. On the other hand, for small distances, where $\lim_{r\to 0} g(r) = 0$, a limit of zero is reached, reflecting the strong repulsive forces present in those regions. The integral of $4\pi r^2 \varrho g(r)$ gives the number of particles contained within a shell of radius equal to the integration domain. The structure of $g(r)$ closely resembles that of the static structure factor, with peaks appearing at positions where there is a higher concentration of particles. The first maximum corresponds to the shell of nearest neighbors, and an estimate of the number of particles in that shell can be obtained by integrating up to the first minimum.

An alternative approach to obtain these equation is given by expressing the n-particle density as an average of microscopic particle densities. The single-particle and two-particle densities for example can be expressed as

$$\rho_N^{(1)}(\boldsymbol{r}) = \left\langle \sum_{i=1}^{N} \delta(\boldsymbol{r} - \boldsymbol{r}_i) \right\rangle, \quad \rho_N^{(2)}(\boldsymbol{r}, \boldsymbol{r}') = \left\langle \sum_{i,j=1}^{N} \delta(\boldsymbol{r} - \boldsymbol{r}_i)\delta(\boldsymbol{r}' - \boldsymbol{r}_j) \right\rangle. \tag{2.31}$$

To define the *pair correlation function* $h^{(2)}(\boldsymbol{r}_1, \boldsymbol{r}_2) = g^{(2)}(\boldsymbol{r}_1, \boldsymbol{r}_2) - 1$, it is necessary to consider the grand canonical ensemble rather than the canonical ensemble, in which the radial distribution function is defined. If $p(N)$ is the probability that the system of the ensemble contains exactly N particles at equilibrium, the n-particle density in the grand canonical ensemble can be expressed as the sum of the form

$$\rho^{(n)}(\{\boldsymbol{r}\}) = \sum_{N \geq n}^{\infty} p(N) \rho_N^{(n)}(\{\boldsymbol{r}\}), \tag{2.32}$$

and the following identities are derived

$$\int \prod_{i=1}^{n} \mathrm{d}\boldsymbol{r}_i \rho^{(n)}(\{\boldsymbol{r}\}) = \left\langle \frac{N!}{(N-n)!} \right\rangle, \quad \int \mathrm{d}\boldsymbol{r} \rho^{(1)}(\boldsymbol{r}) = \langle N \rangle, \tag{2.33}$$

which are almost identical to those obtained in the canonical ensemble. The radial distribution function is defined in the same way as in the canonical ensemble, with the only difference being the use of the n-particle density of the grand canonical ensemble. The main difference lies in the n-particle density for an ideal gas, which is now the nth power of the number density, i.e. $\rho^n = \varrho^n$. Furthermore, for large distances, the limit $\lim_{r \to \infty} g(r) = 1$ is now obtained for the radial distribution function, which is also reflected in the vanishing pair correlation function for large interparticle distances.

The Ornstein-Zernike equation can be derived through a calculation using Density Functional Theory (DFT). The calculation begins with a Hamiltonian that consists of a kinetic term, a potential term, and a field potential term, similar to the one described above. By integrating the product of the microscopic density $\rho(\boldsymbol{r})$ and the field $\phi(\boldsymbol{r})$, the desired potential field contribution to the Hamiltonian can be obtained. With the chemical potential μ, the intrinsic chemical potential $\psi(\boldsymbol{r}) = \mu - \phi(\boldsymbol{r})$ can be defined. This intrinsic potential is then used to modify the partition function by replacing it with one that contains products of exponentials of the intrinsic potentials, and the n-particle density is modified accordingly. By relating the Helmholtz free energy, $F = U - TS$, to the intrinsic chemical potential, an analogue relationship between the intrinsic free energy $\mathcal{F}$ and F can be established:

$$\mathcal{F} = F - \int \mathrm{d}\boldsymbol{r} \rho^{(1)}(\boldsymbol{r}) \phi(\boldsymbol{r}). \tag{2.34}$$

The main aim is to treat the intrinsic free energy as a functional of the one-particle density and to divide it into an ideal gas contribution and an excess part, i.e.

$$\mathcal{F}[\rho^{(1)}] = \mathcal{F}^{id}[\rho^{(1)}] + \mathcal{F}^{ex}[\rho^{(1)}]. \tag{2.35}$$

The excess part acts as a generating functional for the direct correlation function, which appears in the Ornstein-Zernike equation. The direct correlation function is obtained by taking the second order functional derivative of the excess part:

$$c^{(2)}(\boldsymbol{r}, \boldsymbol{r}') = -\beta \frac{\delta^2 \mathcal{F}^{ex}[\rho^{(1)}]}{\delta \rho^{(1)}(\boldsymbol{r}) \delta \rho^{(1)}(\boldsymbol{r}')}. \tag{2.36}$$

Finally, the Ornstein-Zernike equation is derived by plugging this result into an expression of the density-density correlation function [56].

2.2.2 The Intermediate Scattering Function

In proximity to the glass transition, the viscosity of a liquid increases dramatically with only minor structural alterations observable [51]. Additionally, the rise in viscosity with decreasing temperature is specific to the material, leading to the empirical classification of the

material's fragility. The relaxation dynamics of the system provides a more comprehensive understanding of its physical properties compared to viscosity alone. A measure of this dynamics is the density-density correlation function, also referred to as the intermediate scattering function (ISF). It is defined as follows

$$\Phi_{ll'}(\boldsymbol{q},t) = \left\langle \rho_l(\boldsymbol{q},t=0)^* \rho_{l'}(\boldsymbol{q},t) \right\rangle = \left\langle \rho_l(\boldsymbol{q})^* \, \mathrm{e}^{\Omega^\dagger t} \, \rho_{l'}(\boldsymbol{q}) \right\rangle, \tag{2.37}$$

utilizing the definition of equilibrium average and time evolution of observables established above. In the system being analyzed, the relaxation dynamics is therefore evaluated at inverse length scales of q and time scales t. It is crucial to note that the limit $q \to 0$ corresponds to long-range order correlations that have a significant impact on macroscopic properties such as the mean-squared displacement, whereas the limit $q \to \infty$ corresponds to short-range correlations at the microscopic level. The static correlation function can be defined as the initial ISF. A simple calculation shows that the static correlation function is given by

$$\Phi_{ll'}(\boldsymbol{q}) \equiv \Phi_{ll'}(\boldsymbol{q},t=0) = \delta_{l0}\delta_{l'0}(S(q)-1) + \delta_{ll'}, \tag{2.38}$$

where $S(q)$ corresponds to the aforementioned structure factor for PBP. The static correlation function takes on the form of a diagonal matrix with ones, along the diagonal, except for the entry $(l,l') = (0,0)$ in the middle of the matrix, where the structure factor is located at. Due to the required cutoff of angular indices for numerical computations, the vector space containing this diagonal matrix is fixed at $\mathbb{K} = \mathbb{C}^{(2\Lambda_L+1)\times(2\Lambda_L+1)}$.

In Figure (2.4), the ISF for passive Brownian particles is displayed. Thereby, a uniform scaled grid of $N = 1000$ wave numbers is utilized. It should be noted that these particles are characterized by their lack of swim speed and rotational frequency, and all particles are of the same type. The plot depicts the spatial correlations, with the $(l,l') = (0,0)$ entry of the matrix being displayed. As the packing fraction increases, the dynamics of the system slows down, and at a critical packing fraction of $\eta_c = 0.6963$, the function approaches a constant non-zero value, known as the wave vector dependent nonergodicity parameter $F(q)$, which is shown in Figure (2.5), for the entry $(l,l') = (0,0)$. This indicates that the system is nonergodic, meaning that the particles cannot explore all available phase space.

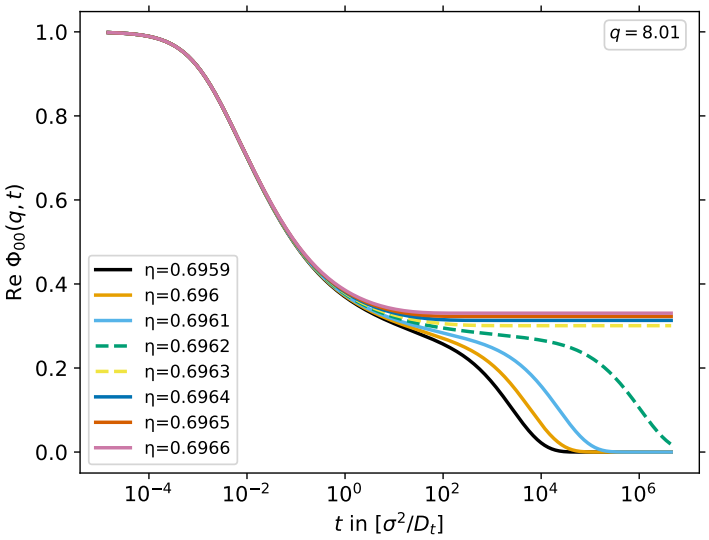

Figure 2.4: Passive ISF, obtained by a passive MCT-implementation for a wave number grid of $M = 1000$ values, for two different wave numbers. The parameters are therefore $\{D_t = 1.0, D_r = 0.0, v = 0.0, \nu = 0.0, \sigma = 1.0\}$.

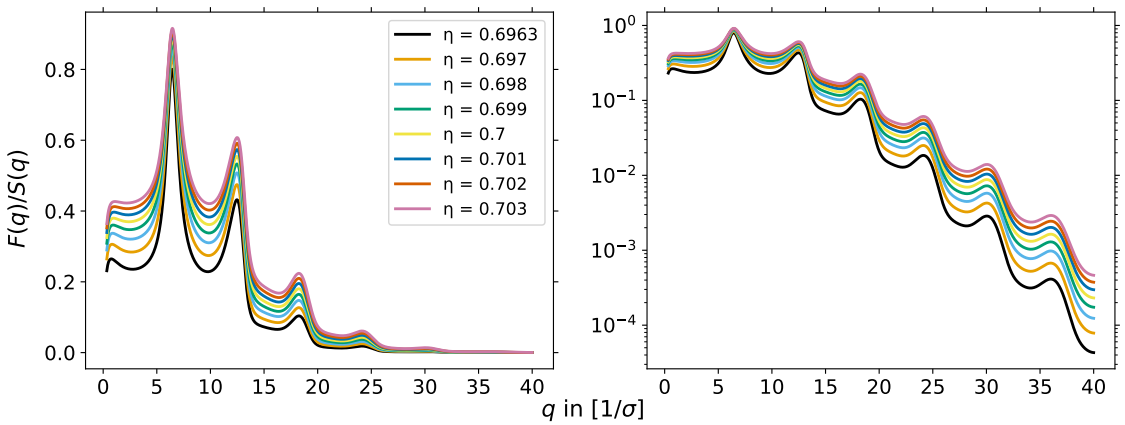

Figure 2.5: Normalized nonergodicity parameter $F(q)/S(q)$ obtained by a passive MCT-implementation, for a wave number grid of $M = 1000$ values, a low q-cutoff of $q_1 = 0.3/\sigma$, a high q-cutoff of $q_M = 40.0/\sigma$, and a particle diameter of $\sigma = 1.0$

This critical packing fraction marks the glass transition from a liquid to a rigid body. To be more precise, it describes the transition from a supercooled liquid to a glass, as the correlation function below the critical packing fraction, shown in Figure (2.4), describes supercooled liquids. The main difference between liquids and supercooled liquids is the relaxation time, with liquids having far quicker correlation times and occurring at lower densities. The relaxation process can be characterized as a three-stage phenomenon. Initially, there is a short-term loss of correlation. Subsequently, the correlation function approaches at a constant value, referred to as β-relaxation regime. If the system is in a glass phase, no further relaxation can be observed, and the nonergodicity parameter assumes the value of the plateau. In this scenario, there is only a two-stage process, comprising the initial loss of correlation and the regime of β-relaxation. Conversely, if the system is a supercooled liquid, the correlation remains frozen for a period of time. This can be imagined as the surrounding particles trapping the particle of interest, thus preventing its motion. After a certain interval, the cages are shattered and a second relaxation process, referred to as α-relaxation, commences. The process concludes when the correlation function falls to zero. Thus, the glass transition can be expressed as a transition of a diverging α-relaxation time.

The system exhibits global invariance under certain transformations. For instance, a global rotation of the system by an angle $\delta\theta$ corresponds to rotating all individual CABP around their center of mass, and their positional vectors, by the same angle. This transformation is denoted by $\theta \mapsto \theta + \delta\theta$, where θ is the system's angle relative to a fixed reference point probed by the x-axis. It should be noted that each CABP angle φ_i is affected by the transformation by $\varphi_i \mapsto \varphi_i + \delta\theta$. The transformation of a vector $\boldsymbol{q}$ is given by $\boldsymbol{q} \mapsto \boldsymbol{q'} = R(\delta\theta)\boldsymbol{q}$, where $R(\delta\theta) \in \mathrm{SO}(2)$ is the rotation matrix. Choosing polar coordinates such that $\boldsymbol{q} = (q, \theta)^T$, the system's density transforms as

$$\rho_l((q, \theta + \delta\theta)^T, t) = u_{ll'}(\delta\theta)\rho_{l'}((q, \theta)^T, t) = \mathrm{e}^{\mathrm{i}\, l\delta\theta}\, \rho_l((q, \theta)^T, t), \tag{2.39}$$

with the unitary matrix $u_{ll'}(\delta\theta) = \delta_{ll'}\, \mathrm{e}^{\mathrm{i}\, l\delta\theta}$. The vectors $\boldsymbol{q}$ and $\boldsymbol{r}_i$ transform with $R(\delta\theta)$, and their combination in the density is invariant under such transformations due to their appearance in the inner product only. Concerning the ISF, one should note that

$$\Omega^\dagger(\theta)\rho_l((q, \theta)^T, t) = \Omega^\dagger(\theta + \delta\theta)\rho_l((q, \theta + \delta\theta)^T, t). \tag{2.40}$$

This equality is valid because of the correction of the angular derivative terms in the Smoluchowski operator. Therefore the transformation of the correlator is given by

$$\Phi_{ll'}((q,\theta+\delta\theta)^T,t) = u^\dagger_{lm}(\delta\theta)\Phi_{mn}((q,\theta)^T,t)u_{nl'}(\delta\theta) = \mathrm{e}^{-\,\mathrm{i}(l-l')\delta\theta}\,\Phi_{ll'}((q,\theta)^T,t). \quad (2.41)$$

The transformation behavior described above provides a significant advantage from a numerical perspective. It allows one to eliminate the dependence on the wave vector and replace it with its length and a phase factor that contains all relevant information. In the subsequent sections, it will be demonstrated that other dependent quantities can also be transformed in a similar manner. The procedure is as follows: First, the equations are presented in their general form, and then, in the following chapter, their transformed version in the x-direction is discussed.

2.2.3 The Mori-Zwanzig Equation

The CABP model belongs to a class of models that describe glass-forming liquids, with a focus on collective density modes. Mori and Zwanzig employed a projection scheme [52] to separate the problem into two mutually orthogonal subspaces: one that contains the density modes of interest and one that contains everything else. The projector that projects onto the density modes is denoted as P_1, and its orthogonal counterpart with respect to P_1 is denoted as $Q_1 = \mathrm{Id} - P_1$. In the basis of density functions, P_1 is given by the following expression

$$P_1 = \sum_{ll'\boldsymbol{q}} \Big|\rho_l(\boldsymbol{q})\Big\rangle \Phi^{-1}_{ll'}(\boldsymbol{q}) \Big\langle\rho_{l'}(\boldsymbol{q})\Big|, \quad P_1 + Q_1 = \mathrm{Id}\,. \quad (2.42)$$

Here, the Bra-Ket notation is used to represent the equilibrium inner product $\langle A|B\rangle = \langle A^*B\rangle$. The presence of the inverse static correlation function in the above equation accounts for the idempotency $P_1^2 = P_1$ of the projection operator. It should be noted that the application of the orthogonal projector Q_1 on a density yields zero, i.e., $Q_1\,|\rho_l(\boldsymbol{q})\rangle = 0$. Taking the time derivative of the exponential function that appears in the ISF and inserting the identity $\mathrm{Id} = P_1 + Q_1$ twice

$$\partial_t\,\mathrm{e}^{\Omega^\dagger t} = \mathrm{e}^{\Omega^\dagger t}\,\Omega^\dagger = \mathrm{e}^{\Omega^\dagger(P_1+Q_1)t}(P_1+Q_1)\Omega^\dagger \quad (2.43)$$

is a first step towards obtaining a first-order, time-dependent equation of motion for the ISF. The last term in the equation can be rewritten using what is known as a *Dyson decomposition*, which takes the form

$$\mathrm{e}^{\Omega^\dagger(P_1+Q_1)t} = \mathrm{e}^{\Omega^\dagger Q_1 t} + \int_0^t \mathrm{d}t'\,\mathrm{e}^{\Omega^\dagger Q_1(t-t')}\,\Omega^\dagger P_1\,\mathrm{e}^{\Omega^\dagger t'}\,. \quad (2.44)$$

By applying both equations to the time derivative of the ISF, the *Mori-Zwanzig* equation of motion is obtained, which is given by

$$\partial_t\Phi(\boldsymbol{q},t) = -\omega(\boldsymbol{q})\Phi^{-1}(\boldsymbol{q})\Phi(\boldsymbol{q},t) + \int_0^t dt' K(\boldsymbol{q},t-t')\Phi^{-1}(\boldsymbol{q})\Phi(\boldsymbol{q},t'). \quad (2.45)$$

Thereby, the angular indices are omitted for clarity. The frequency matrix

$$\omega_{ll'}(\boldsymbol{q}) = -\Big\langle\rho_l(\boldsymbol{q})^*\Omega^\dagger\rho_{l'}(\boldsymbol{q})\Big\rangle = \delta_{ll'}(D_t q^2 + D_r l^2 - \mathrm{i}\,l\nu) - \frac{\mathrm{i}\,qv}{2}\delta_{|l-l'|,1}\,\mathrm{e}^{-\,\mathrm{i}(l-l')\theta_q}\,S_{ll}(q), \quad (2.46)$$

is defined as the previous expression utilizing a single adjoint Smoluchowski operator. The angle between the system and the x-axis is denoted as θ_q. Finally, the dissipative integral kernel that appears in the convolution integral and is called the *diffusion kernel*, is given by

$$K(\boldsymbol{q},t) = \Big\langle\rho_l^*(\boldsymbol{q})\Omega^\dagger Q_1\,\mathrm{e}^{\Omega^\dagger Q_1 t}\,Q_1\Omega^\dagger\rho_{l'}(\boldsymbol{q})\Big\rangle\,. \quad (2.47)$$

The projector denoted by Q_1 is idempotent, which implies that the diffusion kernel can be expressed in a slightly different form by expanding the exponential function and selectively including or excluding corresponding projectors. As a result, it holds that $Q_1\,\mathrm{e}^{\Omega^\dagger Q_1 t} = Q_1\,\mathrm{e}^{\Omega^\dagger Q_1 t}\,Q_1$ and similar expressions can be obtained analogous. When the interaction between particles disappears, the diffusion kernel also disappears, i.e., $K(\boldsymbol{q},t)$ vanishes. Formally, this can be seen by the commutation of Q_1 and $\Omega^\dagger_{\text{free}}$, where the subscript indicates that the interaction term of the Smoluchowski operator equals zero. Since the microscopic density is entailed in the kernel of Q_1, the application of the projector on the density yields zero. Under this circumstance, the Mori-Zwanzig equation reduces to a simple differential equation

$$\partial_t \Phi(\boldsymbol{q},t) = -\omega(\boldsymbol{q})\Phi^{-1}(\boldsymbol{q})\Phi(\boldsymbol{q},t). \tag{2.48}$$

This equation can be solved by an exponentially decaying ISF

$$\Phi(\boldsymbol{q},t) = \mathrm{e}^{-\omega(\boldsymbol{q})\Phi^{-1}(\boldsymbol{q})t}\,\Phi(\boldsymbol{q}), \tag{2.49}$$

starting from the initial condition that the ISF is described by the static correlation function. The numerical solution method utilizes this free particle solution, as on short time scales, which are much shorter than any interaction time scales, each particle is approximately free and does not scatter.

The diffusion kernel must be approximated in order to solve the Mori-Zwanzig equation. For that purpose the *mode-coupling-theory* of the glass transition is used. Unfortunately, the diffusion kernel turns out to be not well suited for any approximation. To explain that point, the definition of the Laplace transformation of a scalar function $f : [0,\infty) \to \mathbb{C}$ is repeated. The Laplace transform $\tilde{f}(z)$ is given by

$$\tilde{f}(z) = \int_0^\infty \mathrm{d}t\,\mathrm{e}^{-zt}\,f(t), \tag{2.50}$$

and it's two major properties of interest for this discussion here are the factorization of the convolution integral under the transformation and the limit theorem $\lim_{t\to\infty} f(t) = \lim_{z\to 0} z\tilde{f}(z)$. Transforming the Mori-Zwanzig equation yields an expression

$$z\tilde{\Phi}(\boldsymbol{q},z) - \tilde{\Phi}(\boldsymbol{q}) = -\tilde{\omega}(\boldsymbol{q})\tilde{\Phi}^{-1}(\boldsymbol{q})\tilde{\Phi}(\boldsymbol{q},z) + \tilde{K}(\boldsymbol{q},z)\tilde{\Phi}^{-1}(\boldsymbol{q})\tilde{\Phi}(\boldsymbol{q},z), \tag{2.51}$$

that can be rearranged in the form

$$\tilde{\Phi}(\boldsymbol{q},z) = \Big[z\,\mathrm{Id} + \tilde{\omega}(\boldsymbol{q})\tilde{\Phi}^{-1}(\boldsymbol{q}) - \tilde{K}(\boldsymbol{q},z)\tilde{\Phi}^{-1}(\boldsymbol{q})\Big]^{-1}\,\tilde{\Phi}(\boldsymbol{q}). \tag{2.52}$$

This is some interesting result. If the relaxation time diverges, the glass transition shows itself by the convergence of the ISF to the nonergodicity parameter. According to the limit theorem of Laplace transformation this means that the transformed ISF must have a $1/z$ pole. Above's equation shows that an equivalent statement is that the limit $\lim_{z\to 0}\tilde{K}(\boldsymbol{q},z) = \tilde{\omega}(\boldsymbol{q})$ exists. Any further approximation of the kernel would easily violate this property. Therefore, the proceeding step introduced in the case of passive Brownian particles by Szamel and Löwen [53] is to approximate the full equation by a further projection, mathematically driven by the projector P_2, that makes the approximation for the diffusion kernel possible. If the new kernel is denoted by $\tilde{M}(\boldsymbol{q},z)$ the projection should yield the feature $\lim_{z\to 0}\tilde{M}(\boldsymbol{q},z) = \infty$, that is more robust under further approximations. Furthermore, an CABP is a two dimensional particle. That means that even in the glassy state the rotational degrees of freedom never be subject to dynamical arrest. The projector

P_2 therefore only entails the translational part $\Omega_T^\dagger$ of the Smoluchowski operator as well as the translational part $\omega_T^{-1}(\boldsymbol{q})$ of the inverse frequency matrix and reads

$$P_2 = -\sum_{ll'\boldsymbol{q}} \Big|\rho_l(\boldsymbol{q})\Big\rangle \omega^{-1}_{T,ll'}(\boldsymbol{q}) \Big\langle \rho_{l'}(\boldsymbol{q})\Big|\Omega_T^\dagger, \quad P_2 + Q_2 = \mathrm{Id}\,. \tag{2.53}$$

The inverse frequency matrix that appears in the equation is problematic in cases for models like that of CABP or ABP for that it's matrix representation does not equal that of a diagonal matrix that can easily be inverted. This point is going to be discussed later in Chapter (3), where an analytic inversion of the frequency matrix is performed. The appearance of that inverse matrix ensures to conserve the needed projection operators feature of idempotency. The projection step uses a further Dyson composition by rewriting the adjoint Smoluchowski operator that appears in the exponential function in the diffusion kernel as $\Omega^\dagger = \Omega^\dagger(P_2 + Q_2)$. This leads to an equation of motion

$$K(\boldsymbol{q},t) = M(\boldsymbol{q},t) - \int_0^\infty \mathrm{d}t' K(\boldsymbol{q},t-t')\omega_T^{-1}(\boldsymbol{q})M(\boldsymbol{q},t'), \tag{2.54}$$

that involves the so called *friction kernel*

$$M(\boldsymbol{q},t) = \Big\langle \rho_l^*(\boldsymbol{q})\Omega_T^\dagger Q_1\, \mathrm{e}^{\Omega^\dagger_{\mathrm{irr}} t}\, Q_1 \Omega_T^\dagger \rho_{l'}(\boldsymbol{q})\Big\rangle, \tag{2.55}$$

with the adjoint irreducible Smoluchowski operator $\Omega^\dagger_{\mathrm{irr}} = \Omega^\dagger Q_2$. Moreover, the two adjoint Smoluchowski operators that are present on either side of the exponential function in the equation above have been substituted by their translational components. The complete operator comprises of its translational and rotational components. If the operator is expressed as a sum, it becomes evident that the outcome of applying the operator on the right to a density function generates a density function that is included in the set of density functions

$$\Omega_R^\dagger \rho_{l'}(\boldsymbol{q}) \in \mathrm{span}\Big\{\rho_{l'}(\boldsymbol{q})\Big\}. \tag{2.56}$$

The subsequent operation of the operator Q_1 on that density function results in zero. Consequently, the operator can be replaced by its translational part. Similarly, the operator that appears on the left side of the exponential function can also be substituted by its translational part. However, the rationale behind this substitution is more complex and necessitates the evaluation of the inner product $\Big\langle A(\Gamma)\Big|\Omega_R^\dagger B(\Gamma)\Big\rangle$, where $A(\Gamma)$ and $B(\Gamma)$ indicate two distinct observables on the phase space Γ. The concept is to divide the operator into its equilibrium and non-equilibrium parts and demonstrate that it is self-adjoint and skew-adjoint, respectively. The calculation assumes that the observables have compact support, which ensures that the surface terms appearing in partial integration vanish. If the expectation value of the friction kernel is replaced by a corresponding inner product, the Smoluchowski operator can be incorporated into the dual vector. The fact that it is self-adjoint or skew-adjoint implies that it can be substituted by its original form, which yields an element of the set of density functions if applied to such a function, up to a minus sign in one case. As the projector is also self-adjoint, its subsequent application results in zero. Consequently, both adjoint Smoluchowski operators can be replaced by their translational parts. The calculation of the Laplace transform of the equation of motion can be performed as a result

$$K(\boldsymbol{q},z) = \Big(M^{-1}(\boldsymbol{q},z) + \omega_T^{-1}(\boldsymbol{q})\Big)^{-1}. \tag{2.57}$$

This outcome can be incorporated into the Mori-Zwanzig equation, resulting in the equation

$$\partial_t \Phi(\boldsymbol{q},t) = -\omega(\boldsymbol{q})\Phi^{-1}(\boldsymbol{q})\Phi(\boldsymbol{q},t) - \int_0^t dt' m(\boldsymbol{q},t-t')\Big(\partial_{t'}\Phi(\boldsymbol{q},t') + \omega_R(\boldsymbol{q})\Phi^{-1}(\boldsymbol{q})\Phi(\boldsymbol{q},t')\Big). \tag{2.58}$$

The memory kernel $m(\boldsymbol{q},t) = M(\boldsymbol{q},t)\omega_T^{-1}(\boldsymbol{q})$ plays a critical role in this study and has only rotational contributions through the irreducible Smoluchowki operator. The coupling between rotational and translational motion is examined by the additional term $\omega_R(\boldsymbol{q})\Phi^{-1}(\boldsymbol{q})\Phi(\boldsymbol{q},t)$, referred to as the hopping term, which appears in the equation of motion. To ensure stability under further approximations of the friction kernel, this equation can be Laplace transformed, revealing the desired feature $\lim_{z\to 0}\tilde{M}(\boldsymbol{q},z) = \infty$.

It is worth noting that if there is no differentiation between the rotational and translational components, as described by Liluashvili [55], the hopping term is not obtained, and separate relaxation pathways for translational and rotational motion are not observed. Therefore, the hopping term accounts for these separate pathways, whereby the translational motion can be impeded and influenced by the rotational degrees of freedom, while the rotational motion remains ergodic and entirely independent of the translational motion, at least for time scales exceeding the rotational relaxation time.

2.2.4 The MCT-Approximation

In order to acquire any valuable outcome, the approximation of the memory kernel becomes imperative. A conceivable approach is the *mode-coupling theory* approximation, formulated by Götze for glassy systems [54]. This approximation is designed to account for the phenomenon that accompanies the glass transition, namely the formation of enclosures or *cages*. Consequently, when considering spherical particles of a single component, an approximation of pairwise interactions emerges as a plausible assumption. It is worth noting that there are generalized versions that incorporate projections onto n-density modes [61]. To integrate this characteristic into the theory, a projector

$$P = \frac{1}{2}\sum_{1234}\Big|\rho_1\rho_2\Big\rangle\Phi_{24}^{-1}\Phi_{13}^{-1}\Big\langle\rho_3\rho_4\Big|, \quad P+Q = \mathrm{Id}, \tag{2.59}$$

is employed, which projects onto density pairs. Here, the shorthand notation $\sum_i \equiv \sum_{l_i\boldsymbol{q}_i}$ and

$$\Phi_{ij}(t) \equiv \Phi_{l_il_j}(\boldsymbol{q}_i,\boldsymbol{q}_j,t) = \Phi_{l_il_j}(\boldsymbol{q}_i,t)\delta_{\boldsymbol{q}_i\boldsymbol{q}_j}\delta_{l_il_j}, \tag{2.60}$$

is used. When this projector is applied to the friction kernel, on both sides of the exponential function, the resultant equation

$$\begin{aligned} M_{ll'}(\boldsymbol{q},t) &\approx \Big\langle\rho_l^*(\boldsymbol{q})\Omega_T^\dagger Q_1 P\,\mathrm{e}^{\Omega_{\mathrm{irr}}^\dagger t}\,PQ_1\Omega_T^\dagger\rho_{l'}(\boldsymbol{q})\Big\rangle \\ &= \frac{1}{4}\sum_{\substack{1234\\1'2'3'4'}}\Big\langle\rho_l^*(\boldsymbol{q})\Omega_T^\dagger Q_1\rho_1\rho_2\Big\rangle\Phi_{24}^{-1}\Phi_{13}^{-1}\Big\langle\rho_3^*\rho_4^*\,\mathrm{e}^{\Omega_{\mathrm{irr}}^\dagger t}\,\rho_{1'}\rho_{2'}\Big\rangle\Phi_{2'4'}^{-1}\Phi_{1'3'}^{-1}\Big\langle\rho_{3'}^*\rho_{4'}^*Q_1\Omega_T^\dagger\rho_{l'}(\boldsymbol{q})\Big\rangle \end{aligned} \tag{2.61}$$

is obtained as an approximation [55]. However, the MCT-approximation entails an additional approximation, which becomes necessary to compute the newly introduced four-point function

$$\Big\langle\rho_3^*\rho_4^*\,\mathrm{e}^{\Omega_{\mathrm{irr}}^\dagger t}\,\rho_{1'}\rho_{2'}\Big\rangle \approx \Phi_{31'}(t)\Phi_{42'}(t) + \Phi_{32'}(t)\Phi_{41'}(t). \tag{2.62}$$

In this approximation, the irreducible Smoluchowski operator is substituted with the conventional one, and a factorization technique is employed to approximate the four-point function as a sum of two two-point functions [54].

Upon scrutiny of the approximated friction kernel, one may discern that the approximation exhibits irregular behavior and lacks guaranteed convergence. The prevailing argument

posits that the theory's success in accurately describing the formation of confinement structures during dynamical arrest [62], as well as exhibiting characteristics such as multistep relaxation patterns, stretched exponentials, and burgeoning dynamical length scales [62–64], validates its application. The approximation can be regarded as an ad hoc approximation, purely and solely a most rudimentary approximation that can be conceived. If one were to forgo projecting onto density pairs and instead focus on individual densities, the friction kernel would diminish. This is due to the presence of orthogonal projectors Q_1, which annihilate any density they act upon. However, this behavior differs when dealing with two-point densities. The replacement of the irreducible Smoluchowski operator with the conventional one can be justified mathematically. Failure to make this substitution would also yield a vanishing outcome, as the single density modes $\rho(\boldsymbol{q}_3, t)$ and $\rho(\boldsymbol{q}_4, t)$, which originate within the slow subspace, would otherwise contribute zero.

In order to compute the friction kernel, three essential steps must be undertaken. The initial step forms part of the MCT-approximation and has been previously discussed. It involves approximating the four-point function as a summation of two two-point functions. The remaining two steps entail the computation of the two remaining averages that emerge. It becomes evident that the inclusion of the orthogonal projector into the terms results in static triplet correlation functions. The *Kirkwood superposition approximation* (KSA), initially proposed to derive a closure for an integral equation governing the pair correlation function [65], proves relevant here. The KSA asserts that the potential of mean force for three particles can be approximated as the sum of the potential of mean forces for pairs of particles. In our case, the potential is represented by a hard disk potential. Consequently, the direct triplet correlations contributing to the static triplet correlation function can be disregarded, yielding the following equations

$$\begin{aligned}\langle \rho_1^* \rho_2 \rho_3 \rangle &\approx \frac{1}{\sqrt{N}} \Phi_{l_1 l_1}(\boldsymbol{q}_1) \Phi_{l_2 l_2}(\boldsymbol{q}_2) \Phi_{l_3 l_3}(\boldsymbol{q}_3) \delta_{\boldsymbol{q}_1, \boldsymbol{q}_2 + \boldsymbol{q}_3} \delta_{l_1, l_2 + l_3}, \\ \langle \rho_1^* \rho_2^* \rho_3 \rangle &\approx \frac{1}{\sqrt{N}} \Phi_{l_1 l_1}(\boldsymbol{q}_1) \Phi_{l_2 l_2}(\boldsymbol{q}_2) \Phi_{l_3 l_3}(\boldsymbol{q}_3) \delta_{\boldsymbol{q}_1 + \boldsymbol{q}_2, \boldsymbol{q}_3} \delta_{l_1 + l_2, l_3}.\end{aligned} \tag{2.63}$$

Equipped with this knowledge, the friction kernel can be calculated, which can be expressed as

$$M_{ll'}(\boldsymbol{q}, t) \approx \frac{\varrho}{2} \int \frac{\mathrm{d}^2 k}{(2\pi)^2} \sum_{l_1 l_2 l_3 l_4} \mathcal{V}^L_{l l_1 l_2}(\boldsymbol{q}, \boldsymbol{k}, \boldsymbol{p}) \Phi_{l_1 l_3}(\boldsymbol{k}, t) \Phi_{l_2 l_4}(\boldsymbol{p}, t) \mathcal{V}^R_{l' l_3 l_4}(\boldsymbol{q}, \boldsymbol{k}, \boldsymbol{p}). \tag{2.64}$$

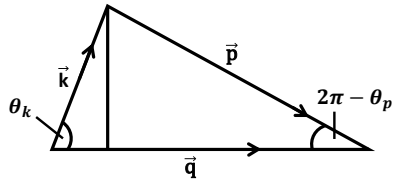

Figure 2.6: Wave vector restriction and the definition of the angles.

Thereby, it can be used that the calculation of the vertices reveals a restriction on the wave vector $\boldsymbol{q} = \boldsymbol{k} + \boldsymbol{p}$, illustrated in Figure (2.6). The left vertex is defined as

$$\mathcal{V}^L_{l l_1 l_2}(\boldsymbol{q}, \boldsymbol{k}, \boldsymbol{p}) = \mathcal{V}_{l l_1 l_2}(\boldsymbol{q}, \boldsymbol{k}, \boldsymbol{p}) + \delta \mathcal{V}_{l l_1 l_2}(\boldsymbol{q}, \boldsymbol{k}, \boldsymbol{p}), \tag{2.65}$$

and contains the equilibrium part

$$\mathcal{V}_{l l_1 l_2}(\boldsymbol{q}, \boldsymbol{k}, \boldsymbol{p}) = D_t \delta_{l, l_1 + l_2} \Big[(\boldsymbol{q} \cdot \boldsymbol{k}) c(k) \delta_{l_1 0} + (\boldsymbol{q} \cdot \boldsymbol{p}) c(p) \delta_{l_2 0} \Big], \tag{2.66}$$

and the non-equilibrium contribution

$$\begin{aligned}\delta\mathcal{V}_{ll_1l_2}(\boldsymbol{q},\boldsymbol{k},\boldsymbol{p}) = \frac{\mathrm{i}\,v}{2\varrho}\delta_{|l_1+l_2-l|,1}\Phi_{ll}(q)\Big[&k\,\mathrm{e}^{\mathrm{i}(l_1+l_2-l)\theta_k}\,\Phi_{l-l_2,l-l_2}(k)\Phi^{-1}_{l_1l_1}(k)\\ &+ p\,\mathrm{e}^{\mathrm{i}(l_1+l_2-l)\theta_p}\,\Phi_{l-l_1,l-l_1}(p)\Phi^{-1}_{l_2l_2}(p) - q\,\mathrm{e}^{\mathrm{i}(l_1+l_2-l)\theta_q}\Big],\end{aligned} \tag{2.67}$$

that entails specific components of the static correlation function $\Phi_{l_il_i}(q_i)$. The right vertex is equal to the equilibrium contribution of the left vertex and reads

$$\mathcal{V}^R_{l'l_3l_4}(\boldsymbol{q},\boldsymbol{k},\boldsymbol{p}) = D_t\delta_{l',l_3+l_4}\Big[(\boldsymbol{q}\cdot\boldsymbol{k})c(k)\delta_{l_30} + (\boldsymbol{q}\cdot\boldsymbol{p})c(p)\delta_{l_40}\Big]. \tag{2.68}$$

These equations are revisited in the next chapter, where they are simplified by means of symmetry features. The vertices coincide with those of active Brownian particles [23]. This observation is not surprising, considering that the rotational frequency ν holds a mathematical role akin to the rotational diffusion constant.

2.3 The MCT-Equation of Tagged Particles

In the following investigation, the focus is set on the self-intermediate scattering function (SISF) for chiral active Brownian particles. This function describes a tagged tracer particle, which stands out from the surrounding particles in the bath due to its unique model parameters, except for its size. The set of system parameters is denoted by $\{D_t^s, D_r^s, v^s, \nu^s\}$. This system can be conceptualized as a two-component system, with one particle exhibiting distinct characteristics. This feature proves advantageous in experiments and simulations as it allows for the extraction of the dynamics of a single particle, which is considerably simpler than describing the dynamics of the entire collective system. Reichert [23] extended the MCT-equations for active Brownian particles to accommodate mixtures of particles. In this study, these equations are revisited and slightly modified by incorporating the rotational term to account for chiral active motion. For a more comprehensive introduction, the original work is referred to.

To incorporate the tagged particle within a bath of other particles, it is logical to consider the phase space as consisting of two parts: that of the single tagged particle Γ_s and that of all the other particles Γ_b. The cartesian product of these two sets gives rise to the total phase space $\Gamma = \Gamma_s \times \Gamma_b$. In the case of mixtures, where multi-component systems are considered, it is possible to define a microscopic density function that differs from the conventional density function only in its specific description and normalization for a particular type of particle. The density can be expressed as follows

$$\rho^\alpha(\boldsymbol{r},\varphi,t) = \frac{1}{\sqrt{N_\alpha}}\sum_{i=1}^{N_\alpha}\delta(\boldsymbol{r}-\boldsymbol{r}_i^\alpha(t))\;\delta(\varphi-\varphi_i^\alpha(t)). \tag{2.69}$$

Here, N_α represents the number of particles of type α. This density can undergo Fourier transform into the wave vector domain, similar to the density of a one-component system. Upon closer examination, it becomes evident that the ISF encompasses two distinct densities associated with different particle types. Consequently, its host space expands to include two additional vector spaces, each corresponding to the number of particles in a particular species. The equations governing the ISF and the MCT-equation incorporate additional terms arising from these new correlations. A key element is the modified direct correlation function $c^{\alpha\beta}(q)$, which incorporates inter-particle correlations between different types [23].

Proceeding, a fluctuating density resolved by concentration is introduced, resulting in a concentration-scaled ISF given by

$$\tilde{\rho}_l^\alpha(\boldsymbol{q}) \equiv \frac{1}{\sqrt{x_\alpha}}\rho_l^\alpha(\boldsymbol{q}), \quad \tilde{\Phi}_{ll'}^{\alpha\beta}(\boldsymbol{q},t) \equiv \frac{1}{\sqrt{x_\alpha x_\beta}}\Phi_{ll'}^{\alpha\beta}(\boldsymbol{q},t). \tag{2.70}$$

Here, $x_\alpha = N_\alpha/N$ represents the ratio of particles of a specific type to the total number of particles. With this formulation, the SISF between particles can be defined as

$$\tilde{\Phi}_{ll'}^{ss}(\boldsymbol{q},t) \equiv \Phi_{ll'}^{s}(\boldsymbol{q},t) = \left\langle \tilde{\rho}_l^s(\boldsymbol{q})^* \, \mathrm{e}^{\Omega^\dagger t} \, \tilde{\rho}_{l'}^s(\boldsymbol{q}) \right\rangle. \tag{2.71}$$

This SISF corresponds to the ISF evaluated for correlations involving the tracer particle itself. The Smoluchowski operator serves as a generalization of the previously introduced operator to accommodate multicomponent mixtures. The only distinction lies in splitting the sum over all particles into a sum over particles of a single type and a sum over particle types. In the current context, the operator can be divided, analogous to the phase space, into two parts: one describing the bath and the other describing the tracer particle. This division can be expressed as $\Omega = \Omega_s + \Omega_b$, where

$$\Omega_s = \boldsymbol{\nabla}_s(\boldsymbol{\nabla}_s - \beta \boldsymbol{F}_s) + D_r^s \partial_{\varphi_s}^2 - v^s \boldsymbol{\nabla} \cdot \boldsymbol{o}_s - \nu^s \partial_{\varphi_s}. \tag{2.72}$$

The tagged frequency matrix can be calculated with the help of the concentration-resolved density functions. It is obtained by substituting the system parameters with those of the tracer particle, i.e.

$$\omega_{T,ll'}^s(\boldsymbol{q}) = D_t^s q^2 \delta_{ll'} - \frac{\mathrm{i}\, q v^s}{2}\delta_{|l-l'|,1}\, \mathrm{e}^{-\mathrm{i}(l-l')\theta_q}, \quad \omega_{R,ll'}^s = \delta_{ll'}(D_r^s l^2 - \mathrm{i}\, l \nu^s). \tag{2.73}$$

In leading order of x_s, the inverse static correlation function can be expressed as

$$\tilde{\Phi}^{-1}(\boldsymbol{q}) = \begin{pmatrix} \mathrm{Id}_{2\Lambda+1} & -\varrho c^{bs}(q)\sqrt{x_s} \\ -\varrho c^{sb}(q)\sqrt{x_s} & (\tilde{\Phi}^{-1})^{bb}(q) \end{pmatrix}. \tag{2.74}$$

This inversion can be performed like any standard block matrix inversion, resulting in

$$\tilde{\Phi}(\boldsymbol{q}) = \begin{pmatrix} \mathrm{Id}_{2\Lambda+1} & -\varrho \tilde{\Phi}^{bb}(q) c^{bs}(q)\sqrt{x_s} \\ -\varrho c^{sb}(q)\tilde{\Phi}^{bb}(q)\sqrt{x_s} & \tilde{\Phi}^{bb}(q) \end{pmatrix} + \mathcal{O}(x_s). \tag{2.75}$$

This general form applies to all relevant quantities of interest. It has been shown [23] that the frequency matrix and the memory kernel share the same structure. The memory kernel governs the dynamics by accounting for interactions and capturing the coupling between the bath and the tracer within the theory. In the thermodynamic limit, when there is only one tracer particle in a large bath of surrounding host particles, its influence on the bath dynamics should be minimal. Therefore, the mathematical behavior where the coupling to all tracer variables vanishes as $x_s \to 0$ is physically plausible. Extracting the (s,s)-component of the MCT-equation yields the MCT-equation for the SISF of a tracer particle in a host environment, which can be expressed as

$$\partial_t \Phi^s(\boldsymbol{q},t) = -\omega^s(\boldsymbol{q})\Phi^s(\boldsymbol{q},t) - \int_0^t dt' m^s(\boldsymbol{q},t-t')\Big(\partial_{t'}\Phi^s(\boldsymbol{q},t') + \omega_R^s(\boldsymbol{q})\Phi^s(\boldsymbol{q},t')\Big). \tag{2.76}$$

This equation only differs form the MCT-equation (2.58) by the missing inverse static correlation function terms. Actually, there is no difference between both equations, since the tracer-tracer component of the static correlation function is equal to the identity matrix, what can be seen by simply evaluating the equilibrium average of the SISF. The inverse static correlation functions are therefore just left away. Here, the inverse translational

frequency matrix was absorbed again into the memory kernel $m^s(\boldsymbol{q},t) = M^s(\boldsymbol{q},t)(\omega_T^s)^{-1}(\boldsymbol{q})$. The current focus is that of a monodisperse system. The friction kernel for a mixed system is given in Reference [23], while that of a monodisperse system is given by

$$M^s_{ll'}(\boldsymbol{q},t) \approx \varrho \int \frac{\mathrm{d}^2k}{(2\pi)^2} \sum_{l_1 l_2} \mathcal{V}^s_{ll_1l_2}(\boldsymbol{q},\boldsymbol{k}) \Phi^s_{l_2l'}(\boldsymbol{p},t) \Phi_{l_10}(\boldsymbol{k},t). \tag{2.77}$$

It differs from the friction kernel of the bath in the property that it only entails a single vertex. It also entails the SISF $\Phi^s_{l_2l'}$, that can be calculated by solving the corresponding MCT-equation numerically and that entails the ISF Φ_{l_10} that must be calculated at first by solving its MCT-equation (2.58). The vertex can be split into an equilibrium and non-equilibrium part like

$$\mathcal{V}^s_{ll_1l_2}(\boldsymbol{q},\boldsymbol{k}) = \mathcal{V}^s_{\mathrm{eq},ll_1l_2}(\boldsymbol{q},\boldsymbol{k}) + \delta\mathcal{V}^s_{ll_1l_2}(\boldsymbol{q},\boldsymbol{k}), \tag{2.78}$$

which are given, also for the monodisperse system, by

$$\begin{aligned} \mathcal{V}^s_{\mathrm{eq},ll_1l_2}(\boldsymbol{q},\boldsymbol{k}) &= \delta_{ll_2}\delta_{l_10}\Big[D^s_t c(k)(\boldsymbol{q}\cdot\boldsymbol{k})\Big]^2, \\ \delta\mathcal{V}^s_{ll_1l_2}(\boldsymbol{q},\boldsymbol{k}) &= \frac{iD^s_t}{2}\delta_{|l_1+l_2-l|,1} k\, \mathrm{e}^{\mathrm{i}(l_1+l_2-l)\theta_k}\, c^2(k)(\boldsymbol{q}\cdot\boldsymbol{k})\Big(vS(k)\delta_{ll_2} - v^s\delta_{l_10}\Big). \end{aligned} \tag{2.79}$$

Thereby, $S(k)$ denotes the static structure factor of the bath.

3. Symmetry Transformations

In the preceding chapter, the MCT-equations were introduced for chiral active Brownian particles, separately for the intermediate and self-intermediate scattering functions. The objective of this chapter is to simplify these equations through the utilization of symmetry transformations. Initially, the focus is on obtaining an analytical expression for the inverse translational frequency matrix dependent on the wave vector in the x-direction. Subsequently, the MCT-equation and its components are reformulated in a manner that incorporates the rotation of the wave vector in the x-direction. This reformulation ensures that the equations solely rely on the vector's magnitude and phase terms, that encompass the directional dependence. Finally, it is demonstrated that for non-chiral active particles, a symmetry transformation can be employed. This transformation enables the calculation of an MCT-equation for the ISF or SISF while encapsulating the complex nature of the scattering functions solely through a prefactor, treating all other quantities as real.

3.1 The Inverse Frequency Matrix

The translational frequency matrix depends on the wave vector $\boldsymbol{q}$. It can be transformed such that the vector points in the x-direction. The matrix then reads

$$\omega_{T,ll'}(q) = -\left\langle \rho_l^*(q)\Omega_T^\dagger \rho_{l'}(q)\right\rangle = \delta_{ll'}D_t q^2 - \frac{\mathrm{i}\,qv}{2}\delta_{|l-l'|,1}S_{ll}(q). \tag{3.1}$$

The rotational frequency matrix is a diagonal matrix $\omega_{R,ll'}(q) = \delta_{ll'}(D_r l^2 - il\nu)$ and its inverse is trivial. The inverse matrix $\omega^{-1}_{T,ll'}(q)$ is problematic in cases for models like that of CABP for that its matrix representation does not equal that of a diagonal matrix that can easily be inverted. Since taking a cutoff and inverting a matrix is in general a non-commutative operation one has to invert it before taking a cutoff. This can be done by applying the Sherman-Morrison formula [66] to the matrix. To do so, one observes that the translational frequency matrix can be written as $\omega = \omega^s + \boldsymbol{u}\boldsymbol{v}^T$, where

$$\begin{aligned} &u_0 = -iqv/2(S(q)-1), \quad \boldsymbol{u}_l = \delta_{l0}u_0, \\ &\boldsymbol{v}_l = \delta_{1l} + \delta_{-1l}, \quad (\boldsymbol{u}\boldsymbol{v}^T)_{ll'} = u_0\delta_{l0}(\delta_{1l'} + \delta_{-1l'}). \end{aligned} \tag{3.2}$$

By defining $\Delta = \sqrt{(D_t q^2)^2 + (qv)^2}$ one can write

$$(\omega_T^s)^{-1}_{ll'}(q) = \frac{(iqv)^{|l-l'|}}{\Delta(D_t q^2 + \Delta)^{|l-l'|}}, \tag{3.3}$$

as the inverse tagged translational frequency matrix, that corresponds to the inverse translational frequency matrix of a single tracer particle. This formula can be derived, cf. (A.1), by noting that the tagged translational frequency matrix has the form of a matrix representation of a Laurent operator [67] whose symbol curve is an ellipsis and that can be

inverted analytically. The Sherman-Morrison formula now yields

$$\begin{aligned}\omega^{-1}_{T,ll'} = (\omega^s + \boldsymbol{u}\boldsymbol{v}^T)^{-1}_{ll'} &= \left((\omega^s_T)^{-1} - \frac{(\omega^s_T)^{-1}\boldsymbol{u}\boldsymbol{v}^T(\omega^s_T)^{-1}}{1+\boldsymbol{v}^T(\omega^s_T)^{-1}\boldsymbol{u}}\right)_{ll'} \\ &= (\omega^s_T)^{-1}_{ll'} - \frac{u_0(\omega^s_T)^{-1}_{l0}\left((\omega^s_T)^{-1}_{1l'} + (\omega^s_T)^{-1}_{-1l'}\right)}{1+u_0\left((\omega^s_T)^{-1}_{10} + (\omega^s_T)^{-1}_{-10}\right)},\end{aligned} \tag{3.4}$$

for the components of the inverse matrix.

The deviation of the $(0,0)$-entry of the numerical inverse of the tagged translational frequency matrix in comparison to the analytic formula for different wave numbers and cutoffs is illustrated in Figure (3.1). Similarly, the top of Figure (3.2) shows the deviation for the $(1,1)$-entry. These figures reveal that a clear deviation can be found for large swim velocities and that inverting a sufficiently large matrix is adequate to obtain a satisfactory result. The $(0,0)$- and $(1,1)$-entries for the translational inverse frequency matrix are shown in the bottom of Figure (3.2) and in Figure (3.3), respectively. First, it can be observed that the matrices have oscillating values with respect to changing wave numbers. This is different from what was observed for the tagged matrix. Additionally, the $(0,0)$- and $(1,1)$-entry differ even more clearly from one another, which is distinct from the tagged case, too. Strikingly, the inverse matrix shows perfect agreement between the analytic solution and the numerical solution for all cutoffs for a very small wave number, in the case of the $(0,0)$-entry. However, for larger swim speeds, the deviation becomes stronger.

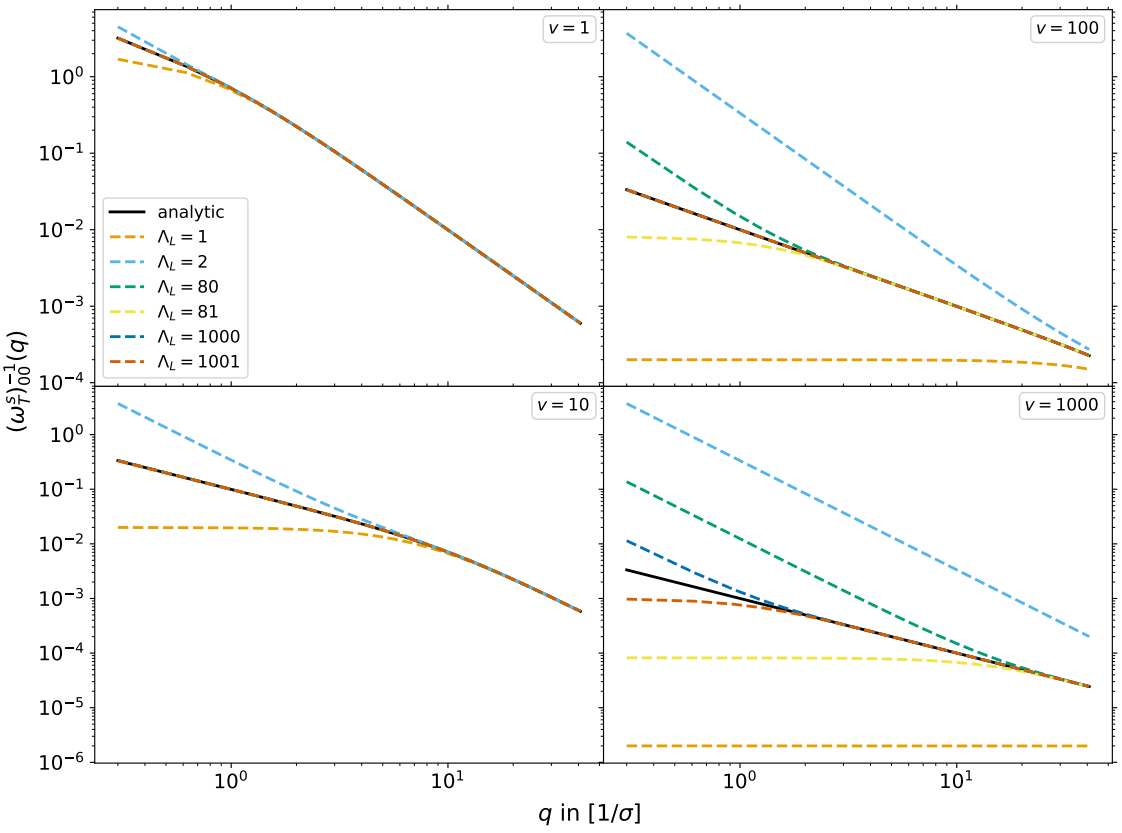

Figure 3.1: Comparison between analytic solution and numerical approximated inverse tagged translational frequency matrix for the $(0,0)$-entry of the matrix.

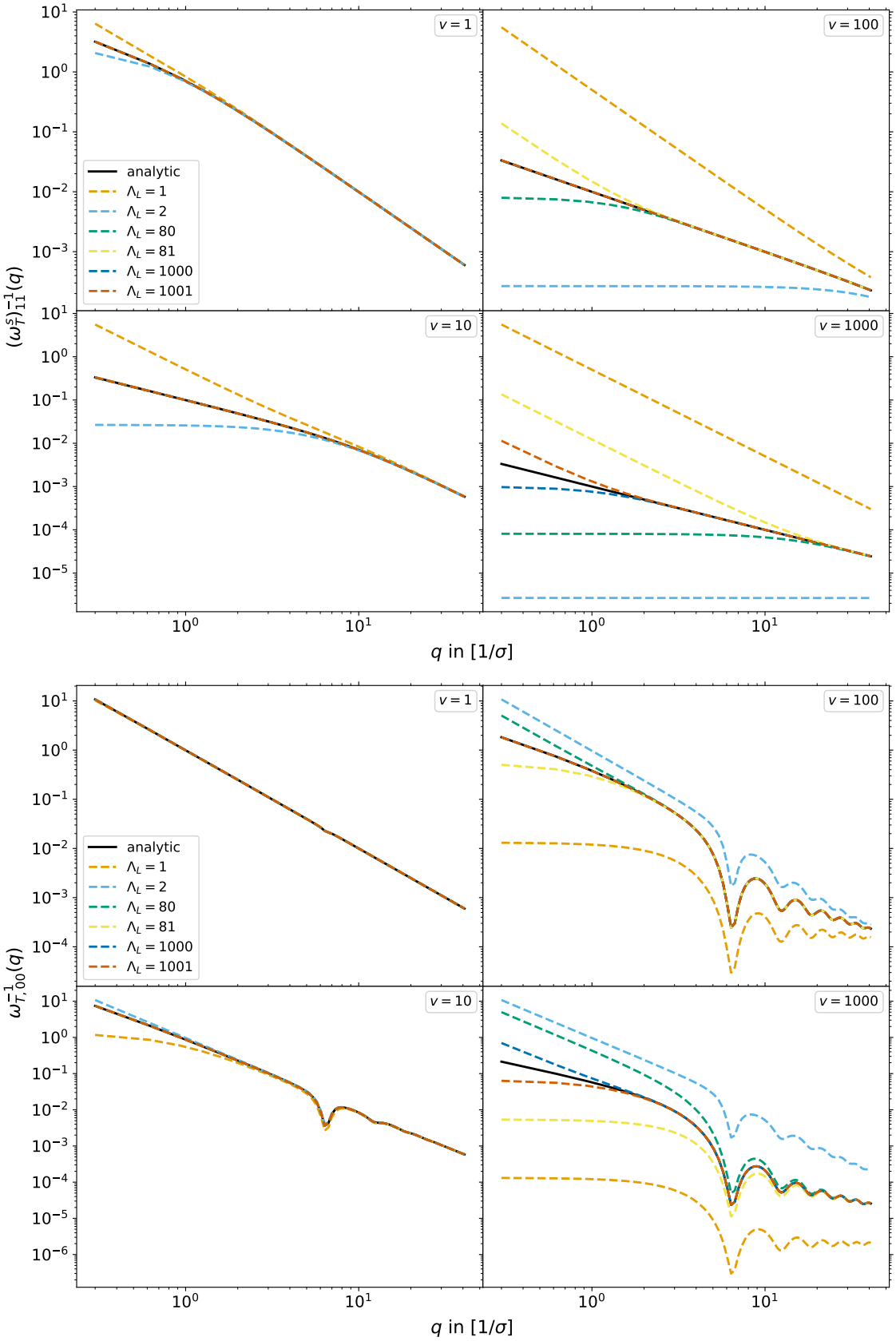

Figure 3.2: Comparison between analytic solution and numerical approximated inverse frequency matrix for the $(1,1)$-entry of the tagged frequency matrix (top) and the $(0,0)$-entry of the frequency matrix (bottom).

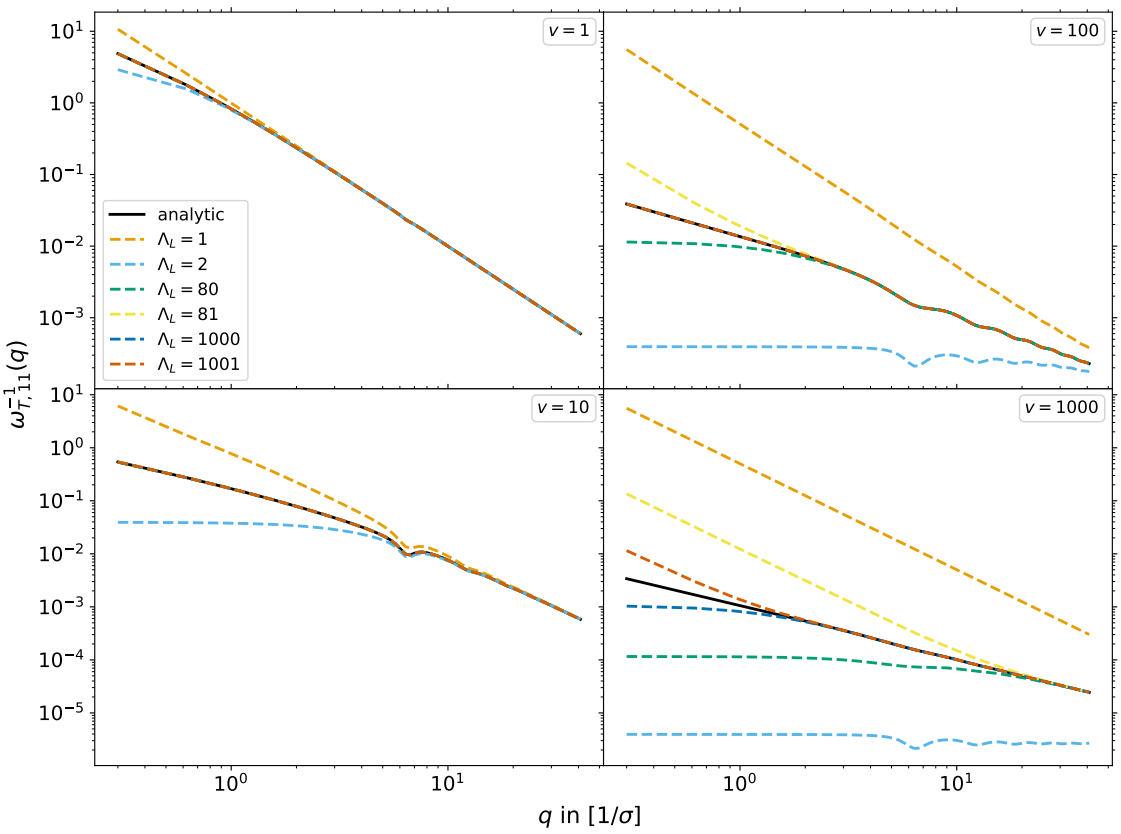

Figure 3.3: Comparison between analytic solution and numerical approximated inverse translational frequency matrix for the $(1,1)$-entry of the matrix.

Furthermore, as the focal point of this investigation resides within the domain of wave numbers at the small scale of $q < 1$, juxtaposed with swim velocities up to $v = 10$, the analytical expression proves to be of paramount utility. Indeed, this specific parameter space necessitates the inversion of frequency matrices subject to a cutoff at $\Lambda_L = 80$. Notably, should the parameter of interest extend to a potential swim velocity of $v = 100$, an exploration deemed meritorious for an inquiry into effective swim velocity, the application of elevated cutoffs, such as $\Lambda_L = 1000$, becomes imperative to yield a robust approximation. This analytic inversion obviates the requirement for any further numerical matrix inversions, affording a notable advantage. Moreover, this study demonstrated that previous studies that accounted for potential complications by inverting large matrices of appropriate size made no numerical errors by using a numerical inversion of the translational frequency matrix for active Brownian particles.

3.2 Alignment of the Wave Vector in x-Direction

The previous section demonstrated the inversion of the frequency matrix with $\boldsymbol{q}$ transformed in x-direction. The advantage of this transformation is its dependence on the absolute value of the wave vector $\boldsymbol{q}$ rather than its vectorial dependence. Additionally, the frequency matrix for different wave vector alignments can be obtained by simply multiplying the corresponding phase term. Now, the ISF, SISF, and whole MCT-equation (2.58) need to be transformed to create a consistent scheme suitable for numerical implementation. This discussion will be limited to the transformation of quantities in the x-direction.

3.2.1 The Transformed MCT-Equation

To obtain the MCT-equation transformed in the x-direction, bipolar coordinates [68] will be introduced, and it is utilized that $\boldsymbol{q} = \boldsymbol{k} + \boldsymbol{p}$, as illustrated in Figure (2.6). The corresponding Jacobian can be calculated and is given by

$$J(k,p) = \frac{2pk}{\sqrt{4q^2k^2 - (q^2+k^2-p^2)^2}}. \tag{3.5}$$

The left vertex is defined as

$$\mathcal{V}^L_{ll_1l_2}(q,k,p) = \mathcal{V}_{ll_1l_2}(q,k,p) + \delta\mathcal{V}_{ll_1l_2}(q,k,p), \tag{3.6}$$

with

$$\mathcal{V}_{ll_1l_2}(q,k,p) = \frac{D_t\varrho}{2}\delta_{l,l_1+l_2}\Big[(q^2+k^2-p^2)c(k)\delta_{l_10} + (q^2+p^2-k^2)c(p)\delta_{l_20}\Big], \tag{3.7}$$

and

$$\begin{aligned}\delta\mathcal{V}_{ll_1l_2}(q,k,p) = \frac{\mathrm{i}\,v}{2}\delta_{|l_1+l_2-l|,1}\Phi_{ll}(q)\\ \times\Big[ke^{\mathrm{i}(l_1+l_2-l)\theta_k}\Phi_{l-l_2,l-l_2}(k)\Phi^{-1}_{l_1l_1}(k) + pe^{\mathrm{i}(l_1+l_2-l)\theta_p}\Phi_{l-l_1,l-l_1}(p)\Phi^{-1}_{l_2l_2}(p) - q\Big].\end{aligned} \tag{3.8}$$

The right vertex reads

$$\mathcal{V}^R_{l'l_3l_4}(q,k,p) = \frac{D_t}{2}\delta_{l',l_3+l_4}\Big[(q^2+k^2-p^2)c(k)\delta_{l_30} + (q^2+p^2-k^2)c(p)\delta_{l_40}\Big], \tag{3.9}$$

Thereby, one calculates the angles by which $\boldsymbol{k}$ and $\boldsymbol{p}$ were rotated, in an anti-clockwise manner from the x-axis, by the use of the law of cosines, that yields

$$\begin{aligned}\theta_k &= \arccos\left(\frac{q^2+k^2-p^2}{2qk}\right),\\ \theta_p &= 2\pi - \arccos\left(\frac{q^2+p^2-k^2}{2qp}\right).\end{aligned} \tag{3.10}$$

It is worth noting that the equilibrium part of the left vertex and the right vertex itself only differ in the missing factor of ϱ in the right vertex. Despite this similarity, it is beneficial to define them separately. When implementing these formulas numerically, it may be advantageous to absorb the phase terms in the vertices and create a lookup table to speed up computation time. These equations are the x-direction transformed versions of those describing an active Brownian particle, shown in detail in Reference [55]. The incorporation of the circle swimmer frequency into the theory does not alter the structure of the MCT-equation, as it does not appear as a separate term. The rotational frequency ν only appears in the exponential function in the memory kernel and enters through the rotational part of the frequency matrix. The transformed MCT-equation reads

$$\partial_t\Phi(q,t) = -\omega(q)\Phi^{-1}(q)\Phi(q,t) - \int_0^t dt' m(q,t-t')\Big[\partial_{t'}\Phi(q,t') + \omega_R(q)\Phi^{-1}(q)\Phi(q,t')\Big], \tag{3.11}$$

and entails the transformed memory kernel $m(q,t) = M(q,t)\omega_T^{-1}(q)$ that makes use of all previous steps and entails the friction kernel, that is given by

$$\begin{aligned}M_{ll'}(q,t) \approx \int_0^\infty dk \int_{|q-k|}^{q+k}\frac{dp}{(2\pi)^2}\times\Big[\sum_{l_1l_2l_3l_4} J(k,p)\mathcal{V}^L_{ll_1l_2}(q,k,p)\\ \times\Phi_{l_1l_3}(k,t)e^{-i(l_1-l_3)\theta_k}\Phi_{l_2l_4}(p,t)e^{-i(l_2-l_4)\theta_p}\mathcal{V}^R_{l'l_3l_4}(q,k,p)\Big].\end{aligned} \tag{3.12}$$

3.2.2 The Transformed MCT-Equation of Tagged Particles

Moving on to the self-intermediate scattering function for CABP, it is worth noting that a tagged particle is considered a single particle deviating from the particles in the bath with respect to its model parameters. The set of parameters describing such a particle is $\{D_t^s, D_r^s, v^s, \nu^s\}$. The SISF describes the dynamics of the tracer particle in the bath, and the MCT-equation has the same form as above, with the simplification that the static correlation function is the identity [23]. The tagged frequency matrix can also be split into translational and rotational parts

$$\begin{aligned} \omega^s_{T,ll'}(q) &= \delta_{ll'} D_t^s q^2 - \frac{\mathrm{i}\, q v^s}{2}\delta_{|l-l'|,1}, \\ \omega^s_{R,ll'} &= \delta_{ll'}(D_r^s l^2 - \mathrm{i}\, l\nu^s). \end{aligned} \tag{3.13}$$

The tracer memory kernel can be written as $m^s(q,t) = M^s(q,t)(\omega_T^s)^{-1}(q)$ with the friction kernel

$$\begin{aligned} M^s_{ll'}(q,t) \approx 2\varrho \int_0^\infty dk \int_{|q-k|}^{q+k} \frac{dp}{(2\pi)^2} \times \Bigg[\sum_{l_1 l_2} J(k,p) \mathcal{V}^s_{ll_1l_2}(q,k,p) \\ \times \Phi^s_{l_2 l'}(p,t) e^{-i(l_2-l')\theta_p} \Phi_{l_1 0}(k,t) e^{-il_1\theta_k} \Bigg]. \end{aligned} \tag{3.14}$$

The kernel for the SISF has the same Jacobian as the one mentioned earlier. In addition, it contains the bath ISF, $\Phi_{l_1 0}(k,t)$, which must be computed prior to calculating the SISF. The vertex is divided into an equilibrium and non-equilibrium part

$$\mathcal{V}^s_{ll_1l_2}(q,k,p) = \mathcal{V}^s_{\mathrm{eq},ll_1l_2}(q,k,p) + \delta\mathcal{V}^s_{ll_1l_2}(q,k,p), \tag{3.15}$$

given by

$$\begin{aligned} \mathcal{V}^s_{\mathrm{eq},ll_1l_2}(q,k,p) &= \delta_{ll_2}\delta_{l_1 0}\left[\frac{D_t^s}{2} c(k)(q^2+k^2-p^2)\right]^2, \\ \delta\mathcal{V}^s_{ll_1l_2}(q,k,p) &= \frac{\mathrm{i}\, D_t^s}{4}\delta_{|l_1+l_2-l|,1} k\, \mathrm{e}^{\mathrm{i}(l_1+l_2-l)\theta_k}\, c^2(k)(q^2+k^2-p^2)\Big(vS(k)\delta_{ll_2} - v^s\delta_{l_1 0}\Big). \end{aligned} \tag{3.16}$$

It should be noted that the direct correlation function and the static structure factor used in these equations are those of the bath. Furthermore, as stated earlier, the static correlation function for the SISF is simply the identity matrix.

3.3 The Improved Integration Method

Previously, a demonstration was provided on how to transform all equations such that the wave vector can be directed towards a specific position, with only its magnitude and corresponding angle, that enters through a phase term, being relevant in the equations. This particular form of the equation is employed in calculating quantities of interest for the scenario involving chiral active Brownian particles. However, in the following section, the focus shifts to non-chiral active Brownian particles. This choice is made due to the fact that the subsequent symmetry arguments are exclusively applicable to ABP, which serves as the foundation for a novel integration method. This new method eliminates the explicit use of bipolar coordinates and incorporates a separation between the real and imaginary components of the intermediate scattering function and all associated quantities. Through this separation, an algorithm is constructed that avoids complex numbers entirely and is capable of monitoring potential imaginary components by observing signs and specific

matrix entries of the ISF. The following analysis reveals that the ISF, along with all related quantities of interest, can be expressed as

$$\Phi_{ll'}(q,t) = \mathrm{i}^{|(l-l')\mathrm{mod}2|}\,\hat{\Phi}_{ll'}(q,t), \tag{3.17}$$

where the component $\hat{\Phi}_{ll'}(q,t)$ represents the real scalar function

$$\hat{\Phi}_{ll'}(q,t) = \mathrm{Re}(\Phi_{ll'}(q,t)) + \mathrm{Im}(\Phi_{ll'}(q,t)), \tag{3.18}$$

and the prefactor possesses a null real part when $(l-l')$ is an odd number, and a null imaginary part when $(l-l')$ is an even number.

The argument commences with the following premise: First, a reflection of the system along the x-axis is considered, denoted by the transformation

$$\{x, y, \theta\} \mapsto \{x, -y, -\theta\}. \tag{3.19}$$

Here, θ represents the angle of the system relative to a fixed reference point, as probed by the x-axis. It is expected that this transformation does not impact the system's dynamics, which can be reasoned visually. To examine this notion mathematically, the quantities involved in the intermediate scattering function are investigated. The density functions contain an inner product, of the wave vector $q\boldsymbol{e}_x$ and the positional vector $\boldsymbol{r}_i$, that remains unchanged under the transformation. However, the angular exponential term experiences a change in sign in its exponent. Conversely, the adjoint Smoluchowski operator remains invariant, owing to the presence of inner products and the squared partial derivative of the angle. If the chirality term is included, the invariance of the Smoluchowski operator is compromised due to the involvement of a first-order partial derivative with respect to the angle. This line of reasoning leads to the following equality

$$\Phi_{-l,-l'}(q\boldsymbol{e}_x,t) = \Phi_{ll'}(q\boldsymbol{e}_x,t), \tag{3.20}$$

describing the invariance of the the system under such a transformation. Moreover, it is valid to state that

$$\Phi^*_{-l,-l'}(q\boldsymbol{e}_x,t) = \Phi_{ll'}(-q\boldsymbol{e}_x,t) = \mathrm{e}^{-\,\mathrm{i}(l-l')\pi}\,\Phi_{ll'}(q\boldsymbol{e}_x,t) = (-1)^{l-l'}\,\Phi_{ll'}(q\boldsymbol{e}_x,t). \tag{3.21}$$

Combining both equations yields the desired property

$$\Phi^*_{ll'}(q\boldsymbol{e}_x,t) = (-1)^{l-l'}\Phi_{ll'}(q\boldsymbol{e}_x,t), \tag{3.22}$$

and thus the matrix entries possess either a null real part or a null imaginary part.

The frequency matrix also exhibits the desired form. The presence of the chirality term has a notable impact, as it introduces imaginary contributions on the matrix's diagonal and hence is another indicator for ruining the symmetry argument for CABP. The memory kernel, the final quantity involved in the MCT-equation, warrants investigation regarding this characteristic. This kernel incorporates the product of the friction kernel $M(q\boldsymbol{e}_x,t)$ and the inverse translational frequency matrix, the latter of which has been previously calculated. Thus, it can be verified that the inverse translational frequency matrix also conforms to the desired form. Lastly, attention must be given to all projection operators employed in constructing the MCT-equation. As these operators sum over all possible angular indices, they remain invariant under the aforementioned transformation as well.

3.3.1 The Intermediate Scattering Function

Here, the intermediate scattering function is regarded. Afterwards, the focus is shifted towards the self-intermediate scattering function. The non-discretized expression for the friction kernel of the ISF reads

$$\begin{aligned} M_{ll'}(q,t) &\approx \mathrm{i}^{|(l-l')\mathrm{mod}2|} \int_0^\infty \frac{\mathrm{d}k}{(2\pi)^2}\frac{k}{2} \sum_{l_1 l_2 l_3 l_4} \hat{\Phi}_{l_1 l_3}(k,t) \int_0^{2\pi} \mathrm{d}\theta_k \hat{\Phi}_{l_2 l_4}(p,t) \times \Big[\cdots\Big], \\ \Big[\cdots\Big] &= \mathcal{V}^R_{l' l_3 l_4}(q,k,p)\Big(s^a_\pm \mathcal{V}_{l l_1 l_2}(q,k,p) I_A + s^b_\pm \sum_{a\in\{A,B,C\}} \delta\mathcal{V}^a_{l l_1 l_2}(q,k,p) I_a\Big), \end{aligned} \tag{3.23}$$

with the phase terms

$$\begin{aligned} I_A &= \mathrm{e}^{-\mathrm{i}(l_1-l_3)\theta_k}\, \mathrm{e}^{-\mathrm{i}(l_2-l_4)\theta_p}, \\ I_B &= \mathrm{e}^{-\mathrm{i}(l_1-l_3)\theta_k}\, \mathrm{e}^{-\mathrm{i}(l_2-l_4)\theta_p}\, \mathrm{e}^{\mathrm{i}(l_1+l_2-l)\theta_k}, \\ I_C &= \mathrm{e}^{-\mathrm{i}(l_1-l_3)\theta_k}\, \mathrm{e}^{-\mathrm{i}(l_2-l_4)\theta_p}\, \mathrm{e}^{\mathrm{i}(l_1+l_2-l)\theta_p}, \end{aligned} \tag{3.24}$$

and the redefined non-equilibrium parts of the left vertex

$$\begin{aligned} \delta\mathcal{V}^A_{l l_1 l_2}(q,k,p) &= -\frac{qv}{2}\delta_{|l_1+l_2-l|,1}\Phi_{ll}(q), \\ \delta\mathcal{V}^B_{l l_1 l_2}(q,k,p) &= \frac{kv}{2}\delta_{|l_1+l_2-l|,1}\Phi_{ll}(q)\Phi_{l-l_2,l-l_2}(k)\Phi^{-1}_{l_1 l_1}(k), \\ \delta\mathcal{V}^C_{l l_1 l_2}(q,k,p) &= \frac{pv}{2}\delta_{|l_1+l_2-l|,1}\Phi_{ll}(q)\Phi_{l-l_1,l-l_1}(p)\Phi^{-1}_{l_2 l_2}(p), \end{aligned} \tag{3.25}$$

where two alternating functions

$$\begin{aligned} s^a_\pm &= (-1)^{(l_1-l_3)(l_2-l_4)}, \\ s^b_\pm &= (-1)^{(l_1-l_3)(l_2-l_4)} \times (-1)^{(l_1-l_3)+(l_2-l_4)}, \end{aligned} \tag{3.26}$$

were defined to keep track of possible minus signs, resulting from squaring imaginary units. A comprehensive demonstration of these equations can be found in the appendix (A.2), where a detailed proof is presented. The underlying principle of the proof revolves around establishing the real-valued nature of the integrals involving I_A, I_B, I_C and their corresponding prefactors. Subsequently, it is demonstrated that, due to the presence of Kronecker deltas, only those terms persist which yield the prescribed equation. Evidently, this final equation exhibits a discernible pattern of real and imaginary components, as governed by its prefactor. It is important to note that the wave number p is dependent on the angle θ_k through Equation (3.10).

Lastly, the friction kernel is provided, resulting from a more profound exploration of the angular integration, as outlined in (A.2), which relies exclusively on real-valued components except for its prefactor. It is expressed as follows

$$\begin{aligned} M_{ll'}(q,t) &\approx \mathrm{i}^{|(l-l')\mathrm{mod}2|} \int_0^\infty \frac{\mathrm{d}k\; k}{(2\pi)^2} \sum_{l_1 l_2 l_3 l_4} \hat{\Phi}_{l_1 l_3}(k,t) \sum_{a\in\{A,B,C\}} \Big[\cdots\Big], \\ \Big[\cdots\Big] &= \int_0^{\pi/2} \mathrm{d}\theta_k\; \Xi^{(1)}_a \chi_a(q,k,p,t) + \int_{\pi/2}^{\pi} \mathrm{d}\theta_k\; \Xi^{(2)}_a \chi_a(q,k,p,t). \end{aligned} \tag{3.27}$$

In this context, reference should be made to Figure (2.6), and an angle must be defined as

$$\tilde{\theta}_p = 2\pi - \theta_p = \arctan\left(\frac{k\sin(\theta_k)}{q - k\cos(\theta_k)}\right), \tag{3.28}$$

which enters the definition of the functions

$$\begin{aligned}
\Xi_A^{(1)} &= \cos\Big((l_1-l_3)\theta_k-(l_2-l_4)\tilde{\theta}_p(\theta_k)\Big),\\
\Xi_A^{(2)} &= (-1)^{(l_1-l_3)}\cos\Big((l_1-l_3)(\pi-\theta_k)+(l_2-l_4)\tilde{\theta}_p(\theta_k)\Big),\\
\Xi_B^{(1)} &= \cos\Big((l-l_2-l_3)\theta_k-(l_2-l_4)\tilde{\theta}_p(\theta_k)\Big),\\
\Xi_B^{(2)} &= (-1)^{(l-l_2-l_3)}\cos\Big((l-l_2-l_3)(\pi-\theta_k)+(l_2-l_4)\tilde{\theta}_p(\theta_k)\Big),\\
\Xi_C^{(1)} &= \cos\Big((l_1-l_3)\theta_k-(l-l_1-l_4)\tilde{\theta}_p(\theta_k)\Big),\\
\Xi_C^{(2)} &= (-1)^{(l_1-l_3)}\cos\Big((l_1-l_3)(\pi-\theta_k)+(l-l_1-l_4)\tilde{\theta}_p(\theta_k)\Big),
\end{aligned} \tag{3.29}$$

Furthermore, this friction kernel utilizes the definitions

$$\begin{aligned}
\chi_A(q,k,p,t) &= \Big(s_\pm^a\mathcal{V}_{ll_1l_2}(q,k,p)+s_\pm^b\delta\mathcal{V}^A_{ll_1l_2}(q,k,p)\Big)\hat{\Phi}_{l_2l_4}(p,t)\mathcal{V}^R_{l'l_3l_4}(q,k,p),\\
\chi_B(q,k,p,t) &= s_\pm^b\delta\mathcal{V}^B_{ll_1l_2}(q,k,p)\hat{\Phi}_{l_2l_4}(p,t)\mathcal{V}^R_{l'l_3l_4}(q,k,p),\\
\chi_C(q,k,p,t) &= s_\pm^b\delta\mathcal{V}^C_{ll_1l_2}(q,k,p)\hat{\Phi}_{l_2l_4}(p,t)\mathcal{V}^R_{l'l_3l_4}(q,k,p).
\end{aligned} \tag{3.30}$$

For the implementation of this angular integration a summation over all possible values of p is performed, encompassing all grid values within the interval $[|q-k|, q+k]$. Subsequently, the corresponding angles are calculated and utilized for the discretization of the integral. In Chapter (4), a comprehensive explanation is provided, outlining the numerical implementation and discretization of the MCT-equation. This implementation closely aligns with that described in Reference [55], deviating solely in the explicit treatment of imaginary and real components, as well as the management of minus signs throughout.

3.3.2 The Self-Intermediate Scattering Function

The discussion of the new integration scheme of the self-intermediate scattering function for tagged active Brownian particles is similar to that of the ISF. It deviates in its use of alternating functions, to keep track of the multiplication of multiple imaginary units. First, the friction kernel is given. It reads

$$\begin{aligned}
M_{ll'}(q,t) &\approx \varrho\,\mathrm{i}^{|(l-l')\mathrm{mod}2|}\int_0^\infty\frac{\mathrm{d}k\;k}{(2\pi)^2}\sum_{l_1l_2}\hat{\Phi}_{l_10}(k,t)\int_0^{2\pi}\mathrm{d}\theta_k\hat{\Phi}^s_{l_2l'}(p,t)\times\Big[\cdots\Big],\\
\Big[\cdots\Big] &= \mathcal{V}^s_{\mathrm{eq},ll_1l_2}(q,k,p)I_O+s_\pm\delta\mathcal{V}^{s,A}_{ll_1l_2}(q,k,p)I_A,
\end{aligned} \tag{3.31}$$

with the phase terms

$$\begin{aligned}
I_O &= \mathrm{e}^{-\mathrm{i}\,l_1\theta_k}\,\mathrm{e}^{-\mathrm{i}(l_2-l')\theta_p},\\
I_A &= \mathrm{e}^{-\mathrm{i}\,l_1\theta_k}\,\mathrm{e}^{-\mathrm{i}(l_2-l')\theta_p}\,\mathrm{e}^{\mathrm{i}(l_1+l_2-l)\theta_k},
\end{aligned} \tag{3.32}$$

and the redefined non-equilibrium vertex contribution

$$\delta\mathcal{V}^{s,A}_{ll_1l_2}(q,k,p) = \frac{D_t^s}{4}\delta_{|l_1+l_2-l|,1}kc^2(k)(q^2+k^2-p^2)\Big(vS(k)\delta_{ll_2}-v^s\delta_{l_10}\Big), \tag{3.33}$$

and the alternating function

$$\begin{aligned}
s_\pm &= (1-l'\mathrm{mod}2)s_\pm^a+(l'\mathrm{mod}2)s_\pm^b,\\
s_\pm^a &= (-1)^{l_1+l_2}(-1)^{l_1l_2},\\
s_\pm^b &= (-1)^{l_1+l}(-1)^{l_1l},
\end{aligned} \tag{3.34}$$

defined to keep track of possible minus signs, resulting from squaring imaginary units. Lastly, the friction kernel is provided again, resulting from the same exploration of the angular integration, as described before and as outlined in (A.2), which relies exclusively on real-valued components except for its prefactor. It is expressed as follows

$$\begin{aligned} M_{ll'}(q,t) &\approx 2\varrho\,\mathrm{i}^{|(l-l')\mathrm{mod}2|}\int_0^\infty \frac{\mathrm{d}k\;k}{(2\pi)^2}\sum_{l_1 l_2}\hat{\Phi}_{l_1 0}(k,t)\sum_{a\in\{O,A\}}\Big[\cdots\Big], \\ \Big[\cdots\Big] &= \int_0^{\pi/2}\mathrm{d}\theta_k\;\Xi_a^{(1)}(q,k,p)\hat{\Phi}^s_{l_2 l'}(p,t) + s_\pm\int_{\pi/2}^{\pi}\mathrm{d}\theta_k\;\Xi_a^{(2)}(q,k,p)\hat{\Phi}^s_{l_2 l'}(p,t). \end{aligned} \tag{3.35}$$

and makes use of the functions

$$\begin{aligned} \Xi_O^{(1)}(q,k,p) &= \mathcal{V}^s_{\mathrm{eq},ll_1l_2}(q,k,p)\cos\Big(l_1\theta_k - (l_2-l')\tilde{\theta}_p(\theta_k)\Big), \\ \Xi_O^{(2)}(q,k,p) &= (-1)^{l_1}\mathcal{V}^s_{\mathrm{eq},ll_1l_2}(q,k,p)\cos\Big(l_1(\pi-\theta_k) + (l_2-l')\tilde{\theta}_p(\theta_k)\Big), \\ \Xi_A^{(1)}(q,k,p) &= \delta\mathcal{V}^{s,A}_{ll_1l_2}(q,k,p)\cos\Big((l-l_2)\theta_k - (l_2-l')\tilde{\theta}_p(\theta_k)\Big), \\ \Xi_A^{(2)}(q,k,p) &= (-1)^{l-l_2}\delta\mathcal{V}^{s,A}_{ll_1l_2}(q,k,p)\cos\Big((l-l_2)(\pi-\theta_k) + (l_2-l')\tilde{\theta}_p(\theta_k)\Big). \end{aligned} \tag{3.36}$$

Here, $p \equiv p(\theta_k)$ is again a function

$$p(\theta_k) = \sqrt{q^2 + k^2 - 2qk\cos(\theta_k)} \tag{3.37}$$

of the angle θ_k and a numerical implementation uses such values for θ_k that correspond to certain values of the wave number grid.

4. Numerical Details

There are three major versions of MCT-code employed in this thesis. The initial version comprises code designed for passive Brownian particles. It addresses the partial integro-differential equations governing these particles' behavior, encompassing both the ISF and SISF. Furthermore, this version enables the determination of the critical packing fraction and the non-ergodicity parameter. The utility of this particular code lies in its ability to facilitate a comprehensive comparison with data obtained from the second version of the code in this thesis. The second version of the code centers on the solution of chiral active Brownian particles. When the rotational frequency, rotational diffusion constant, and swim speed all tend toward zero, a passive Brownian particle's behavior is replicated. Consequently, in this limit, the results produced by this second version of the code should align with those generated by the initial version. As this code proves to be more intricate than its predecessor, the predecessor serves a dual purpose: aiding in the debugging process and serving as a preliminary validation for the numerical methodology. The third and final version of the MCT-code incorporates symmetry features, specifically applicable to non-chiral active Brownian particles. However, its implementation remains an open problem and is not utilized in the analysis presented herein.

Subsequently, a comprehensive discussion of the numerical implementation is presented, as the discretization of the MCT-equation and its subsequent integration forms the crux of this endeavor. The approach closely mirrors the one delineated in the appendix of Reference [55]. However, the forthcoming discussion delves into a more intricate elucidation of the numerical implementation. This detail is warranted due to the limited explanations available regarding the stability boundaries of MCT-numerics, the conditions under which they remain robust, and the specific parameter regimes where an imminent numerical instability and code divergence is anticipated.

4.1 The Discretization of the MCT-equation

The ensuing section encapsulates the discretization process of the MCT-equation, as elucidated by the exposition in Reference [55]. This commences by recognizing the characteristic property of the correlation function, whereby it diminishes across several orders of magnitude, rendering it a gradually altering temporal entity. Consequently, its temporal derivatives are expected to become small as $t \to \infty$. This enables the solution of the equation to be partitioned into distinct segments, designated by the integer $b = 1, 2, \ldots, B$. Each of these temporal segments, referred to as time blocks, encapsulates time instances separated by a standardized time increment $h_b = h_1 2^{(b-1)}$. Aligning with the programming language Julia's indexing, which commences with 1 for the initial element of a sequence or array, this indexing convention is adopted. The computational framework employs $B = 45$ of such blocks, each consisting of 256 temporal values, effectively overseeing the temporal decay of the correlation function across a sufficiently extensive temporal span.

Denoting the time instances within each block as $t_i = (i-1)h_b$, a backward Euler method is operationalized within each block to resolve the underlying differential equation. In this context, the derivatives with respect to time in the MCT-equation are substituted by the expressions

$$\partial_t \Phi_i = \big[(3/2)\Phi_i - 2\Phi_{i-1} + (1/2)\Phi_{i-2}\big]/h_b. \tag{4.1}$$

This substitution is built on the assumption that the initial correlation values for each block are already known. To realize this, a "block 0" is introduced, with its entries computed by solving the MCT-equation for a free particle (2.49). The remaining values within the first block are then determined using the subsequent iterative discretization scheme, incorporating the backward Euler method. The first half of values in each ensuing block are derived through the time decimation process. The second half is obtained by the application of the backward finite differences method.

The numerical discretization process uses a reformulated version of the MCT-equation. Notably, this discretization is known to be stable [55], owing to the utilization of auxiliary functions that streamline the iterative process. By suppressing the wave number dependence, the reformulated equation assumes the form

$$\begin{aligned} \partial_t \bar{\Phi}(t) &= -\omega_T \cdot \Phi_1^{-1} \cdot \Phi(t) - \int_0^t \mathrm{d}t' m(t-t') \cdot \partial_{t'} \bar{\Phi}(t'), \\ \partial_t \Phi(t) &= \partial_t \bar{\Phi}(t) - \omega_R \cdot \Phi_1^{-1} \cdot \Phi(t). \end{aligned} \tag{4.2}$$

Here, $\bar{\Phi}(t)$ signifies the auxiliary correlation function, with $\bar{\Phi}(0) = \Phi(0) = \Phi_1$. For discretizing the convolution integral, the introduction of moments proves essential, defined as

$$d\bar{\Phi}_i = \frac{1}{h_b}\int_{t_i}^{t_{i+1}} \mathrm{d}t\ \bar{\Phi}(t) = \frac{1}{2}(\Phi_i + \Phi_{i+1}), \quad dm_i = \frac{1}{h_b}\int_{t_i}^{t_{i+1}} \mathrm{d}t\ m(t) = \frac{1}{2}(m_i + m_{i+1}). \tag{4.3}$$

This permits the expression of the integral term in the following manner

$$\begin{aligned} \int_0^t \mathrm{d}t' m(t-t') \cdot \partial_{t'} \bar{\Phi}(t') &\approx m_{i-\bar{i}} \cdot \bar{\Phi}_{\bar{i}+1} - m_i \cdot \bar{\Phi}_1 + \big[\cdots\big], \\ \big[\cdots\big] = \sum_{k=1}^{\bar{i}} [m_{i-k+1} - m_{i-k}] \cdot d\bar{\Phi}_k &+ \sum_{k=1}^{i-\bar{i}-1} dm_k \cdot [\bar{\Phi}_{i-k+1} - \bar{\Phi}_{i-k}]. \end{aligned} \tag{4.4}$$

The integral is approximately divided at the midpoint of the time interval, indicated by index $\bar{i} = \lfloor (i-1)/2 \rfloor$, and it is assumed that its integrand varies slowly for times $t \geq t_{\bar{i}}$. Leveraging this insight, the reformulated equation can be discretized as

$$\begin{aligned} \bar{\Phi}_i &= A^{-1} \cdot (m_i[\Phi_i] \cdot B - C_i), \\ \Phi_i &= A_L^{-1} \cdot \left[\frac{3}{2h_b}\bar{\Phi}_i + A_R\right], \end{aligned} \tag{4.5}$$

with the inclusion of auxiliary matrices denoted as

$$\begin{aligned} A_L &= \frac{3}{2h_b}\,\mathrm{Id} + \omega_R \cdot \Phi_1^{-1}, \\ A_R &= \frac{1}{h_b}\Big[-2(\bar{\Phi}_{i-1} - \Phi_{i-1}) + (\bar{\Phi}_{i-2} - \Phi_{i-2})/2\Big], \\ A &= \frac{3}{2h_b}\,\mathrm{Id} + \frac{3}{2h_b}\,\mathrm{Id} \cdot \omega_T \cdot \Phi_1^{-1} \cdot A_L^{-1} + dm_1, \\ B &= \bar{\Phi}_1 - d\bar{\Phi}_1. \end{aligned} \tag{4.6}$$

Additionally, the expression for the convolution sum results in

$$\begin{aligned} C_i = \frac{1}{h_b}[-2\bar{\Phi}_{i-1} + \bar{\Phi}_{i-2}/2] + \omega_T \cdot \Phi_1^{-1} \cdot A_L^{-1} \cdot A_R + m_{i-\bar{i}} \cdot \bar{\Phi}_{\bar{i}+1} - m_{i-1} \cdot d\bar{\Phi}_1 \\ - dm_1 \cdot \bar{\Phi}_{i-1} + \sum_{k=2}^{\bar{i}} [m_{i-k+1} - m_{i-k}] \cdot d\bar{\Phi}_k + \sum_{k=2}^{i-\bar{i}-1} dm_k \cdot [\bar{\Phi}_{i-k+1} - \bar{\Phi}_{i-k}]. \end{aligned} \tag{4.7}$$

The solution scheme is now comprehensive. Initially, the memory kernel is computed by employing the previous time value for the correlation function. Subsequently, the auxiliary correlation function is computed based on this memory kernel result. Utilizing the auxiliary function, the dynamic correlation function can then be recalculated. This process iterates through an iterator until a predetermined precision or a maximum iteration count is attained. Once a block concludes, a time decimation takes place. This involves obtaining the first half of the next block for the correlation function and memory kernel through the mapping $\Phi_{2i-1} \mapsto \Phi_i, m_{2i-1} \mapsto m_i$, utilizing the values of the previous block. The moments can be discretized as $(d\Phi_{2i-1} + d\Phi_{2i})/2 \mapsto d\Phi_i, (dm_{2i-1} + dm_{2i})/2 \mapsto dm_i$. When a moment does not exist for a specific index, the moments should be replaced by their corresponding expressions that depend on the correlation function or memory kernel themselves.

It is important to make explicit reference to the fact that the numerical discretization herein satisfies the bifurcation equation denoted as $f = m(1 - f)$, with $m \equiv m[f]$, within the passive long term limit, as t tends towards infinity, and h_b grows infinitely large. A more profound description of this assertion is found in the work of Götze [54]. The manifestation of this connection becomes evident through the exposition that follows, wherein this long time limit is under scrutiny. Initially, it can be observed that in this limit, the parameter denoted as A_R converges to zero. Furthermore A_L approaches $3/(2h_b)\,\mathrm{Id}$. Consequently, the lower equation encapsulated within Equation (4.5) conveys that the distinction between the correlation function and its auxiliary counterpart vanishes, such that $\Phi = \bar{\Phi}$. As for the variable designated as B, it holds $B \to 1 - df$, and in the case of the parameter A, it satisfies the condition $A \to 1 + dm$. The expression C entails a degree of intricacy. Upon acknowledging that the deviations among correlation values of the memory kernel recede in this limit, it becomes apparent that C approaches the expression $mf - m\ df - f dm$. Substituting these outcomes into the upper equation encompassed within Equation (4.5) culminates in the emergence of the bifurcation equation. This substantiates that, instead of resorting to an implicit Euler method, the finite difference approach can be utilized for the discretization of the MCT-equation.

A final crucial point to note is the utilization of a fifth-order open extended Newton-Cotes formula [69] for calculating the innermost wave number integral of the memory kernel. This formula has been employed in earlier implementations [23–25, 55] and has demonstrated satisfactory convergence characteristics in handling the singular Jacobian of the integrand. It is expressed as

$$\int_{q_1}^{q_M} \mathrm{d}q\ f(q) = h_q \left[\frac{55}{24} f_2 - \frac{1}{6} f_3 + \frac{11}{8} f_4 + f_5 + \ldots + f_{M-4} + \frac{11}{8} f_{M-3} - \frac{1}{6} f_{M-2} + \frac{55}{24} f_{M-1} \right], \tag{4.8}$$

where h_q represents the time interval between two wave numbers and the dots denote terms with additional unit coefficients.

4.2 The Numerical Implementation

The previous segment described the discretization of the MCT-equation and entailed an introduction of auxiliary correlation functions and moments to ensure the stability of the code. The current section shifts its emphasis towards the numerical realization of these equations. The Julia programming code is organized into a modular framework, with each module representing a discrete translation unit saved in an individual file. Of particular significance are two files: "Main.jl" and "ActiveParameters.jl."

The initial of these encompasses the program's entry point. Separate files are dedicated to the computation of the ISF and SISF, the latter of which takes the text data from a previously computed ISF as input. The "ActiveParameters.jl" module establishes the initial values, thereby governing the program's logical structure. Initially, command-line arguments and other constants that require definition are exported to be accessible in the main file and other modules. These constants are saved as numerical entities, a trait adhering to the principles of type stability in the Julia programming language. Although potential alterations to these numerical values remain feasible as long as the type is not changed, such changes are, and should be, minimized. Notably, Julia is not an object-oriented programming language, thus devoid of classes and objects. Nevertheless, the features inherent in these concepts can be emulated through structures and modules. Throughout the program's execution, the values for the memory kernel and correlation function undergo multiple modifications. Since numerous functions operate on these functions, a prudent approach is to store them on the heap and employ mutating functions whenever possible, both to economize memory utilization and to expedite subsequent heap allocations. In Julia, this objective is accomplished through the formulation of structures. This program introduces the structures "struct MomentSolutions", "struct FrequencyMatrix", "struct LookUp", and "struct TaggedLookUp", with the latter two being subtypes of the abstract type "LookUpTable". For optimal performance, these structures are defined as parametric, indicating that they should be characterized by the fundamental types of their constituent fields. Each structure is endowed with a constructor, ensuring proper initialization when invoked.

The "struct MomentSolutions" structure encompasses essential components, including the grid's wave numbers, the direct correlation function, the inverse static correlation function, along with arrays representing various correlation functions and memory kernels. These arrays are initialized with zero values. An important feature of the Julia programming language pertains to array initialization. While it is feasible to create uninitialized arrays, these can lead to random memory artifacts, if not handled carefully. As such, it is considered good practice to initialize such arrays with zero values. Additionally, it's crucial to address that Julia adopts a column-major order, similar to Fortran. Consequently, arrays must be defined accordingly to prevent memory jumps during iteration. The structure linked to the frequency matrix includes arrays associated with this matrix, while the look-up tables structure encompasses tables pertinent to the wave number integration domain of the innermost integral of the memory kernel, as well as the angles θ_k and θ_p between corresponding wave vectors and the system's x-axis. These tables also pertain to the vertices. This approach yields substantial computational time savings, as it circumvents the need for frequently time-consuming function calls. Naturally, this optimization amplifies memory usage; however, the overall program's memory consumption remains capped at 50 GB, assuming an angular index cutoff of $\Lambda_L = 1$, i.e., $l \in \{-1, 0, 1\}$. It's important to note that larger cutoffs can swiftly escalate memory requirements, thereby establishing a primary limitation within the program.

Two distinct "Main.jl" files exist: "MainActive.jl" and "MainTagged.jl". The former computes the ISF, while the latter focuses on the SISF. In the initial stages of "MainActive.jl", the necessary packages are invoked. Following this, the "ActiveParameters.jl" file is included, and its module is loaded using the command "using .ActiveParameters," adhering to the naming of the module. This sequence is designed to ensure that the other modules are loaded only after the parameter file has been incorporated into the main file, given that these modules draw their parameters from this translation unit. Upon this foundation, multiple functions are constructed to build the frequency matrix, functioning as mutating operations on the corresponding structures delineated in the "ActiveParameters.jl" file. It is worth noting that every function is designed to utilize the *@inbounds* macro. Julia's built-in just-in-time compilation and execution encompass boundary checking, which this macro allows to bypass, thereby conserving critical computational time. Following debugging, benchmarking, and thorough testing, the inclusion of this macro is recommended. The subsequent function construction pertains to the generation of the static correlation function. This function thereby generates the initial values for solving the correlation function when invoked. Subsequently, a function is devised to construct the small time values. These values are determined by analytically solving the MCT-equation for a free particle, specifically the equation that assumes the memory kernel to be negligible.

An additional function incorporates the resolution of the differential equation within a single time block. Both of these functions, in turn, invoke the function responsible for constructing the memory kernel. A noteworthy detail is that the memory kernel is contingent on the wave number q and can be computed distinctly for various wave numbers. Given that the numerical solution uses on a grid of 128 wave numbers, parallelizing the computation of these values becomes advantageous. Various methods for parallelization are available. Firstly, SIMD (Single Instruction, Multiple Data) optimization comes into play. This optimization, automated by the LLVM compiler tailored to the processor architecture, is highly efficient. For instance, an AVX512 processor can execute 8×64 BIT floating-point operations simultaneously, distributing operations across loops. Thus, it's recommended to use loop constructs as frequently as possible within the programming language. Next, MPI (Message Passing Interface) is a parallelization approach, but it's not adopted here due to the relatively straightforward parallelization required. Distributed programming isn't employed either, primarily due to the time-consuming data transfers between different processes and the substantial overhead involved in initiating such processes. Instead, the approach taken is akin to the "#pragma omp parallel for" used in OpenMP for C++. For this type of task, threading within Julia is recommended. It facilitates the parallelization of memory kernel calculations for diverse wave numbers without incurring substantial overhead.

Ultimately, the program's point of entry is represented by the primary function. In its initial steps, it invokes the constructors belonging to the structures outlined in the parameter model. Following this, a function from an external module, responsible for computing the wave number grid, is called into action. In this process, both a low and high wave number cutoff are determined. This choice introduces an additional numerical constraint. In principle, an infinitely expansive wave number grid would be ideal, yet in practical terms, such a limitless consideration remains infeasible. The subsequent chapter, among other things, investigates the impact of the low wave number cutoff. Notably, a small cutoff below $q = 2.5$ leads to potential terms that converge near the divergent segment of the integrand within the memory kernel integral. It's worth mentioning that the associated look-up table for this integration is engaged. Here, the objective is to identify the initial and concluding

wave numbers, denoted as p, encompassed within the range $[|q-k|, q+k]$, and then store these values. This expedited retrieval of values enhances the computation efficiency of the memory kernel. Subsequently, the tables for angles and the static correlation matrix are generated, since they are pivotal in computing the vertices. These vertices are constructed subsequently. The generation of frequency matrices follows, accompanied by the invocation of the initial value function and the solution of the differential equation for a given block. This latter operation iterates for all blocks, with the resultant outcomes being saved in the form of text data file.

The final component involves a module responsible for the computation of the memory kernel and the iterative process. As elucidated earlier, the iteration function employs prior correlation function values, computes the memory kernel, then the auxiliary correlation function, and subsequently, the new correlation function. This sequence persists until either a critical threshold of a maximum of 8000 iterations is reached or a termination criterion is satisfied. The first termination criterion regards the $(-1,-1)$-elements of both the previous and updated correlation function components aligning with a relative and absolute tolerance of 10^{-9}. These components are stored as vectors, $\boldsymbol{u}$ an $\boldsymbol{v}$, where each element corresponding to a distinct wave number. The termination criterion evaluates to true if the inequality

$$|\boldsymbol{u}-\boldsymbol{v}| \leq \max(\mathrm{atol}, \mathrm{rtol} \times \max(|\boldsymbol{u}|, |\boldsymbol{v}|)) \tag{4.9}$$

holds, where the norm reflects the standard Euclidean norm in such a vector space. This approach obviates the need for inspecting each individual correlation function component separately. Indeed, the unmet criterion for one specific component implies the likelihood of similar non-conformity among the other components. Upon criterion fulfillment, an additional loop iterates through every individual component of either the ISF or SISF. Only when all components adhere to the stipulated condition does the overarching termination criterion become satisfied, thereby concluding the calculation of the next correlation function value in time.

4.3 The Improved Integration Method

The enhanced method of integration employed the multiplication behavior of matrices with specific structural attributes, as expounded upon in (A.3), to circumvent the necessity for complex numbers. This, in turn, resulted in a notable acceleration of computational processes. In both previous investigations [23–25, 55] and the current work, it becomes apparent that when approaching the limit of ABP, the computational routine aggregates infinitesimal imaginary components that eventually manifest as noteworthy contributions. A further numerical instability manifests when the swim velocity surpasses a specific threshold, or when the rotational parameters, particularly within the context of CABP, attain excessive values. Moreover, the advent of instabilities is conceivable in cases where the system's ergodicity is compromised, leading to minute imaginary constituents that trigger an oscillatory trend, superimposing the plateau observable in the ISF or SISF. A first idea to solve this issue involves verifying the nullity of select imaginary components. Those found non-null are then subjected to a mathematical operation aimed at their nullification. Regrettably, this procedural course has proven to be overly time-intensive. Drawing from the tenets of symmetry, it becomes apparent that an alternative analytical formulation of the memory kernel is plausible for ABP, one that encompasses these attributes and thus circumvents the aforementioned challenges. The previous chapter has exhibited a derivation of this novel memory kernel. Armed with this formulation, the potential for devising an improved approach emerges, one poised to address the MCT-equation for

elevated swim speeds. This, in turn, could facilitates a more intricate exploration of the effective swim velocity and the resultant motility-induced phase separation.

The implementation mirrors that of CABP, albeit distinguished by the inclusion of the aforenoted alternating sign function within matrix multiplications. In this instantiation, the code abstains from deploying any lookup table to ascertain the vertices. Instead, it engenders them as functional entities. Additionally, the functions denominated as χ and Ξ emerge, constituting integral components of the analytical formulations underpinning this alternative memory kernel. Although the formulations have been actualized, the fidelity of their implementation remains an ongoing enigma. Discrepancies in the numerical values of the memory kernel, when juxtaposed against those generated by alternative code, indicate a potential error. Another issue pertains to the prevailing runtime predicament. The strategy of crafting vertices and engendering the χ and Ξ functions sans recourse to a lookup table ushers forth billions of function invocations. Consequently, the attainment of a precise and accurate implementation remains an open problem.

4.4 The Nonuniform Integration Method

In Reference [70], a novel integration technique for PBP is expounded. This integration method introduces a nonuniform wave number grid comprising N discrete points, as opposed to the conventionally employed uniform discretization. This confers a distinct advantage. By selecting a grid that allocates more points proximate to the first and second peaks of the static structure factor, and fewer points for larger wave numbers, a grid of approximately $N = 50$ points proves sufficient for achieving numerical stability, as outlined in Reference [70]. In contrast, the uniform integration scheme necessitates approximately 100 grid points.

The memory kernel is a wave number-dependent entity that entails a double integration over the same wave number grid. Consequently, there exists a cubic dependence on the number of grid points, and a reduction in the number of grid points leads to an approximate reduction of summation steps of one order of magnitude. This, in turn, translates to computational time in a linear yet not straightforward manner. As elucidated below, this nonuniform integration method poses greater numerical intricacy. Nevertheless, it allows for a potential halving of computational time [70]. The method's advantage primarily resides in diminished memory consumption, rather than a substantial enhancement in computational speed. In cases where memory usage is a critical consideration, adapting a nonuniform integration scheme proves advantageous.

For ABP and angular cutoffs exceeding $\Lambda_L > 1$, such an adaptation would represent a highly beneficial improvement. Regrettably, the method presented cannot be readily applied to such an extension of passive Brownian particles. Employing a nonuniform wave number grid necessitates a semi-analytical approach for the innermost integral of the memory kernel, while the outer integral is discretized as a trapezoidal one. The memory kernel reads

$$M_i = \frac{\varrho}{2} \sum_{j=0}^{N-2} (q_{j+1}\Phi_{j+1}A_{i,j+1} + q_j\Phi_j A_{i,j})(q_{j+1} - q_j)/2, \tag{4.10}$$

with $M_i = M(q_i, t)$ and $\Phi_i = \Phi(q_i, t)$. The inner integral is given by

$$A_{i,j} = \int_{|q_i - q_j|}^{q_i + q_j} \mathrm{d}p \; p \; \Phi(p,t) \frac{\Big[(q_i^2 + q_j^2 - p^2)c_j + (q_i^2 + p^2 - q_j^2)c(p)\Big]^2}{\sqrt{4q_i^2 q_j^2 - (q_i^2 + q_j^2 - p^2)^2}}. \tag{4.11}$$

The crucial point is the substitution $p \mapsto x = (q_i^2 + q_j^2 - p^2)/(2q_iq_j)$. Thereby, one must keep in mind that $\Phi(p,t)$ and the direct correlation function $c(p)$ are also affected by the substitution. The integral after the substitution reads

$$A_{i,j} = 2q_i^2 q_j^2 \int_{-1}^{1} \mathrm{d}x \; \Phi(p,t) \frac{\left[(c_j - c(p))x + \frac{q_i}{q_j} c(p)\right]^2}{\sqrt{1-x^2}}. \tag{4.12}$$

The next step includes splitting the interval $[-1,1]$ in $l_2 - l_1 + 2$ subintervals where $l_2 - l_1 + 1$ is the number of grid points contained in the interval $[|q_i - q_j|, q_i + q_j]$ such that the integral can be split up into a sum of integrals over these subintervals

$$A_{i,j} = 2q_i^2 q_j^2 \sum_{l=l_1-1}^{l_2} \int_{x_{l+1}}^{x_l} \mathrm{d}x \; \Phi(p,t) \frac{\left[(c_j - c(p))x + \frac{q_i}{q_j} c(p)\right]^2}{\sqrt{1-x^2}}. \tag{4.13}$$

Here, $x_{l_1-1} = -1$ corresponds to $p = q_i + q_j$ and $x_{l_2+1} = 1$ corresponds to $p = |q_i - q_j|$ and $x_l = (q_i^2 + q_j^2 - p_l^2)/(2qk)$ with the index $l_1, \ldots, l_2$ labeling the grid points q_l for which the inequality $|q_i - q_j < q_l < q_i + q_j|$ holds. The last step involves to rewrite the integral term like

$$A_{i,j} = 2q_i^2 q_j^2 \sum_{l=l_1-1}^{l_2} \sum_{\alpha=0}^{2} \int_{x_{l+1}}^{x_l} \mathrm{d}x \; g_\alpha(x, q_i, q_j) \frac{x^\alpha}{\sqrt{1-x^2}}, \tag{4.14}$$

with $g_0(x, q_i, q_j) = [q_i c(p)/q_i]^2 \Phi(p,t)$ and $g_1(x, q_i, q_j) = 2[c_j - c(p)][q_i c(p)/q_i]\Phi(p,t)$ and $g_1(x, q_i, q_j) = 2[c_j - c(p)]^2 \Phi(p,t)$. This assumes that the functions g_α are approximated as linear functions

$$g_\alpha(x) = g_\alpha(x_l) + \frac{g_\alpha(x_{l+1}) - g_\alpha(x_l)}{x_{l+1} - x_l}(x - x_l) \tag{4.15}$$

in the integration domain.

An analogous equation can be derived for ABP or CABP. However, an issue arises with this derivation, stemming from the substitution process itself and the subsequent linear approximation of the functions denoted as g_α. This issue is attributable to the intricate nature of the nonequilibrium component within the left vertex. It encompasses multiple phase factors contingent upon the angles θ_k and θ_p, which, in turn, rely on all three wave numbers q, k, p. The additional phase factors arising from the transformation of the two ISFs featured in the memory kernel along the x-direction ruins the assumption of linearity in the functions g_α. Moreover, these even more intricate equations yield a further escalation in numerical computational time. Consequently, resorting to this method becomes necessary solely when stringent memory constraints are paramount, as it is not a straightforward endeavor.

5. Chiral Active Brownian Particles

The in x-direction transformed MCT-equation and its associated quantities are applicable for investigating chiral active Brownian motion. However, additional symmetries, such as the invariance of the ISF under reflections of the system at the x-axis, are not present in this case. This is due to the circle swimmer contribution breaking the symmetry, resulting in the rotational part of the adjoint Smoluchowski operator being skew-adjoint, like described in Chapter (3). From a physical standpoint, this is expected since a pseudo (axial) vector, which is how the rotational chirality term could be considered, transforms differently from a polar vector. As a result, the modified numerical method is not utilized in this chapter, and the standard uniform integration method that was previously described is employed.

5.1 The MSD of a Free Chiral Active Brownian Particle

Moreover, it is essential to provide a more in-depth explanation regarding the influence of considering correlations over a certain distance, which corresponds to $l \sim 1/q$. To accomplish this, the mean-squared displacement of a free chiral active Brownian particle is analyzed [3]. The mean-squared displacement is given by the equation

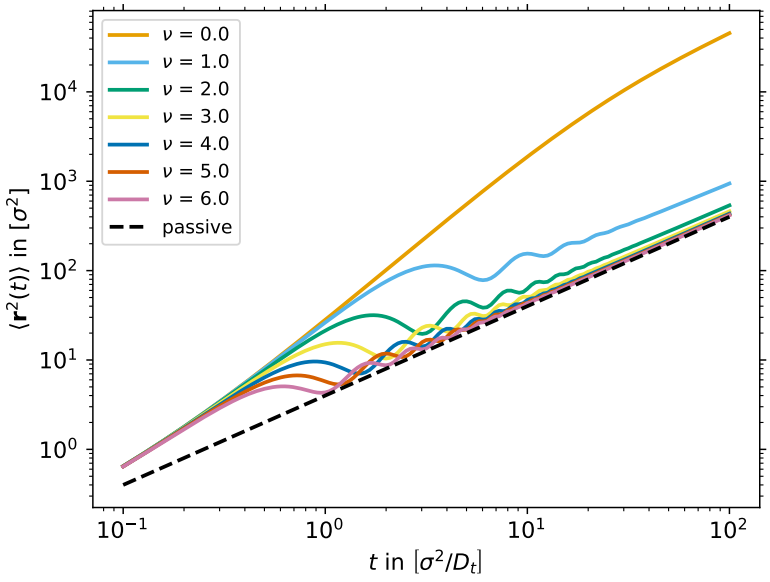

Figure 5.1: Analytic mean-squared displacement for different rotational frequencies $\nu = \nu^s$. A vanishing rotational frequency corresponds to an active Brownian particle. The mean-squared displacement for a passive Brownian particle is indicated by the dashed line. The set of system parameters is given by $\{D_t = D_t^s = 1.0, D_r = D_r^s = 0.1, v = v^s = 5.0\}$.

$$\langle \boldsymbol{r}^2(t)\rangle = 4D_t t\Big[1 + P_\nu\Big(1 + \frac{D_r^2-\nu^2}{D_r^2+\nu^2}\frac{e^{-D_r t}\cos(\nu t)-1}{D_r t} - \frac{2\nu}{(D_r^2+\nu^2)t}e^{-D_r t}\sin(\nu t)\Big)\Big], \quad (5.1)$$

where the Péclet number is

$$P_\nu = \frac{v^2 D_r}{2D_t(D_r^2+\nu^2)}. \quad (5.2)$$

Figure (5.1) presents the analytic formula for the mean-squared displacement of a free particle, exhibiting four distinct regimes. First, for very small times $t \ll 4D_t/v^2 = t_b$, a purely diffusive dynamics can be observed. As time progresses, this behavior changes into ballistic motion. For even longer times one can define an effective diffusion constant $D_L = D_t(1+P_\nu)$, and the dynamics can once again be described as diffusive for times that satisfy $v^2t^2 = 4D_L t$. These times are given by $t \gg t_b + 2D_r/(D_r^2+\nu^2) = t_p$, and eventually are superimposed with oscillations, which are characterized by the rotational frequency ν, thereby reflecting the particle's rotational behavior. This feature distinguishes chiral active Brownian particles from active Brownian particles. The oscillations are anticipated in a region $t_p < t < t_b + 2/D_r$. It is important to highlight that the mean-squared displacement for a chiral active Brownian particle is generally smaller than that of an active Brownian particle. This observation is logical since the rotational frequency has a similar impact on particle movement as the rotational diffusion constant. The frequency acts as a hindrance to the enhanced movement ability induced by swim velocity, and this effect occurs in a strictly monotonic manner. At larger rotational frequencies, encompassing timescales associated with ballistic motion and increased diffusion, the mean-squared displacement of a CABP coincides with that of a passive particle, whereas the ABP exhibits significant deviations, particularly at longer times. This implies that high rotational frequencies completely diminish the long-term active behavior of a chiral active Brownian particles, effectively rendering the system describable by its passive counterpart during such timescales. It should be noted that these observations pertain to the analysis of a single free particle, and the collective dynamics of a system may exhibit slight differences.

With the persistence time t_p a persistence length $l_p = \sqrt{\langle \boldsymbol{r}^2(t_p)\rangle/4}$ can be defined. Although this definition does not straightforwardly generalize to the interacting collective system, it nonetheless provides a useful approximation for understanding the distances at which the oscillatory effect of the rotational frequency can be observed. For the given set of system parameters of $\{D_t = 1.0, v = 5.0, D_r = 0.1, \nu = 5.0\}$, the persistence length is $l_p = 0.5774$. This suggests that one should anticipate oscillations in the self-intermediate scattering function for wave vectors approximately $q < 1/l_p = 1.73$. This consideration is crucial to keep in mind while progressing.

5.2 The Dynamical Correlation Functions

The present investigation commences with an examination of the ISF and SISF for chiral active Brownian particles. First, the results derived from the numerical solution of the MCT-equation are presented. Subsequently, a comparative analysis with the simulation results is made. All numerical results are obtained for a diffusion constant and a particle diameter that are both set to one: $D_t = \sigma = 1.0$. The underlying grid of wave numbers has a low-q cutoff of $q_1 = 0.3/\sigma$ and a high-q cutoff of $q_M = 40.0/\sigma$, thereby using a regular gird of $M = 128$ values.

5.2.1 Comparison to Passive Brownian Particles

First and foremost, Figure (5.2) presents the static structure factor computed for $M = 128$ wave numbers, precisely matching the quantity of wave numbers utilized in the numerical solution of the MCT equation. Hence, the figure depicts the exact static structure factor used in the numerical calculations, serving as the initial values for the ISF and the differential equation. It can be seen that the resolution is sufficient to generate glassy dynamics. This function was determined by employing the aforementioned expression for the direct correlation function, which was calculated via the DFT method outlined in Reference [60]. The reference demonstrates a close agreement with the location of the maxima, but a notable variance is observed concerning the height of these maxima. Specifically, the first maximum exhibits an excessive height, while the second one appears too low. This discrepancy becomes more pronounced as the densities increase, while the effect is comparatively milder for lower densities. Consequently, it is imperative to bear this particular characteristic in mind while progressing further.

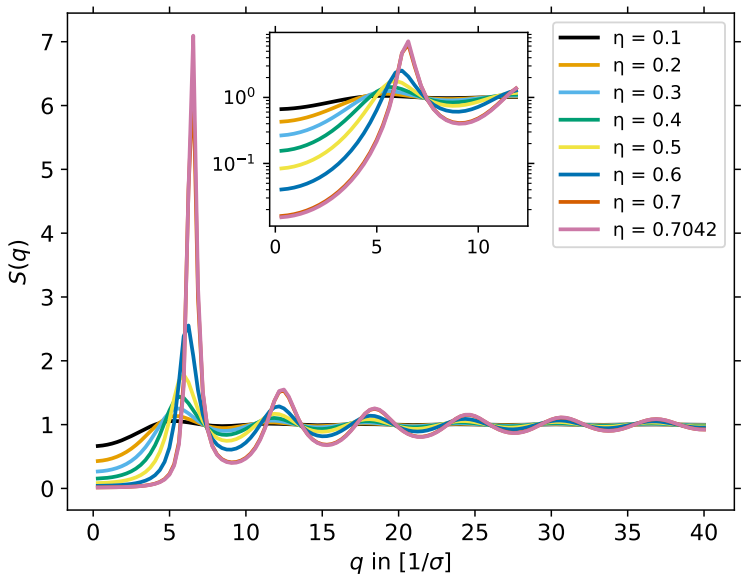

Figure 5.2: The figure highlights the static structure factor as it is utilized as the initial values for the differential equation's solution. The implementation is accomplished employing an extensive grid with $M = 128$ wave number points, leading to the demonstration of precisely this static correlation function for this specific number of wave numbers. The set of system parameters comprises $\{D_t = 1.0, \sigma = 1.0\}$.

Figure (5.3) portrays the intermediate scattering function for various packing fractions at different wave numbers, selected in the vicinity of the static structure factors' first maximum. Herein, specifically the passive Brownian particle limit is considered and juxtaposed against data generated by the passive MCT-code, represented by solid lines. The data obtained from the active code is indicated by the marker crosses. Evidently, both methodologies yield identical results, serving as an initial confirmation of the accuracy of the MCT numerical approach. The glass transition manifests for both approaches at a critical packing fraction of $\eta = 0.7042$. At this juncture, the system retains its non-ergodic nature, and the initial correlation remains frozen to an extent determined by the height of the plateaux, referred to as the non-ergodicity parameter. Upon examining the four illustrations, one can deduce that this non-ergodicity parameter oscillates in tandem with the oscillations observed in the static correlation function. Thus, the deviation of the ISF

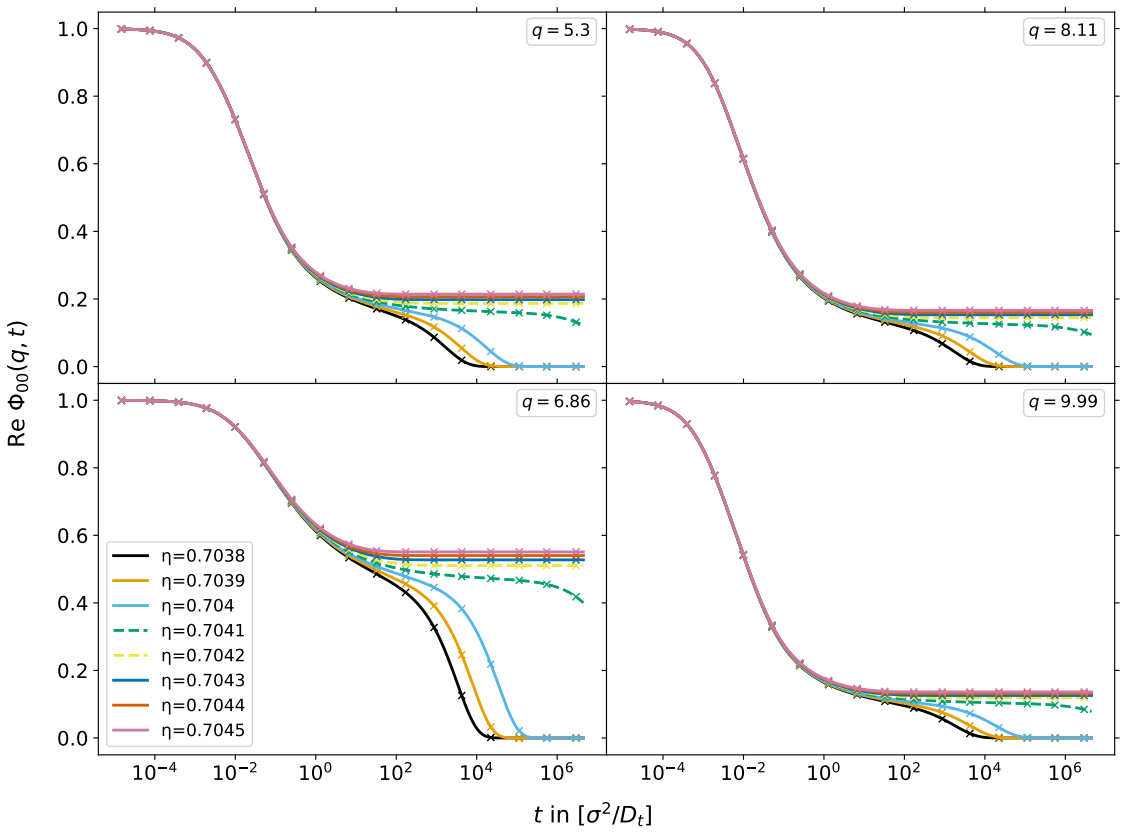

Figure 5.3: ISF around the critical packing fraction at wave numbers close to the first maximum of the static structure factor. The limit of a passive Brownian particle (PBP) is considered (markers) and compared to the result obtained from a numerical calculation for a PBP (solid lines). The system parameters are $\{\nu = 0.0, D_r = 0.0, v = 0.0\}$.

for different packing fractions is particularly pronounced at the first maximum of the static correlation function. It is important to mention that both the critical packing fraction and the non-ergodicity parameter slightly deviate from the values reported in the existing literature [23, 55]. Furthermore, it should be noted that the $(0, 0)$-component of the ISF is used for the comparison to passive MCT-data, since this component describes the spatial

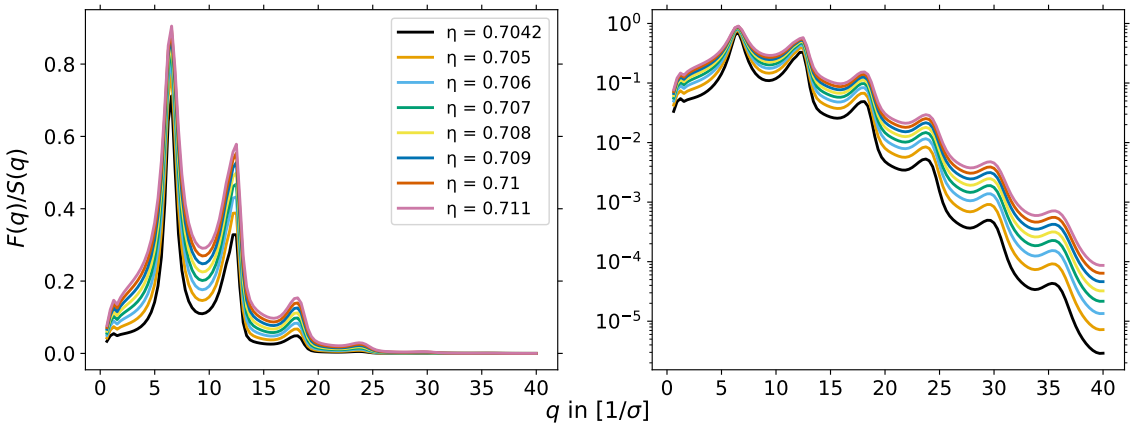

Figure 5.4: Normalized non-ergodicity parameter for passive Brownian particles. A grid of $M = 128$ wave numbers is used and the system parameters are $\{D_t = 1.0, \sigma = 1.0\}$.

correlations due to the absence of rotational contributions.

Figure (5.4) displays the non-ergodicity parameter, normalized by the static structure factor, for diverse packing fractions around the critical value. As anticipated, two prominent peaks are evident, coinciding with the first and second maxima of the structure factor. Notably, higher packing fractions correspond to elevated non-ergodicity parameters.

The slight deviation of the critical packing fraction in comparison to literature values observed in this implementation can be attributed to two factors. Firstly, the adoption of the DFT direct correlation function, and secondly, the critical packing fraction's dependence on the low wave number cutoff. In Chapter (3), bipolar coordinates are introduced, leading to an interior integral of the memory kernel that becomes an integration over the wave number, denoted as p, within the domain $[|q-k|, q+k]$. Given that the high q-cutoff is determined as $q_M = 40.0/\sigma$, it becomes evident that employing a different low q-cutoff would result in a varied number of summations in the integral. This outcome arises because the condition may no longer be satisfied by certain pairs of q and k, as was the case previously. It has been ascertained that the numerics remain stable even for relatively small wave numbers. Consequently, a low q-cutoff value of $q_1 = 0.3/\sigma$ has been selected. Notably, this value lies prior to the first decline in the critical packing fraction, as illustrated in Figure (5.5). On the whole, it can be stated that while the critical packing fraction exhibits jumps, it does not diminish to zero. Instead, it remains at reasonable values, fluctuating around $\eta_c = 0.701$.

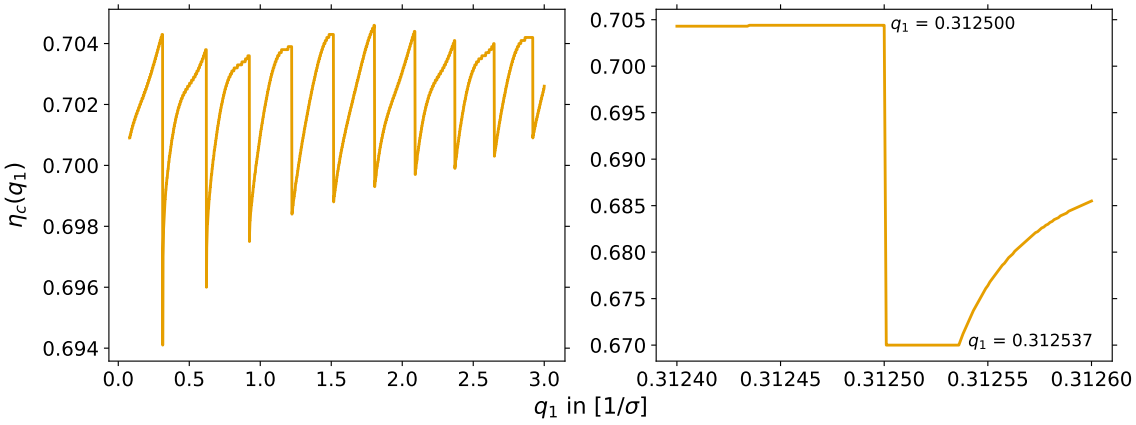

Figure 5.5: Illustration of the influence of the low wave number cutoff on the critical packing fraction. The implementation uses $M = 128$ wave numbers, a high q-cutoff of $40.0/\sigma$ and a set of system parameters given by $\{D_t = 1.0, \sigma = 1.0\}$.

5.2.2 Free Chiral Active Brownian Particle

The memory kernel, an essential component of the MCT-equation, redefines the system's dynamics by accounting for particle interactions. However, in the limit of exceedingly small densities, its influence can be neglected, simplifying the MCT-equation to

$$\partial_t \Phi(q,t) = -\omega(q)\Phi^{-1}(q)\Phi(q,t). \tag{5.3}$$

This simplified form is then solved by the exponential decaying function

$$\Phi(q,t) = \mathrm{e}^{-\omega(q)\Phi^{-1}(q)t}\,\Phi(q), \tag{5.4}$$

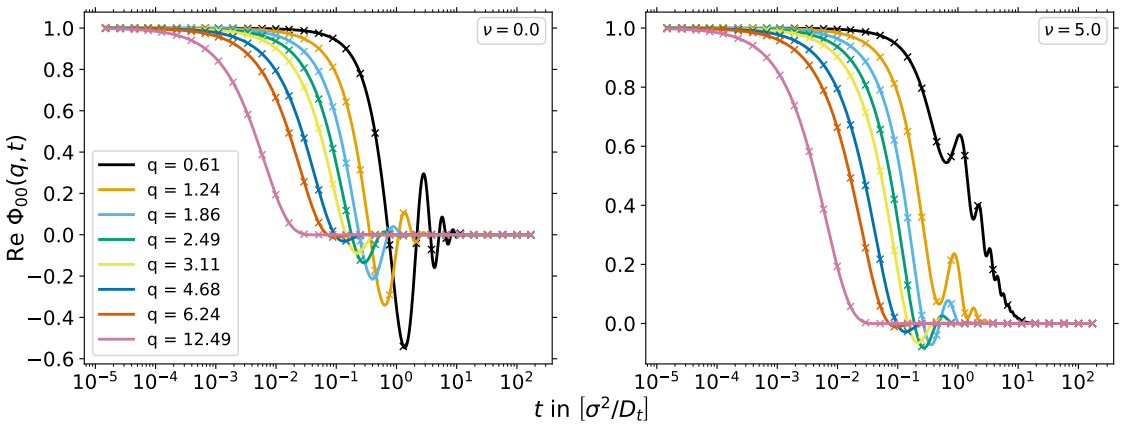

Figure 5.6: Free ISF for different wave numbers q, once for a vanishing circle swimmer frequency $\nu = 0.0$ and once for a finite one $\nu = 5.0$. The set of system parameters is given by $\{\eta = 0.0, D_r = 0.1, v = 5.0\}$.

that sets the static correlation function as initial values. Figure (5.6) exhibits this analytic solution, represented by solid lines, while the markers denote solutions obtained from the active MCT-code. The perfect agreement between both methods provides further evidence of the numerical implementation's accuracy. This congruence validates the correctness of the Backward-Euler implementation, the time decimation procedure, and the use of moments and auxiliary correlation functions in the numerical scheme, as described in Chapter (4).

Given that the density is set to zero, and consequently the packing fraction becomes negligible, the memory kernel vanishes in the numerical implementation. Thus, at this point, no definitive statement regarding the correctness of the memory kernel can be made, except for the previously demonstrated agreement between the active and passive codes in the passive Brownian particle limit.

The figures portray intriguing aspects: at vanishing packing fractions, higher wave numbers expedite the relaxation process in a strictly monotonic manner. Furthermore, the influence of the circle swimmer frequency can be observed, probing oscillations of the ISF before it tends to zero. Notably, these oscillations are more pronounced at very small wave numbers and completely vanish for larger ones. This observation aligns with the earlier discussion concerning the mean-squared displacement, where it was argued that oscillations can only be detected for $q < 1/l_p = 1.73$ for the considered parameter regime.

The representation wherein solid lines depict the analytic solution and markers correspond to the MCT-solution also applies to Figure (5.7) and Figure (5.8). These figures showcase the free ISF in two scenarios: one with a vanishing circle swimmer frequency and the other with a finite frequency of $\nu = 5.0$. To facilitate comparisons with previous studies that explored the ISF with wave vectors aligned in the y-direction, the current results are presented for this alignment as well. Achieving this entails transforming the output ISF of the MCT-code, initially oriented in the x-direction, to be aligned in the y-direction. Upon examination, the most evident aspect once again is the impeccable agreement between the analytic and numeric solutions. As wave numbers increase, the relaxation of functions accelerates accordingly. This behavior is consistent for both the diagonal and off-diagonal components of the ISF. However, a crucial point necessitates mention. The figure portrays the real part of the ISF for the $(0, 0)$-component, and for the off-diagonal elements. Here,

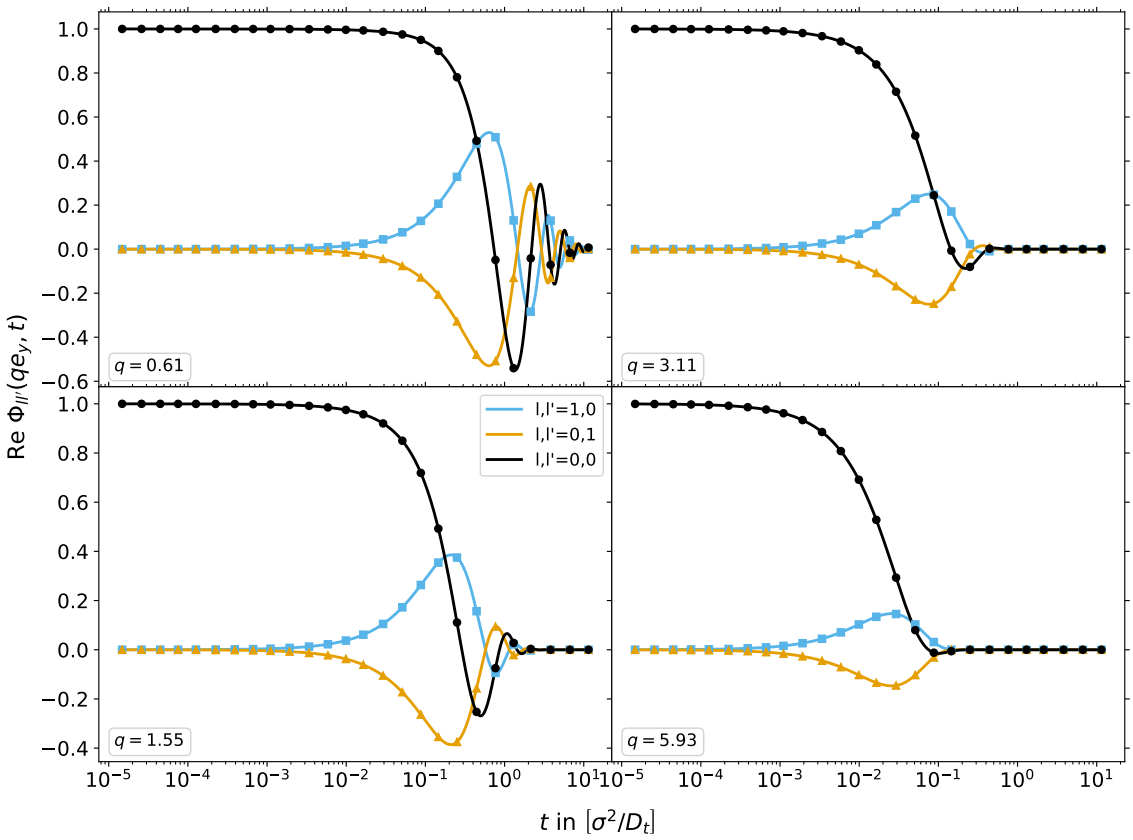

Figure 5.7: Free ISF for $\nu = 0.0$. Solid lines represent the analytic solution, markers indicate results from MCT-numerics. The parameters are given by $\{\eta = 0.0, D_r = 0.1, v = 5.0\}$.

caution must be exercised, as components of the ISF and SISF for a non-chiral ABP are either real or imaginary. However, in the case of a CABP, such as the one considered here, the situation differs, leading to non-vanishing imaginary parts for the $(0,0)$-component and non-vanishing real parts for the off-diagonal elements of the in x-direction transformed ISF and SISF.

The amplitude of off-diagonal cross correlations, specifically $(1,0)$ and $(0,1)$, are equal for a free (C)ABP, differing only in sign. Observing the data, it becomes evident that the amplitude of these oscillations diminishes as time progresses. Furthermore, this amplitude exhibits greater prominence for correlations encompassing longer distances, mirroring the oscillatory pattern of the $(0,0)$-component. The underlying physical interpretation of this phenomenon is nuanced. The spatial correlations find their scrutiny through the $(0,0)$-components of the ISF. In a scenario characterized by a finite rotational diffusion constant and swim speed, the system abandons detailed balance and ventures into a state of non-equilibrium. The oscillatory relaxation process captures this inherent non-equilibrium nature of the system, a feature absent in the context of passive Brownian particles. In the latter case, the ISF follows a strictly monotonic trajectory. This is a mathematical consequence engendered by the negative definite Smoluchowski operator with its sole nonpositive real eigenvalues. However, this distinctive trait is not sustained in the realm of active Brownian motion. The rationale behind the augmented amplitude for extended spatial distances can be elucidated by an escalated probability for a particle to revert to its initial position over such extended trajectories. Furthermore, the interplay between rotational and translational motion, captured by the off-diagonal components, discloses

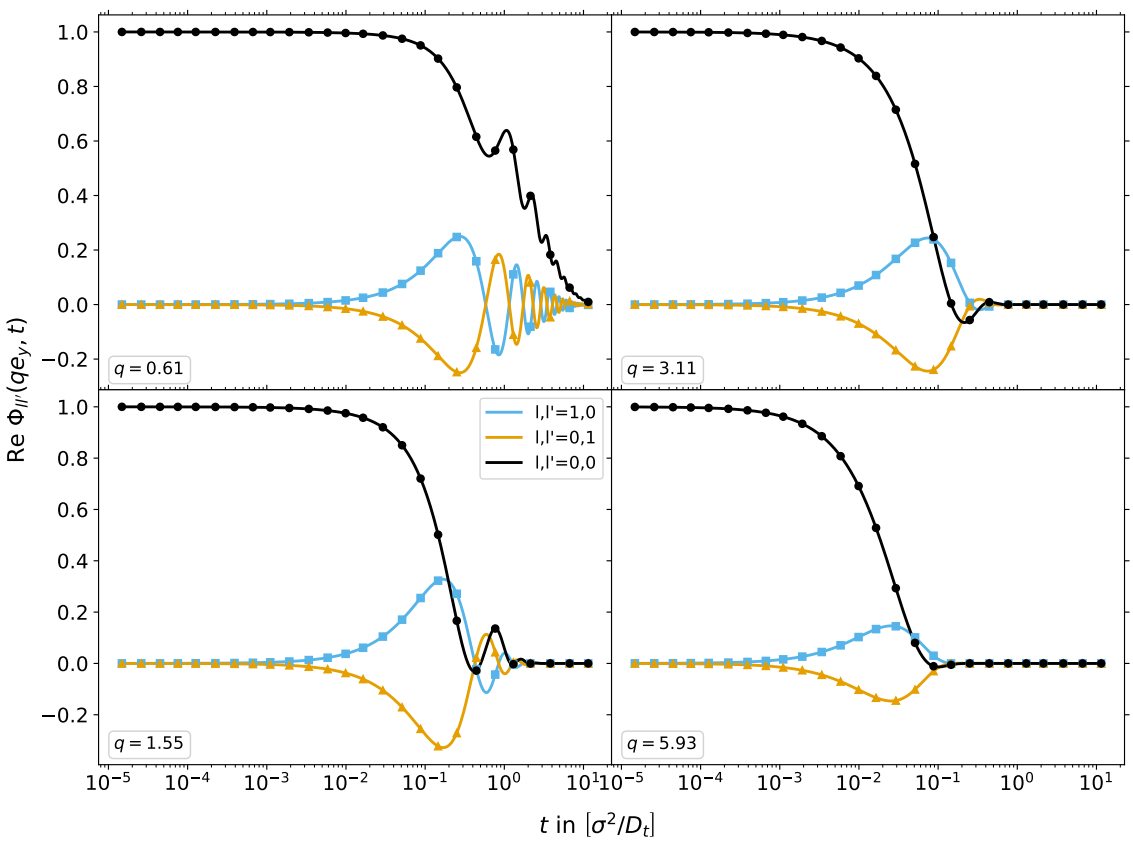

Figure 5.8: Free ISF for $\nu = 5.0$. Solid lines represent the analytic solution, markers indicate results from MCT-numerics. The parameters are given by $\{\eta = 0.0, D_r = 0.1, v = 5.0\}$.

an interesting trend. Initially, no discernible correlation exists between these distinct channels. However, as the particle initiates ballistic motion, correlation is magnified. Eventually, this correlation wanes again as the process evolves into complete randomization.

The impact of the rotational frequency comes into focus through the elucidation offered by Figure (5.8). Within the realm of anticipated oscillations, encompassing wave numbers below $q < 1/l_p = 1.73$, the oscillatory patterns are observable not just for the spatial correlation channels but also for the cross correlation channels. Within this domain, a heightened oscillatory frequency of the ISF is apparent, only to fade once this specific wave number threshold is surpassed. However, it's worth noting that the amplitude of these oscillations is comparatively lower compared to an ABP. This variance can be rationalized by the perturbed motion exhibited by a CABP due to the presence of the rotational frequency ν. An ABP generally displays a larger mean squared displacement than a CABP, making it less likely for the latter to return to its initial position with the same orientation. This discrepancy leads to a smaller amplitude. Nevertheless, this motion is simultaneously influenced by rotational behavior, which is evident in the heightened frequency of oscillations. This phenomenon is a consequence of the greater likelihood, in this case, of encountering a particle with a specific orientation and position after a given time interval.

5.2.3 The Effect of the Packing Fraction

The packing fraction η overwhelmingly governs the glassiness of the system. Consequently, Figure (5.9) illustrates the ISF (top) and SISF (bottom) across a wide range of densities,

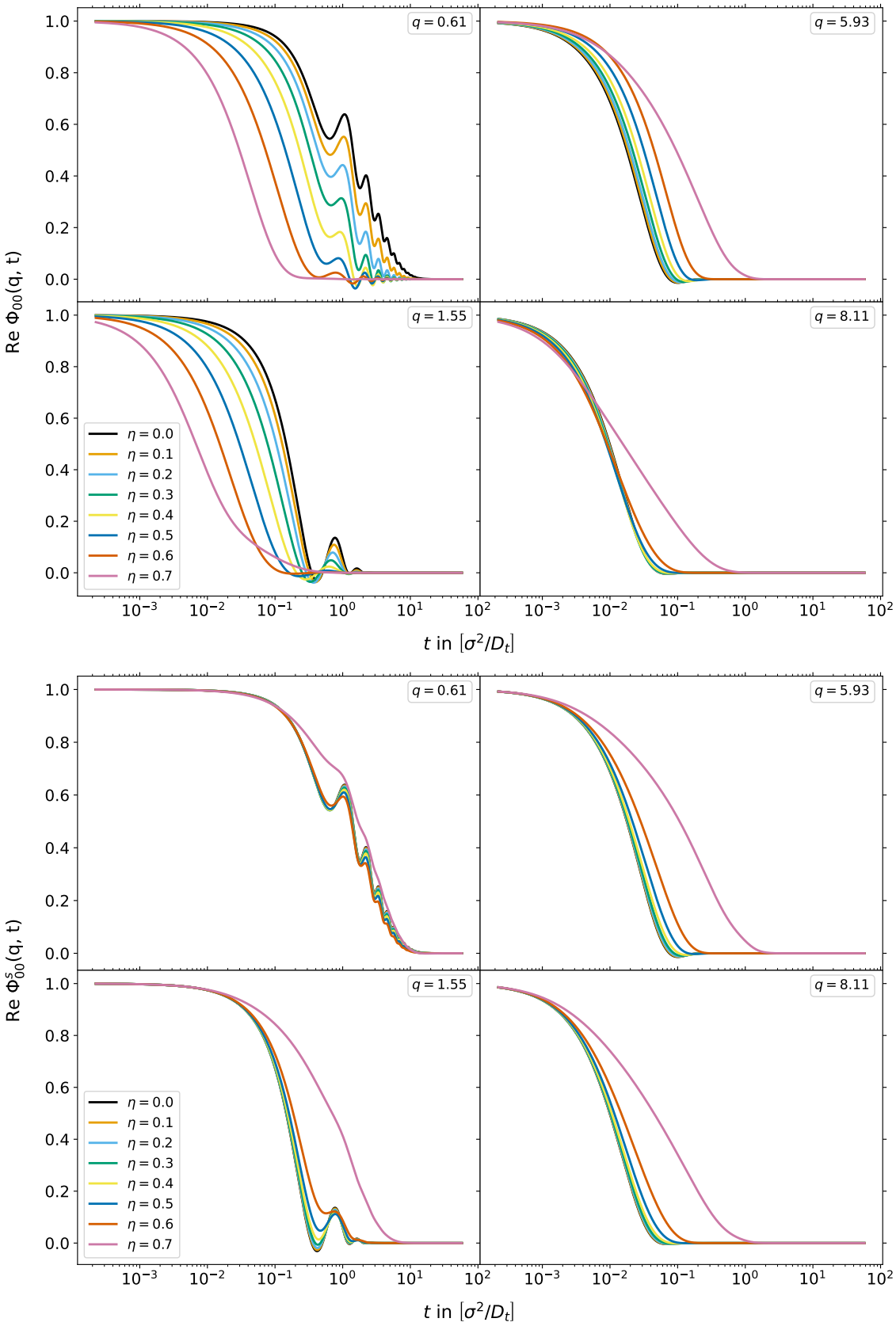

Figure 5.9: Real part of the (0,0)-component of the ISF (top) and the SISF (bottom) for varying packing fraction at different wave numbers q. The set of system parameters is given by $\{\nu = 5.0, D_r = 0.1, v = 5.0\}$.

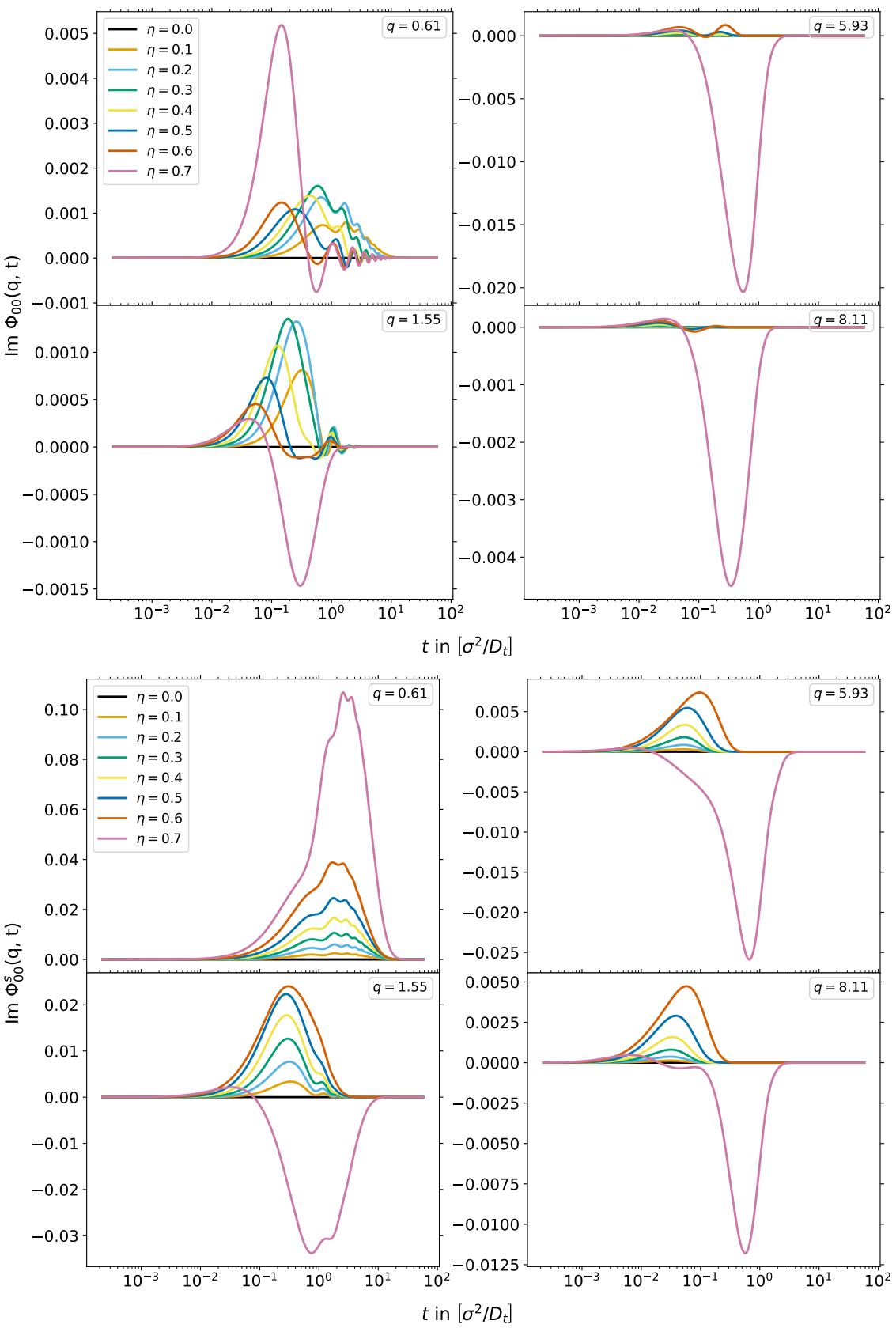

Figure 5.10: Imaginary part of the (0,0)-component of the ISF (top) and the SISF (bottom) for varying packing fraction at different wave numbers q. The set of system parameters is given by $\{\nu = 5.0, D_r = 0.1, v = 5.0\}$.

spanning from low to higher values. The data reveals that the collective dynamics of the ISF remains largely unaffected by the driven rotational frequency. Conversely, the SISF for a tagged particle exhibits pronounced oscillatory behavior. However, this behavior is confined to the realm of small wave numbers, specifically for $q < 1/l_p = 1.73$. Furthermore, the SISF also displays a diminishing oscillatory pattern in the proximity of the glass transition. The ISF exhibits a discernible oscillatory pattern within the context of small packing fractions, confined to the regime above the length scale determined by the persistence length. The rationale underlying this behavior is fundamentally intuitive. When a circle swimmer fails to complete a full circle, the correlation between its initial and subsequent positions isn't significantly amplified. This holds true not only for correlations spanning distances shorter than the calculated free persistence length, but also for dense systems where such a distinctive feature cannot be sustained collectively. In the case of a tagged particle, its circular motion is subject to a less pronounced influence compared to that of the collective system, as it might traverse regions of lower density. This behavior undergoes alteration in proximity to the glass transition, where the translational and circular motion of the tagged particle becomes notably constrained.

An additional feature worth noting pertains to the relaxation time of both functions. While a more thorough investigation of this aspect is reserved for a subsequent section, preliminary observations indicate that the relaxation time for the ISF seems to defy the conventional expectation that higher packing fractions result in slower relaxation processes, particularly for specific wave numbers. The underlying reason for this phenomenon lies in the nature of the static correlation function. For a tagged particle, it reduces to an identity matrix, whereas for the interacting system, it transforms into a diagonal matrix, encompassing the static structure factor. Consequently, the SISF exhibits a monotonously faster decay with increasing wave numbers. In contrast, the behavior of the ISF is influenced by the rising initial structure, modulated by the static structure factor, at certain distances probed by the latter.

Figure (5.10) portrays the imaginary part of the transient correlation function. The non-zero imaginary part is made plausible by the drift, proportional to a factor $\mathrm{e}^{il\nu t}$, that the circle swimmer frequency causes. The data illustrates that the initial and final correlation is indeed zero. With the exception of very small wave numbers, a larger packing fraction is associated with a stronger correlation.

5.2.4 The Glass Transition

The upper part of Figure (5.11) delineates the ISF within a parameter range corresponding to a glass-forming system. Evident within this depiction is that a glassy state can occur for a finite swim speed. Only a swim speed of sufficient magnitude is able to break the glass. This observation concurs with findings documented for ABP in [55]. A more detailed examination of swim speed is reserved for a subsequent section. Notably, it can be observed herein that an elevated swim speed augments the capacity of particles to liberate themselves from their confining cages, thereby accelerating the relaxation process or even precipitating the dissolution of a glassy system. The influence of swim speed is more pronounced in regions characterized by higher wave numbers. The lower segment of Figure (5.11) depicts the SISF. In this context, the impact of swim speed is distinctly discernible across all wave numbers. Furthermore, the non-ergodicity parameter exhibits a monotonic descent as wave numbers increase. When $v = v^s = 1.0$, numerical instability becomes evident, with the constant plateau overlaid by oscillations featuring divergent amplitudes over time. For the temporal regime under consideration, this effect remains relatively minor and thus becomes smoothed out before plotting. The presentation encompasses the corrected ISF and SISF for this particular scenario.

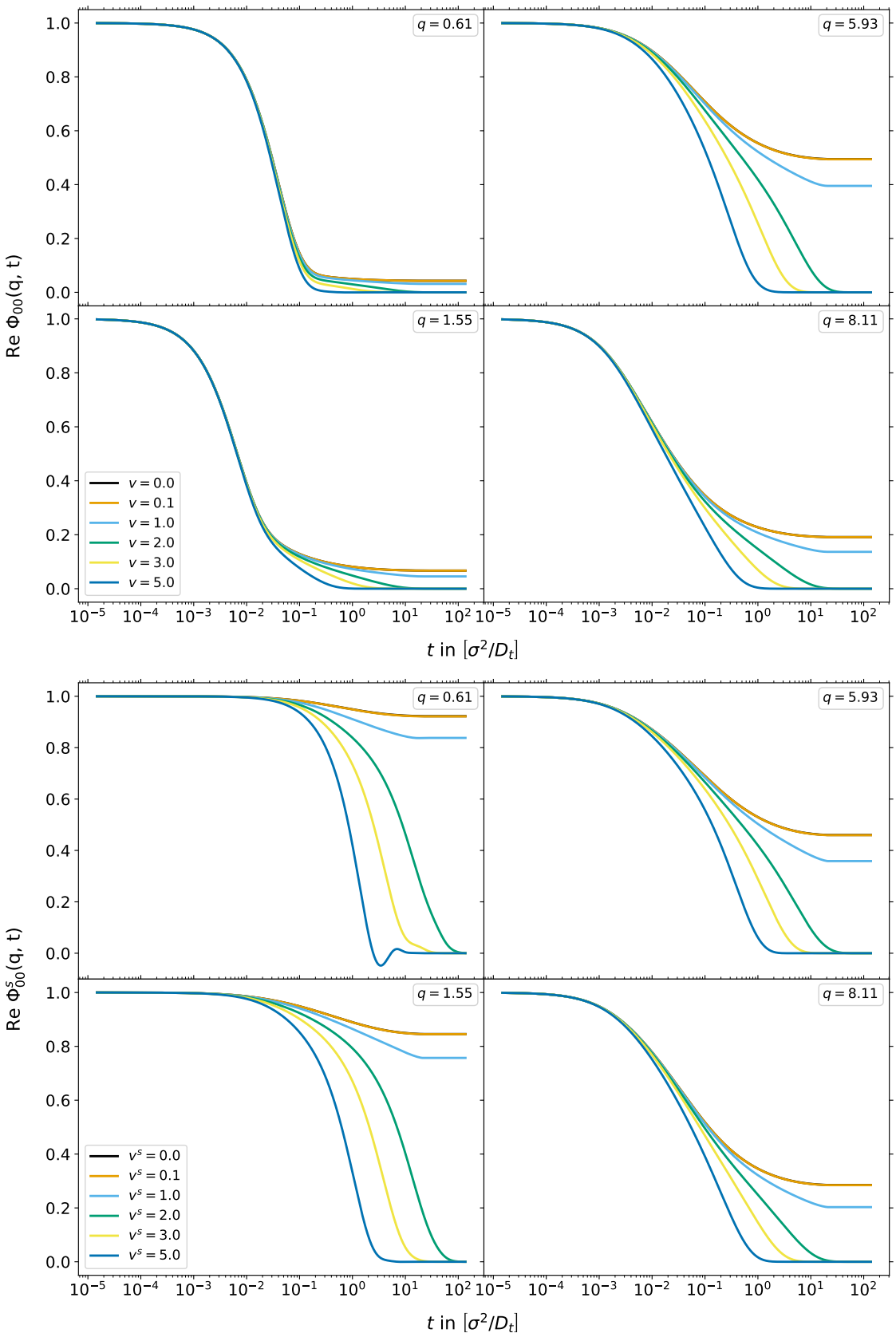

Figure 5.11: ISF (top) and SISF (bottom) for varying swim speed $v = v^s$ and different wave vectors q, for a packing fraction of $\eta = 0.705$. The set of system parameters is given by $\{\nu = 0.1, D_r = 0.01\}$.

5.2.5 The Effect of the Rotational Frequency

In Figure (5.12), the ISF for various rotational frequencies ν and q-values is displayed. The shape of these functions is quite similar to that of typical active Brownian particles [23, 24, 55], and the effect of the rotational frequency shows only a minor impact. This is interesting, because the mean-squared displacement of a single free chiral active Brownian disk, for the same system parameters, shows a profound dependence on the rotational strength. The same holds for the ISF of such an particle. Nevertheless, the many particle system differs from that, indicating that the feature of a circle swimmer frequency is of local significance.

The correlation time in relation to the wave number q once again fluctuates in alignment with the configuration of the static structure factor, diverging from the pattern observed for the SISF in the lower portion of the figure. A particularly pronounced attribute lies in the oscillations, most vivid when considering small wave numbers. These oscillations delve into longer relaxation times and the emergence of oscillations within the SISF at an earlier juncture. Analogously, the same trend pertains to the rotational frequency ν. Elevated values of ν exert a substantial impact primarily on small wave numbers, effectively probing the characteristic oscillatory tendencies of CABP. However, as wave numbers increase, this influence dissipates, and the oscillatory behavior fades. Nonetheless, a higher rotational constant does manifest in noticeably sluggish relaxation of correlation functions, a feature observable across both the ISF and SISF. Furthermore, for a higher circle swimmer frequency the undershoots in the ISF and SISF vanish. This can be explained by the altered persistence length of the system compared to a persistence length of ABP. For CABP an enhanced circle swimmer frequency decreases the persistence length to such an extend, that it can be resolved for all displayed correlation distances, or adequately their wave numbers.

An additional intriguing aspect to consider is the influence of the packing fraction. Although previously addressed, another noteworthy observation emerges in this context. While the conventional oscillatory behavior diminishes with heightened densities, the impact of the circle swimmer frequency continues to exert significant influence on the ISF and SISF, particularly at elevated wave numbers within this high-density regime. However, a reversal of this trend becomes apparent for exceedingly small wave numbers. In such instances, the rotational frequency holds greater sway over the correlation functions, especially within the context of lesser packing fractions. This phenomenon, however, does not carry over to the imaginary components of the $(0, 0)$-component of the ISF and SISF, as depicted in Figure (5.13). In this case, the effect of higher correlation values remains conspicuous for higher densities without exception. Additionally, larger wave numbers contribute to heightened correlations. Notably, prior speculation on the possibility of finite imaginary components being a numerical artifact within the implementation is cast into doubt by the SISF data, which showcases correlations attaining significant magnitudes. A subtle instability becomes apparent within the SISF data at a wave number of $q = 1.55$. Regrettably, the reason for this instability's occurrence at this specific wave number remains elusive, as such anomalies could theoretically manifest at larger or smaller wave numbers. It is worth mentioning that higher rotational diffusion constants have contributed to instabilities in previous implementations. Furthermore, the choice of a notably small low q-cutoff might also contribute to such instabilities. Remarkably, the circular frequency is not distinct from the rotational diffusion constant within this context, as both engender divergent behavior if chosen appropriately large. This effect is particularly pronounced within a non-ergodic system, where a constant value can be enveloped by initiating oscillations eventually tending towards infinity.

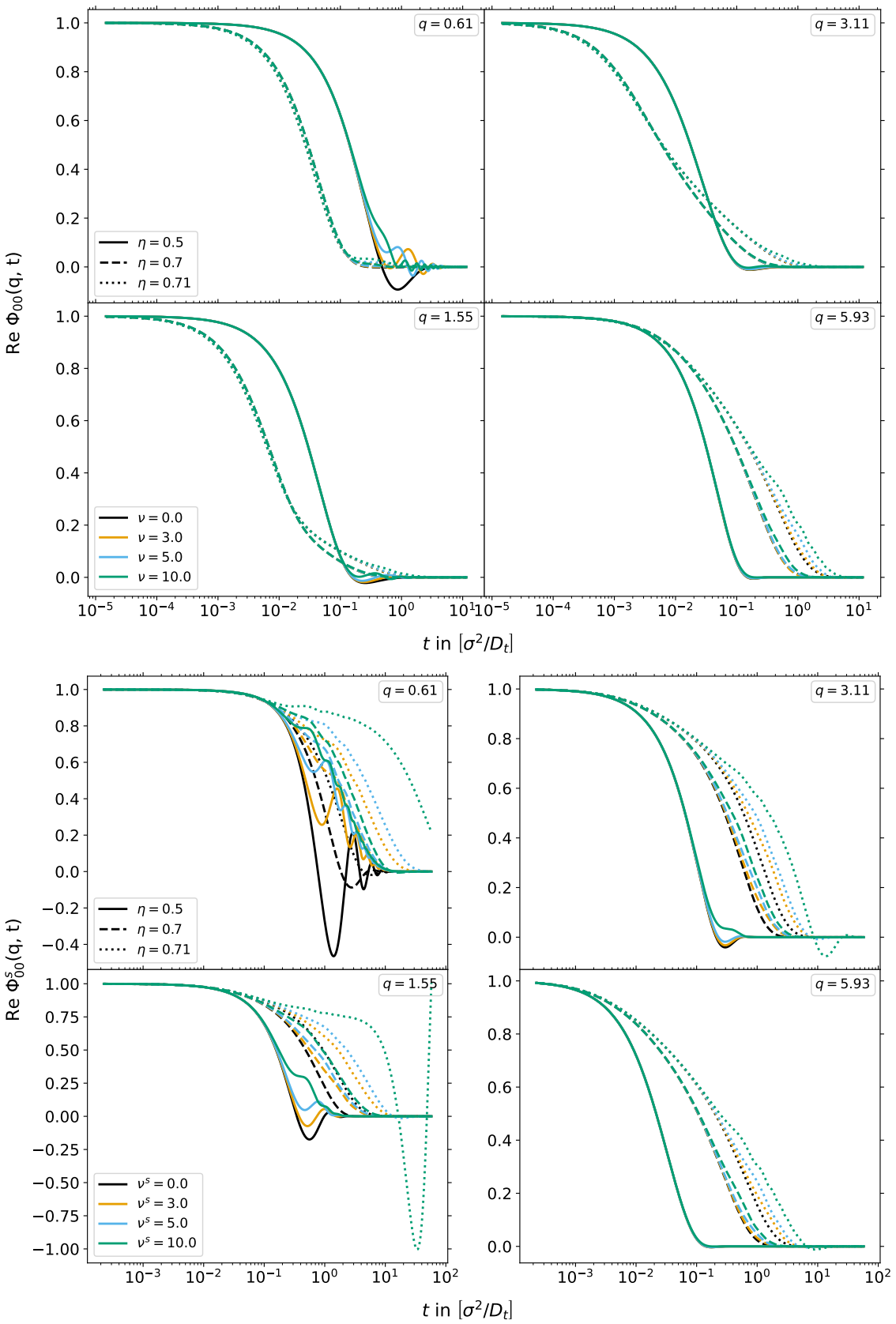

Figure 5.12: Real part of the (0,0)-component of the ISF (top) and SISF (bottom) for varying rotational frequencies ν. The set of system parameters is given by $\{D_r = 0.1, v = 5.0\}$.

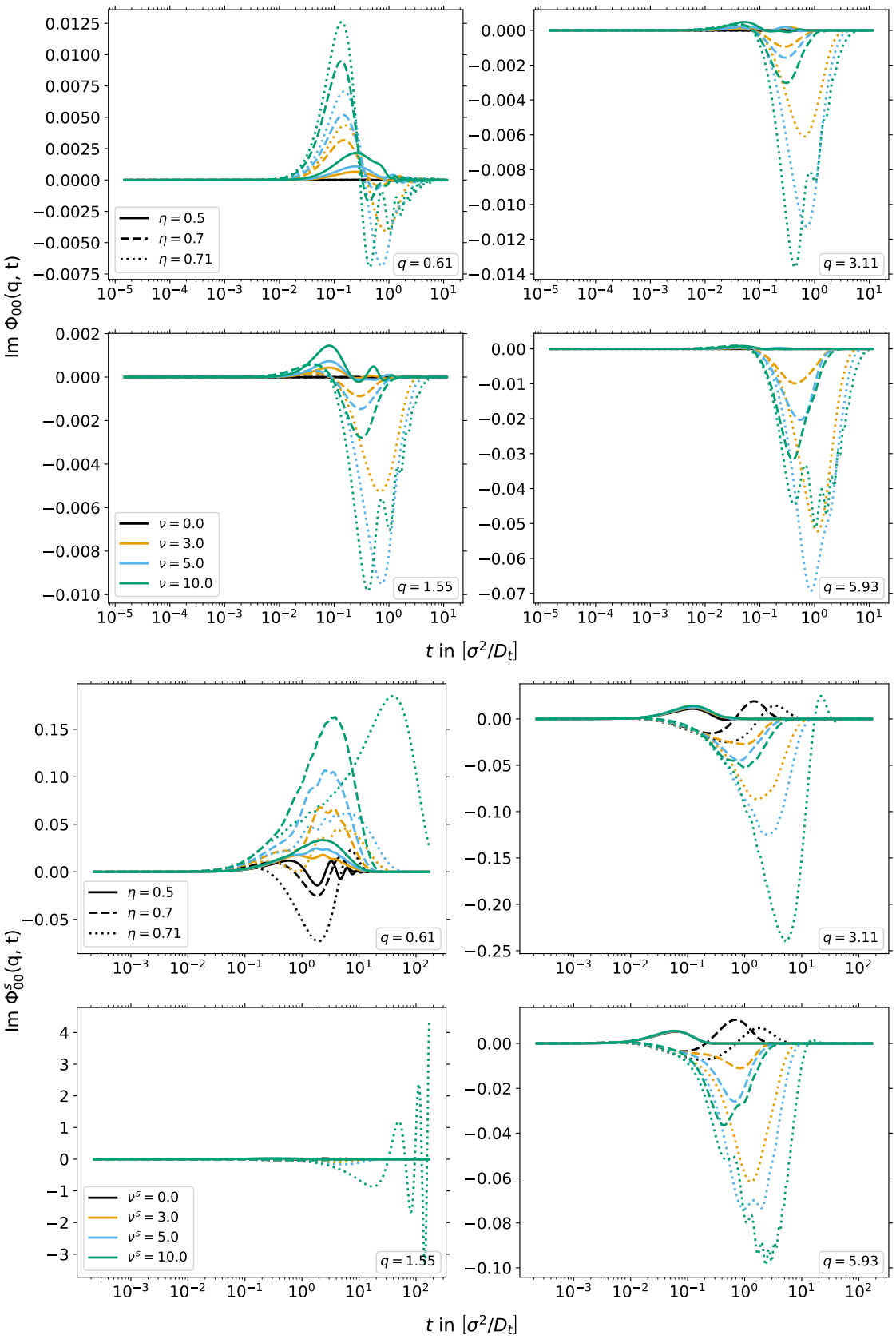

Figure 5.13: Imaginary part of the (0,0)-component of the ISF (top) and the SISF (bottom) for varying rotational frequencies ν. The set of system parameters is given by $\{D_r = 0.1, v = 5.0\}$.

Figure (5.14) portrays the imaginary part of two interrelated relaxation channels within the ISF, while Figure (5.15) mirrors the same for the SISF. Prior to delving into the data's description, a pivotal aspect concerning the cross correlation channels demands attention. The dynamics between Φ_{01} and Φ_{10} are nuanced, as the correlation function in the context of active particles embodies a non-symmetric matrix. The Φ_{01} component encompasses a Smoluchowski operator that engages with a density function featuring a finite rotational contribution. Consequently, this operator delves into the rotational behavior of the particle, which in turn influences its translational motion. Through the act of applying the dual vector that is the other density on that expression, and the ensuing completion of the inner product, this effect translates into the subspace that underlies the particle's translational motion. Consequently, the Φ_{01} component might indeed undergo relaxation on timescales akin to those of the Φ_{00} component. This temporal trajectory can even exceed the typical timescales dictated by the particle's rotational motion, eventually converging to a finite value and contributing to the emergence of a glass transition. A comparable plateau was previously observed for ABP in Reference [55]. In contrast, a particle invariably retains its capacity for rotation, owing to its rotational diffusion constant, even when the parameter space ushers in the formation of a glassy state. As a result, the other component, Φ_{10}, invariably undergoes relaxation on a reorientational timescale. Below this temporal threshold, the influence of the particle's translational motion on its orientation remains substantial.

The initial matter of consideration when examining the two figures pertains to this aspect. For the ISF, the $(1, 0)$-component manifests greater correlations than its counterpart when dealing with smaller wave numbers. However, as the wave number approaches the first peak of the static structure factor, a specific wave number threshold is encountered wherein this trend is inverted. At this juncture, the impact of rotational behavior on translational dynamics supersedes the reciprocal influence. The underlying rationale for this phenomenon is relatively straightforward: at this particular wave number, the considered correlation distances align with a greater number of particles. As the system achieves higher density, a phenomenon expounded upon by observing the lower portion of the figure, this characteristic effect becomes attenuated. Consequently, elevated density yields more potent amplitudes and a higher sensibility towards the circle swimmer's frequency. For both the lower and higher of the two densities, an increased circle swimmer frequency yields a stronger emergence of correlation values. These oscillations exhibit greater frequency yet are characterized by diminished amplitude.

The SISF exhibits an unsurprising alignment with the circle swimmer frequency. However, a notable distinction arises when juxtaposed with the ISF. In the case of the SISF, both cross correlation channels manifest a more comparable structure. At a lower packing fraction of $\eta = 0.5$, the divergence between the two components almost vanishes. This could be attributed to the fact that the particles have more space to move and rotate, making their overall motion more similar. Conversely, this trend does not hold true for the larger packing fraction, and its disparity accentuates further for higher wave numbers. These observations are compounded by the fact that the magnitude of correlation is significantly lower for the SISF in comparison to the ISF. Moreover, a consistent trait characterizes all oscillatory curves: a growing correlation value over time prior to oscillation commencement, which may descent below zero.

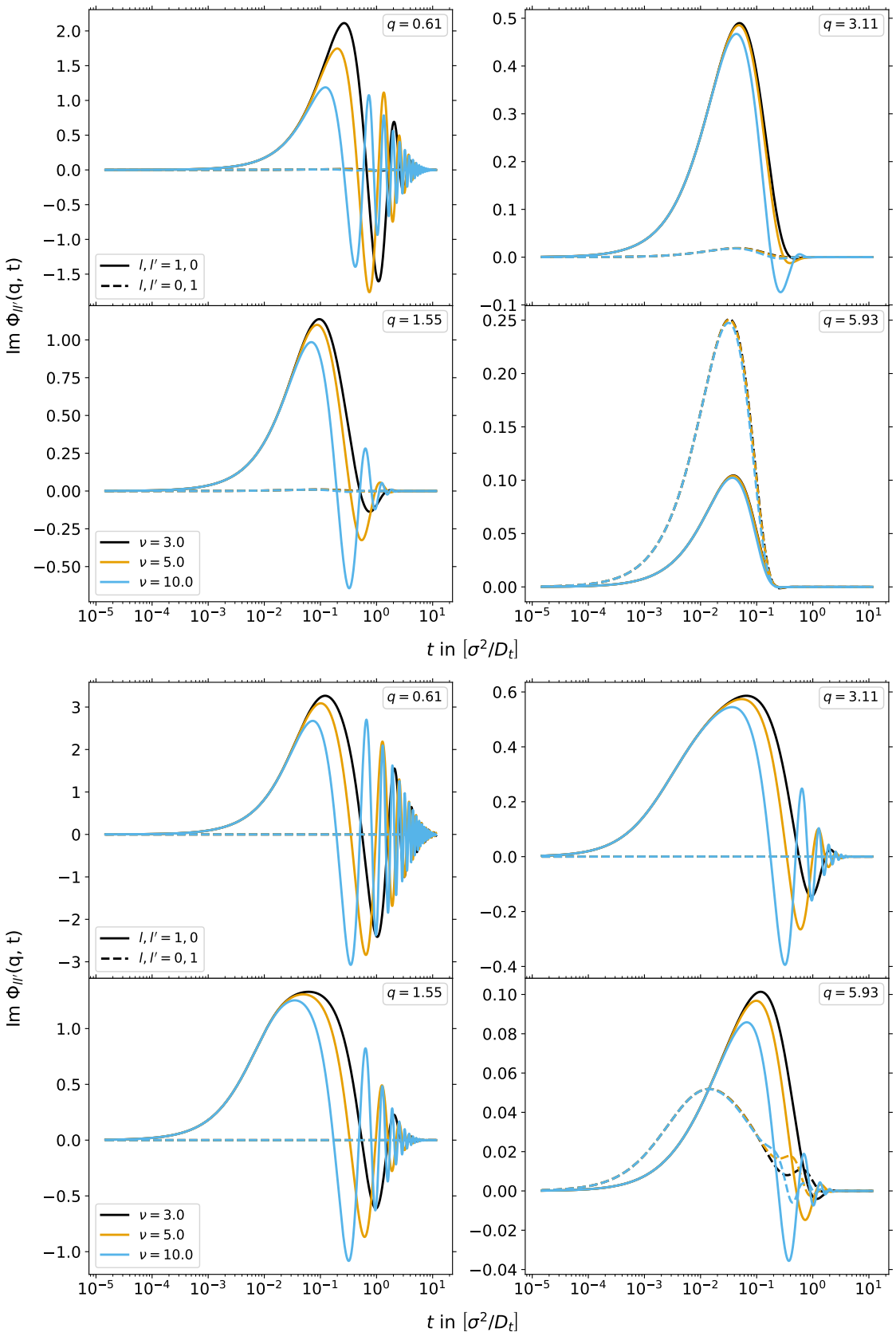

Figure 5.14: Imaginary part of ISF for varying rotational frequencies ν and different wave numbers q once for a packing fraction of $\eta = 0.5$ (top) and once for $\eta = 0.7$ (bottom). The set of system parameters is given by $\{D_r = 0.1, v = 5.0\}$.

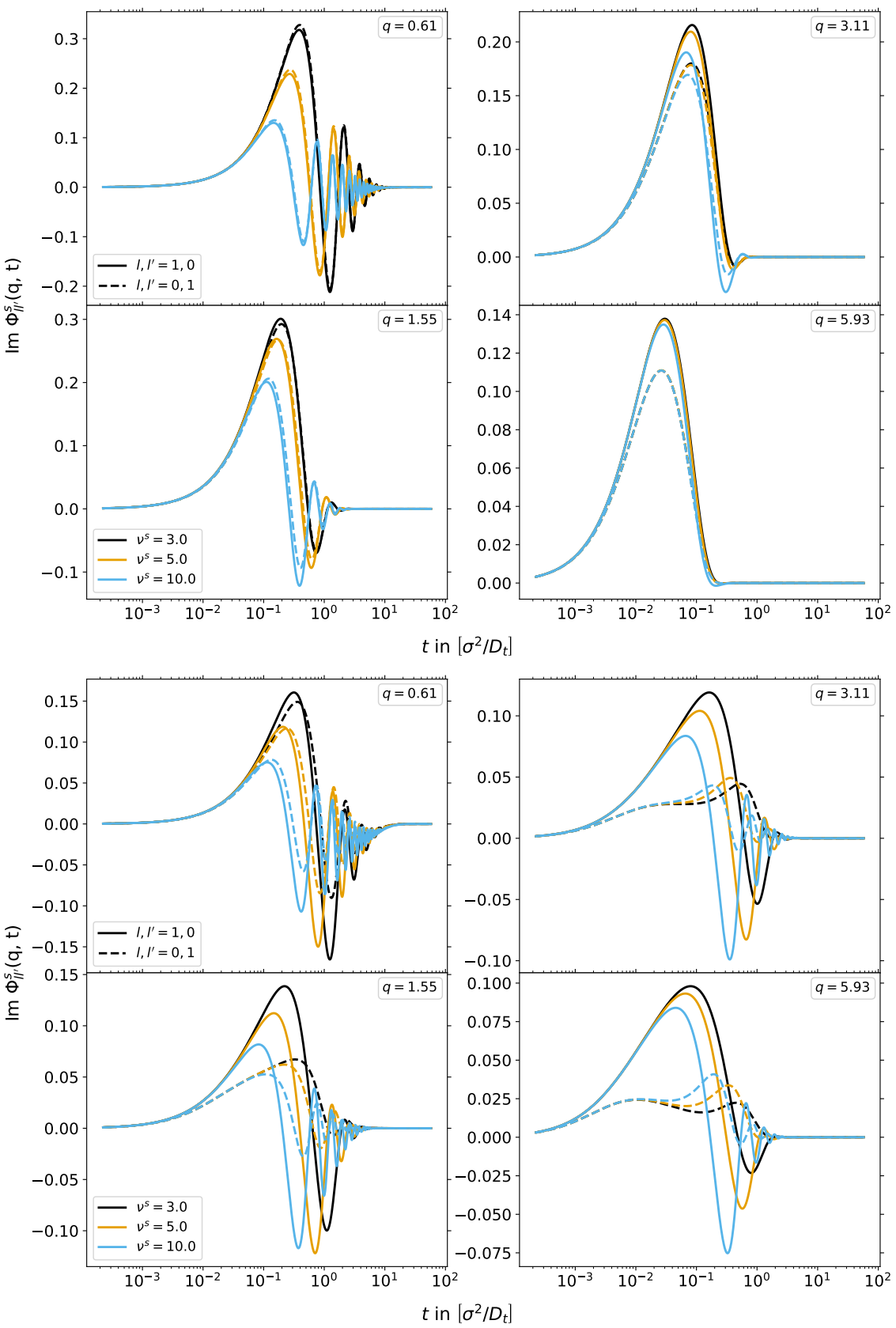

Figure 5.15: Imaginary part of SISF for varying rotational frequencies ν and different wave numbers q once for a packing fraction of $\eta = 0.5$ (top) and once for $\eta = 0.7$ (bottom). The set of system parameters is given by $\{D_r = 0.1, v = 5.0\}$.

5.2.6 The Effect of the Rotational Diffusion Constant

The primary aim of this section is to investigate the influence of the rotational diffusion constant on the system's behavior. A similar analysis has been previously conducted for active Brownian particles in studies by Liluashvili [55] and Reichert [23]. However, the addition of the circle swimmer frequency introduces an additional feature that may alter the impact of the rotational diffusion constant. To facilitate a more comprehensive comparison, the ISF and SISF data incorporate values for a vanishing circle swimmer frequency. This approach allows to assess the deviations introduced by the frequency to the system's dynamics.

Figures (5.16), (5.17) and (5.18) clearly demonstrate that a larger diffusion constant curtails the particles' ability to break free from the confining influence of neighboring particles, as their directed motion becomes impaired. As a result of this behavior, longer relaxation times are observed for higher rotational diffusion constants. Furthermore, greater D_r^s, D_r results in lesser oscillations in the SISF. This phenomenon can be attributed to the larger diffusion that curtails the rotational behavior's driven aspect and is described by the towards zero tending Péclet number (5.2). This means that the effective diffusion constant is approximately given by the translational one $D_L \approx D_t$. For an exceedingly large diffusion constant of $D_r = D_r^s = 100.0$, the influence of a circle swimmer frequency diminishes significantly when compared to the case of a vanishing circle swimmer frequency. Similarly, the impact of the circle swimmer frequency becomes negligible for higher wave numbers. Moreover, the effect of the rotational diffusion constant also diminishes accordingly. Overall, it becomes apparent that the rotational diffusion constant exerts a more pronounced influence on the SISF than on the ISF.

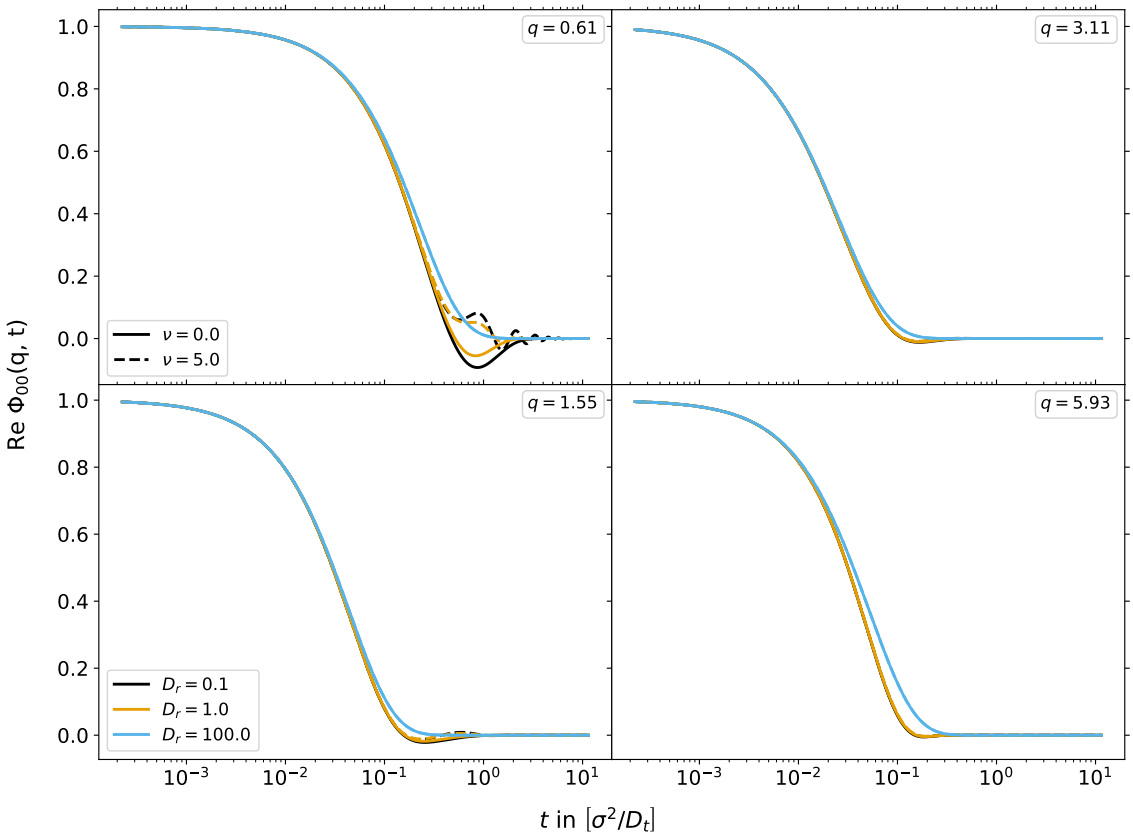

Figure 5.16: ISF for varying rotational diffusion constants D_r and different wave numbers q, for a packing fraction of $\eta = 0.5$. The set of system parameters is given by $\{\nu = 5.0, v = 5.0\}$.

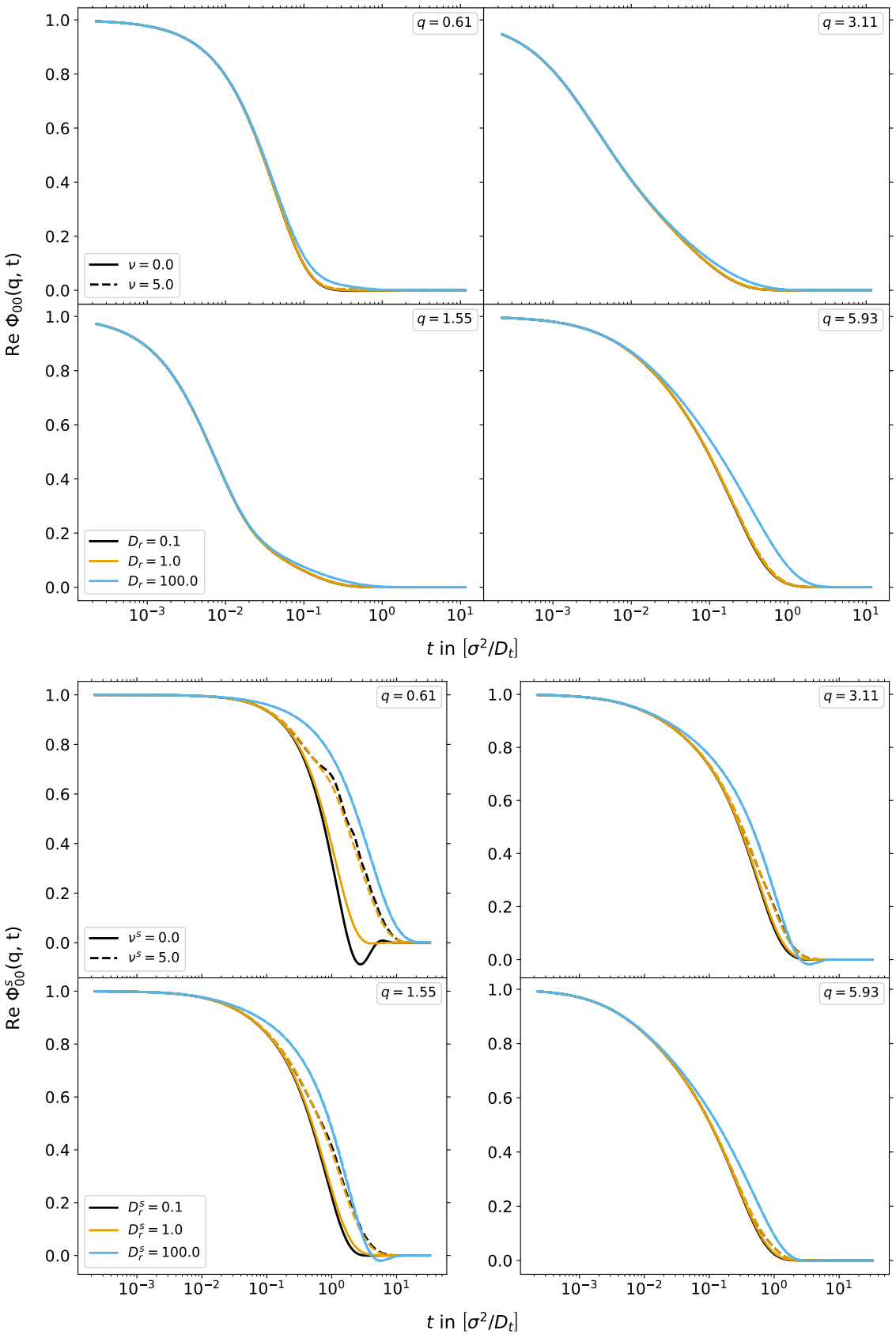

Figure 5.17: ISF (top) and SISF (bottom) for varying rotational diffusion constants D_r and different wave numbers q, for a packing fraction of $\eta = 0.7$. The set of system parameters is given by $\{\nu = 5.0, v = 5.0\}$.

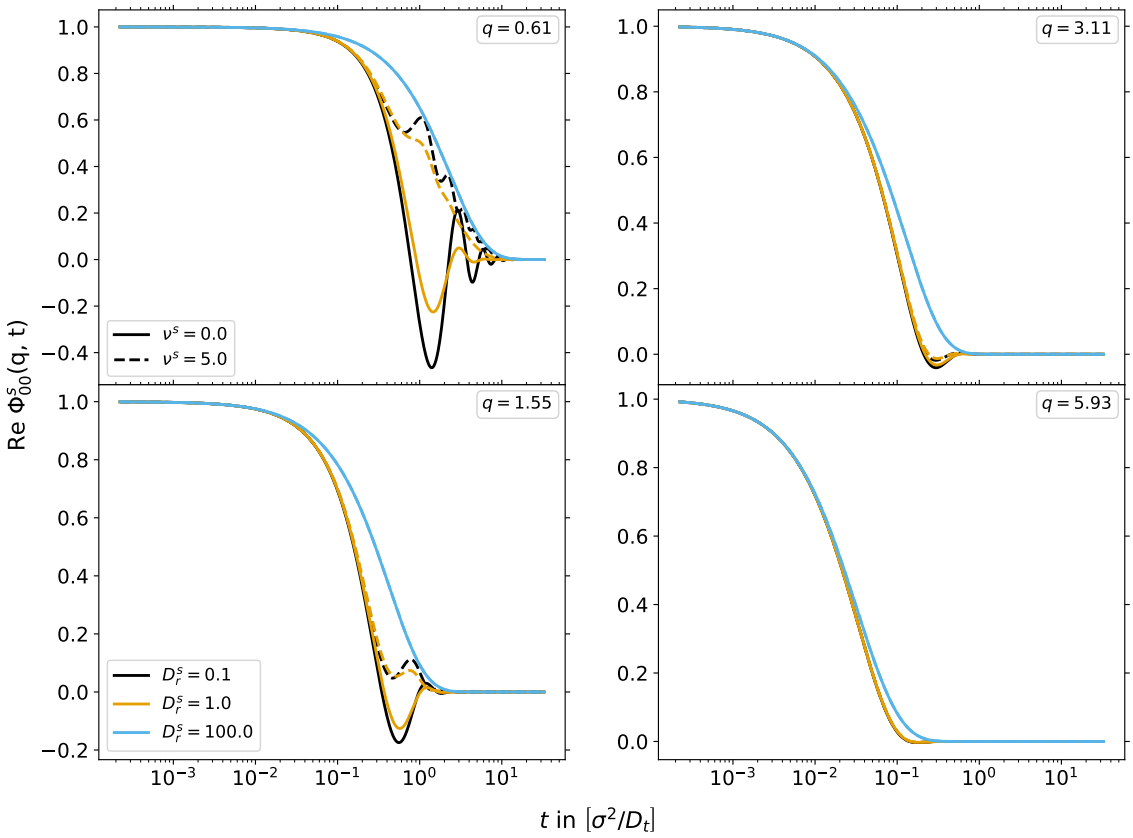

Figure 5.18: SISF for varying rotational diffusion constants D_r and different wave numbers q, for a packing fraction of $\eta = 0.5$. The set of system parameters is given by $\{\nu = 5.0, v = 5.0\}$.

5.2.7 The Effect of the Swim Speed

The response of the system to variations in swim speed v is examined in Figure (5.19) and Figure (5.20) both for intermediate and high densities. Notably, an increase in swim velocity enhances the particles' capacity to liberate themselves from their surrounding cages, leading to a swifter relaxation of the functions under scrutiny. This behavior is especially conspicuous for smaller distances, that is, larger wave numbers, in both the ISF and SISF, as aptly captured by the data. Evidently, swim speed exerts a profound influence on the shape and dynamics of these functions. For the SISF, higher swim speeds yield earlier and generally faster oscillations, without altering the strength of the oscillations represented by their amplitudes. However, these oscillations are suppressed for larger wave numbers.

An intriguing departure from the behavior of other model parameters is that the effect of swim velocity becomes more pronounced at larger wave numbers. In essence, it tends to impact correlations over shorter distances more than those over longer distances. Additionally, it is noteworthy that even substantial swim speeds do not alter this effect, hinting that MCT might have underestimated the influence of swim speed. This aspect is a subject of discussion when comparing MCT-data to ED-BD-data in the subsequent section. It is also worth highlighting the distinctive behavior observed in the self-intermediate density functions, where very strong undershoots occur. Such behavior arises when the wave number, determined by the persistence length, falls below the corresponding critical wave number, thereby limiting the resolution and preventing the resolution of the particles' persistence length.

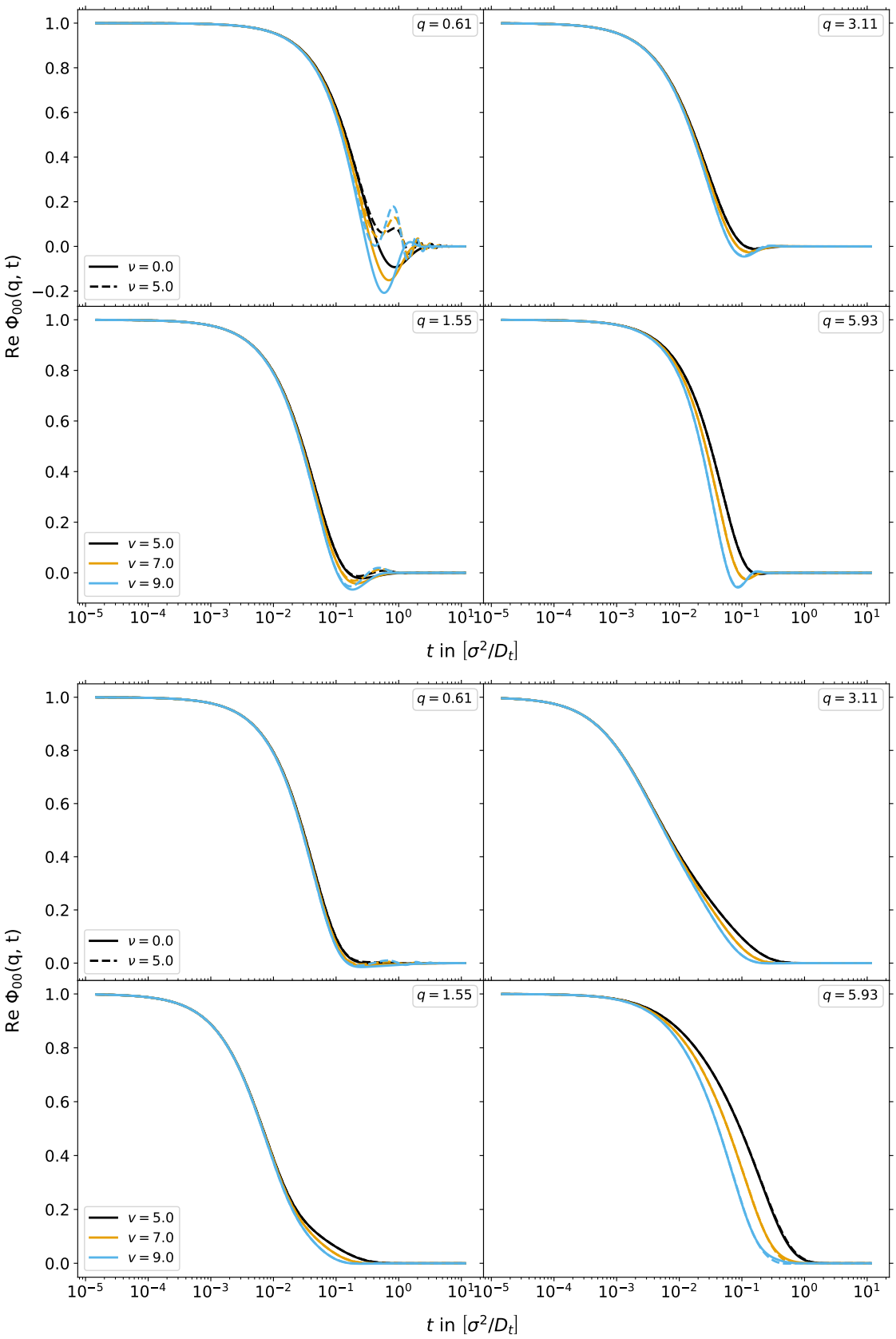

Figure 5.19: ISF for varying swim speed v and different wave vectors q, once for a small packing fraction of $\eta = 0.5$ (top) and once for $\eta = 0.7$ (bottom). The set of system parameters is given by $\{\eta = 0.5, \nu = 5.0, D_r = 0.1\}$.

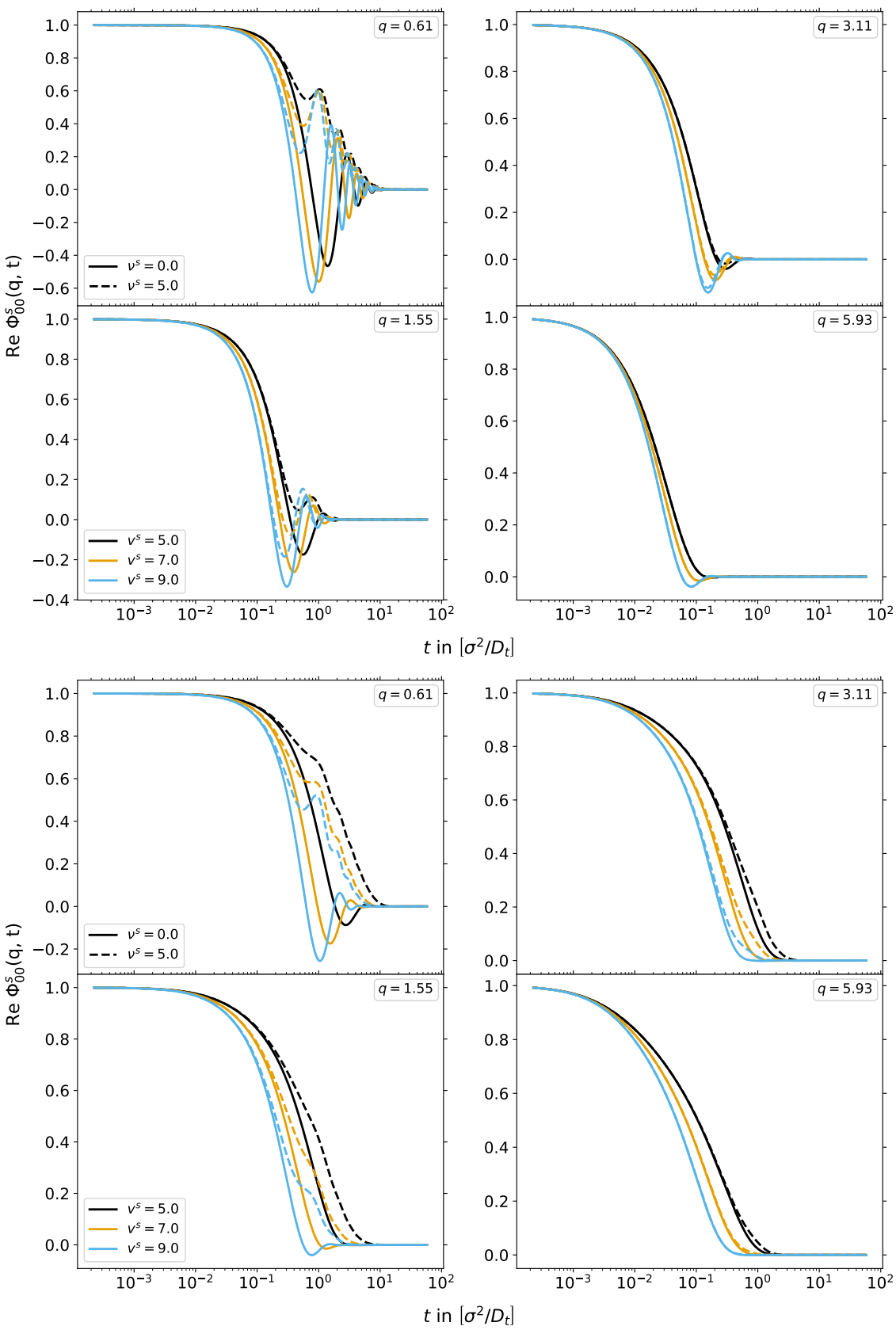

Figure 5.20: SISF for varying swim speed v and different wave vectors q, once for a small packing fraction of $\eta = 0.5$ (top) and once for $\eta = 0.7$ (bottom). The set of system parameters is given by $\{\eta = 0.5, \nu = 5.0, D_r = 0.1\}$.

5.3 Comparison with Simulation Results

In conclusion, the SISF computed within the framework of MCT is subjected to a comparison with simulation outcomes, with a specific focus directed towards the low-q behavior that reveals the distinctive oscillatory nature intrinsic to the chiral movement of CABP. In the ensuing analysis, the value of D_r is set to 0.1 in order to accentuate the persistence effects characteristic of this motion. An established understanding gleaned from investigations of passive systems indicates that MCT tends to predict an ideal glass transition point that diverges by roughly 15% from the transition point pinpointed through simulations [71]. To facilitate a meaningful comparison of MCT-results pertaining to structural relaxation in the vicinity of the glass transition, a conventional practice involves contrasting MCT-outcomes corresponding to a shifted packing fraction denoted as η_{MCT} with simulations conducted at a higher η_{BD}. Employing a linear mapping approach is customary, as it effectively underscores that the crux of the density-driven fluctuations is encapsulated within the MCT-predictions. Furthermore, broadening the scope of comparison to encompass simulations encompassing significantly lower densities, the mapping scheme can be logically extended to encompass quadratic deviations, a methodology that has demonstrated its efficacy in the context of ABP [24].

In the present study, BD-simulation results for $\eta_{\mathrm{BD}} = 0.1$, 0.5, and 0.72 are investigated. In order to match the relaxation times of the passive SISF these are mapped to $\eta_{\mathrm{MCT}} = 0.176, 0.664, 0.697$ for $q = 0.5, 1.0, 1.5$, and to $\eta_{\mathrm{MCT}} = 0.17, 0.551, 0.686$ for all larger wave numbers, respectively. Since the simulation uses a different q-grid than the MCT-numerics, the wave numbers accessible to compare with are limited. For the comparision the theory results thus are interpolated to wave numbers used in BD. The density shift involves generating simulation data for packing fractions around a particular value, such as $\eta_{\mathrm{BD}} = 0.7$, for passive Brownian particles. A loop over packing fractions is then created, and for each value, the MCT-numerics is called. Through a minimization procedure that involves summing up all elements of the ISF for a particular q-value and minimizing the square of that sum, i.e. using a least-square method, the values for η_{MCT} that best match a specific packing fraction of the ED-BD-simulation are found.

In Figure (5.21), one observes the correlation functions that have been modified through density mapping. The upper illustration portrays an exclusive density mapping at a wave number of $q = 7.5$. It becomes apparent that this sole mapping proves insufficient for resolving the SISF at low wave numbers. In truth, the vertex contributions exhibit a lack of precision for small wave numbers. Owing to their minor back-coupling in the memory kernel, a second mapping within this parameter regime appears judicious. The lower segment of the illustration demonstrates the alignment of ED-BD-data with MCT-data when both mappings are executed. The overall congruence between them is pronounced, with any deviation manifesting itself solely in the vicinity of larger packing fractions that approach the glass transition point.

Finally, using a quadratic fit, η_{MCT} can be expressed as a function of η_{BD}, given by

$$\begin{aligned} \eta^{<}_{\mathrm{MCT}} &= -0.553\eta^2_{\mathrm{BD}} + 0.819\eta_{\mathrm{BD}} + 0.394, \\ \eta^{>}_{\mathrm{MCT}} &= -0.587\eta^2_{\mathrm{BD}} + 1.271\eta_{\mathrm{BD}} + 0.073. \end{aligned} \tag{5.5}$$

Here, $\eta^{<}_{\mathrm{MCT}}$ denotes the packing fraction obtained from a small density mapping at $q = 1.0$ and $\eta^{>}_{\mathrm{MCT}}$ denotes the packing fraction for the density mapping at $q = 7.5$. The fit result

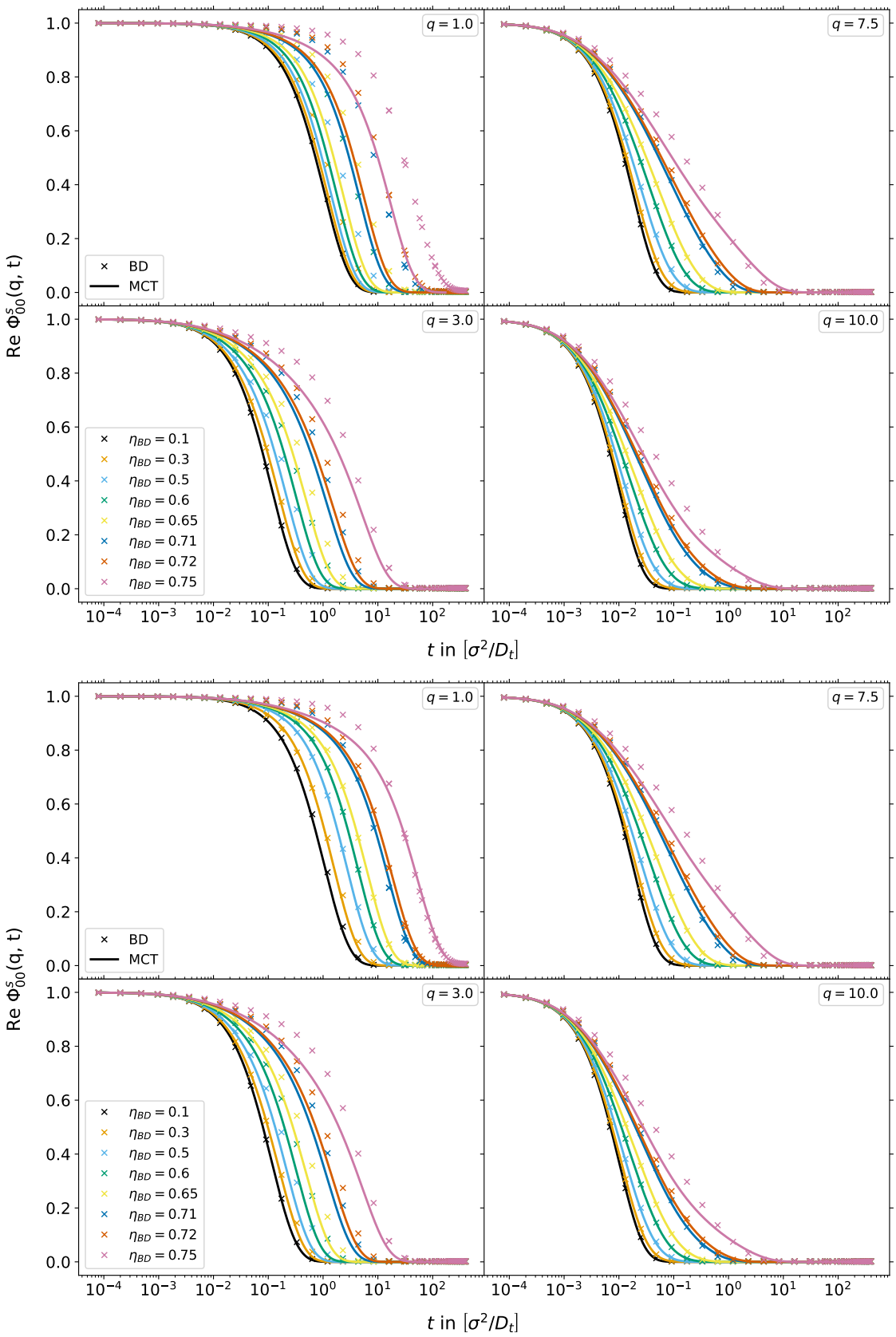

Figure 5.21: SISF for various packing fractions η, once calculated by MCT (lines) and once by ED-BD (markers). The top panel illustrates the results for four different wave numbers for a mapping exclusively performed for a wave number of $q = 7.5$. The bottom panel shows the result if a further mapping for $q = 1.0$ is made. The set of system parameters is given by $\{\nu = \nu^s = 0.0, D_r = D_r^s = 0.0, v = v^s = 0.0\}$.

can also be rephrased as

$$\begin{aligned}
\eta_{\mathrm{BD}} - \eta_{\mathrm{BD,c}} &= \frac{1}{C}(\eta_{\mathrm{MCT}} - \eta_{\mathrm{MCT,c}}) + \frac{1}{C'}(\eta_{\mathrm{BD}} - \eta_{\mathrm{BD,c}})^2, \\
\eta_{\mathrm{BD}} - 0.767 &= -\frac{1}{0.0293}(\eta^{<}_{\mathrm{MCT}} - 0.7042) - \frac{1}{0.053}(\eta_{\mathrm{BD}} - 0.767)^2, \\
\eta_{\mathrm{BD}} - 0.767 &= \frac{1}{0.3705}(\eta^{>}_{\mathrm{MCT}} - 0.7042) + \frac{1}{0.6312}(\eta_{\mathrm{BD}} - 0.767)^2,
\end{aligned} \tag{5.6}$$

where $\eta_{\mathrm{BD,c}}$ and $\eta_{\mathrm{MCT,c}}$ denote the critical packing fraction for the ED-BD-simulation and the MCT-numercis, respectively. The fit is also shown in Figure (5.22).

Figure (5.23) presents a comparison between the SISF obtained from a MCT calculation and that derived from a BD simulation. It reveals a wave number regime where the SISF oscillations vanish. Moreover, the data showcases a congruence, especially in the limit of lower densities and higher wave numbers. To achieve this, a mapping was conducted for the lower three wave numbers by setting the swim velocity as $v_{\mathrm{MCT}} = 0.6 v_{\mathrm{BD}}$ for the highest of the three densities. This mapping does not align with that employed in Reference [23], where a mapping of $v_{\mathrm{MCT}} = 1.5 v_{\mathrm{BD}}$ was performed to acknowledge MCT's tendency to underestimate the influence of swim speed. Here, no mapping must be performed for larger wave numbers. Furthermore, the mapping at low wave numbers shows that MCT overestimates the effect of swim speed in this regime. This effect proves particularly significant in densely packed systems for density fluctuations over short distances, which is why only this regime is subjected to a mapping. In addition, Figure (5.23) also offers a comparison for small wave numbers. Prior studies in active matter generally employed low wave number cutoffs of approximately $q = 2.5/\sigma$ to stabilize the numerical solution [23–25, 55]. In this work, a lower cutoff of $q = 0.3/\sigma$ is employed to observe the oscillatory behavior of the correlation functions. Admittedly, this lower cutoff introduces some lack of accuracy. Nevertheless, its implementation allows for the observation of the oscillatory behavior.

When comparing the MCT-data with simulation data, interpolation to specific wave numbers becomes necessary due to differences in the usage of underlying grids. This deviation in grid usage results in a certain lack of accuracy, too, particularly evident in the regime of the smallest wave numbers for large and intermediate densities.

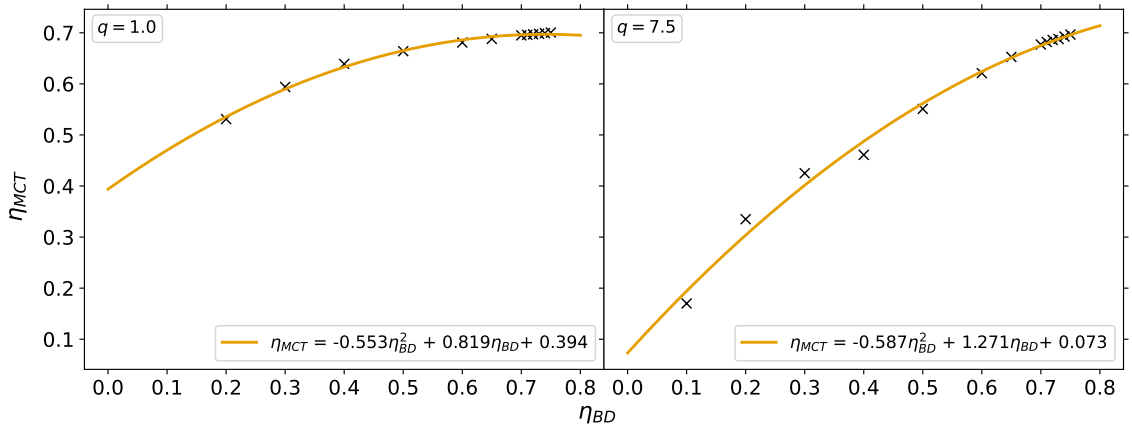

Figure 5.22: Quadratic least-square fit to find the dependence between the packing fraction used in the ED-BD-simulation and that for the MCT-numerics. Two kinds of mappings are performed, one for a small wave number of $q = 1.0$ (left) and one for a larger wave number of $q = 7.5$ (right).

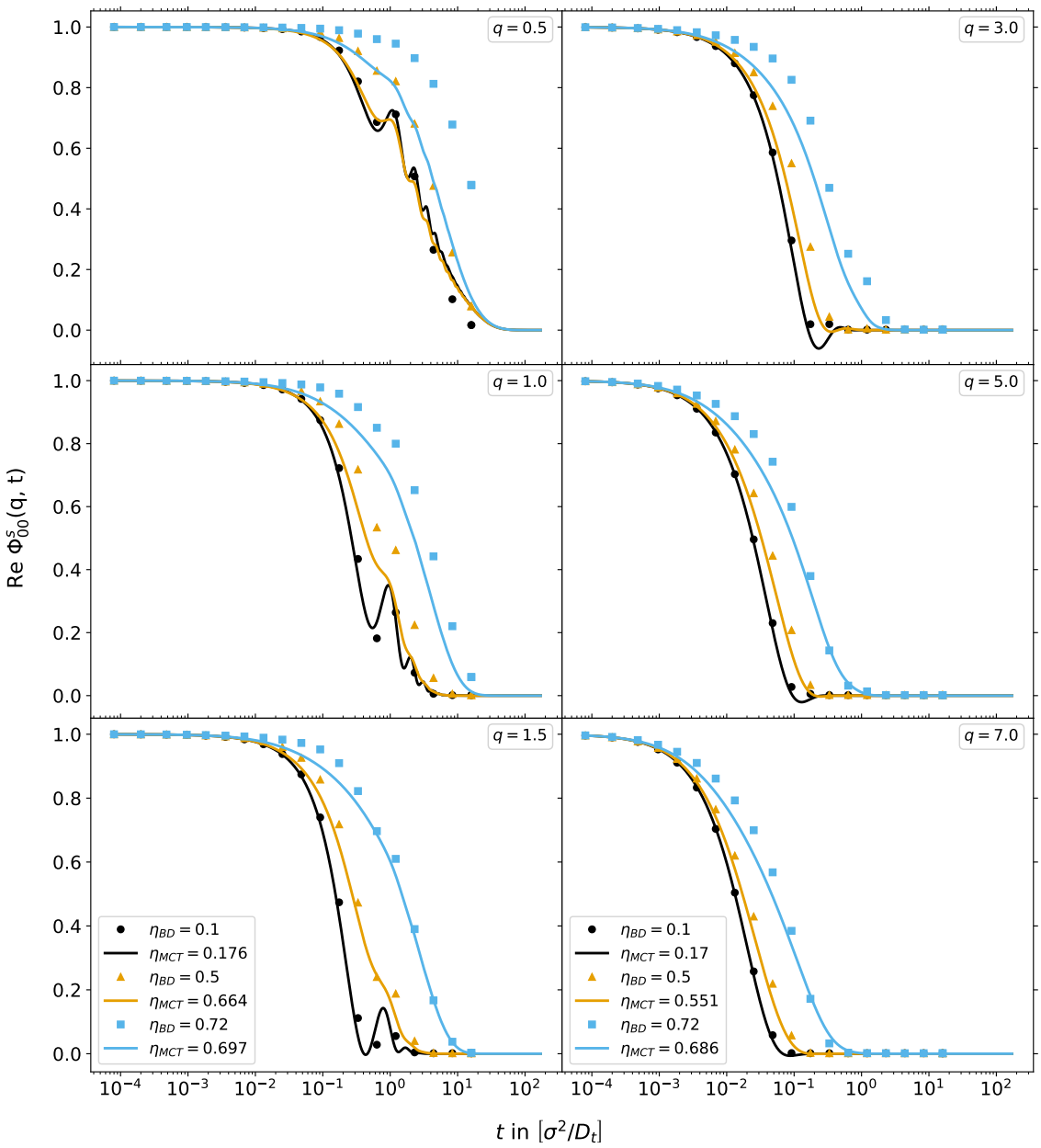

Figure 5.23: SISF from MCT and ED-BD for different wave numbers q. The low wave number mapping for $q = 1.0$ is performed for the figures on the left side, whereas the standard density mapping at $q = 7.5$ is utilized for the plots on the right side. The caption shows the corresponding MCT-packing fraction for the corresponding column. Furthermore, a mapping of the swim speed is made for the highest of the three densities for the pictures on the left side that reads $v_{\mathrm{MCT}} = 0.6 v_{\mathrm{BD}}$. The set of system parameters is given by $\{D_t = D_t^s = 1.0, v = v^s = 5.0, D_r = D_r^s = 0.1, \nu = \nu^s = 5.0\}$.

5.4 The Relaxation Time

A more in-depth investigation of the relaxation times of the ISF and SISF is warranted. The relaxation time is delineated as the temporal juncture at which the correlation function has attenuated to a level less than 1% of its initial magnitude and remains beneath this threshold. This framework accommodates the presence of plausible oscillatory tendencies

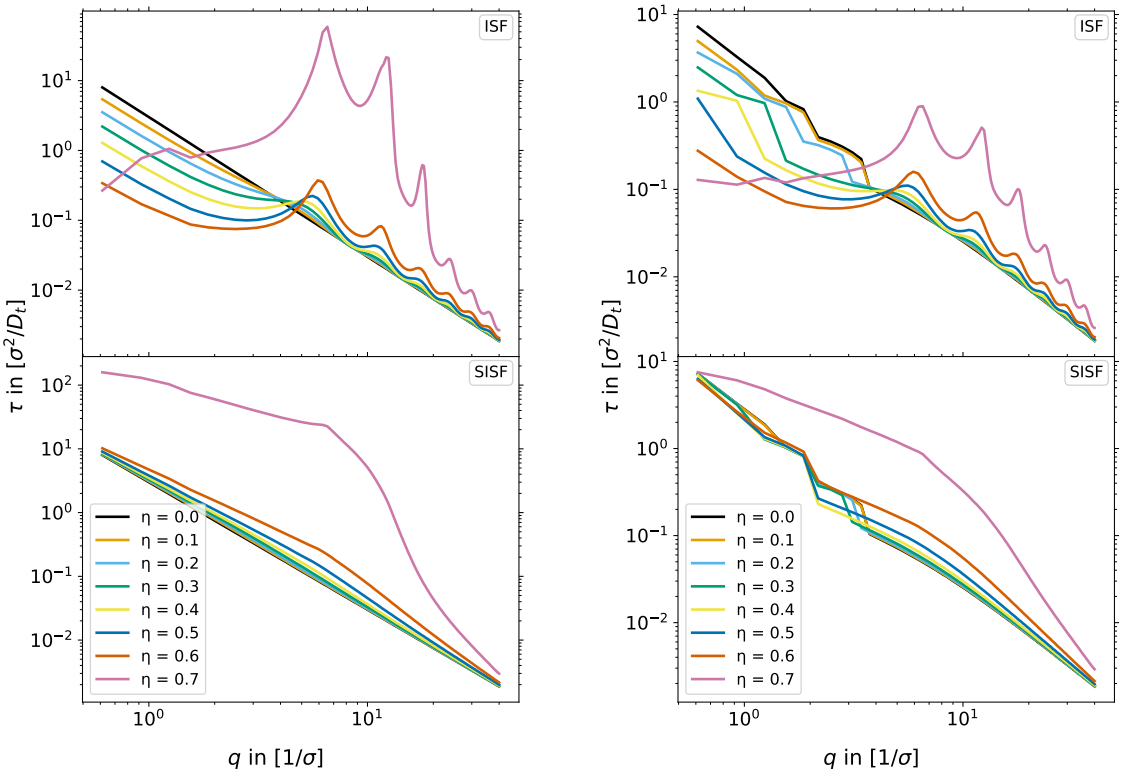

Figure 5.24: Relaxation time for the ISF and SISF as function of the wave vector q. The left figures illustrate a vanishing circle swimmer frequency, whereas the figures on the right illustrate the relaxation time for a finite frequency of $\nu = \nu^s = 5.0$. The other system parameters are given by the set $\{v = v^s = 5.0, D_r = D_r^s = 0.1\}$.

converging towards zero. A correlation function is considered as not relaxed, if the oscillations exceed the specified threshold. Two figures have been created. Figure (5.24) displays the relaxation time for varying wave numbers, while Figure (5.25) displays the relaxation time for varying packing fractions. First, varying wave numbers are considered. The effect of varying the wave number q is consistent with what has been observed previously for both the ISF and SISF. Specifically, larger wave numbers correspond to shorter correlation distances and, therefore, faster relaxation times. In addition, larger packing fractions, which correspond to higher densities, slow down the relaxation dynamics. Notably, there are some key differences between the ISF and SISF. Specifically, the SISF exhibits slightly faster relaxation times for small wave numbers that obey $\tau \sim 1/q^2$ for $q \to 0$ and the ISF displays profound oscillations that resemble the formation of cages, which are mathematically described by the oscillations of the static form factor. The ISF shows a behavior of $\tau \sim const$ for $q \to 0$. It should be noted that both figures are limited to the regime of low packing fractions below the critical packing fraction of $\eta_c = 0.7042$, which has been observed for passive Brownian particles in the numerical implementation employed here. The SISF graph exhibits an unequivocal upward trend of relaxation times with increasing densities, whereby higher q-values lead to smaller relaxation times. In contrast, the ISF graph demonstrates a distinct behavior that is related to the aforementioned oscillations of the static structure factor. A notable distinction arises between the behavior of the purely active system and the system of circle swimmers. Remarkably, the relaxation time of the ISF exhibits no significant disparity. The plot representing the finite rotational frequency does not exhibit an entirely monotonous decrease in relaxation time with increasing wave number.

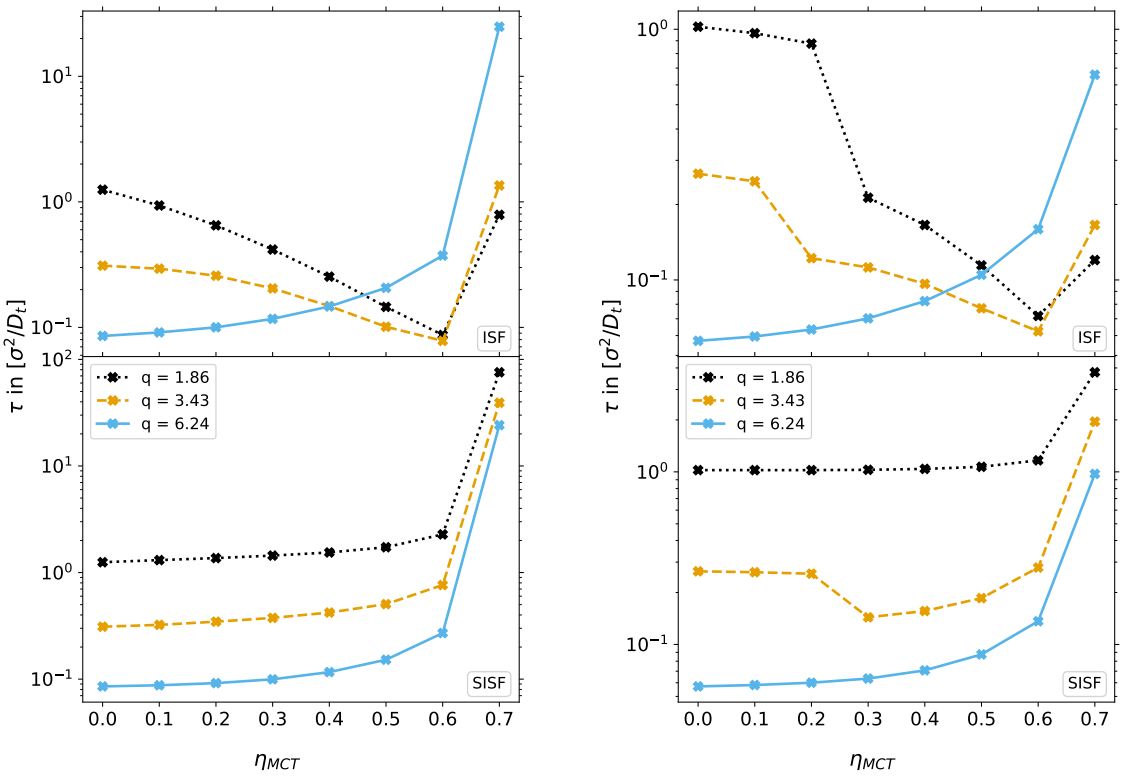

Figure 5.25: Relaxation time for the ISF and SISF as function of the packing fraction η. The left figures illustrate a vanishing circle swimmer frequency, whereas the figures on the right illustrate the relaxation time for a finite frequency of $\nu = \nu^s = 5.0$. The other system parameters are given by the set $\{v = v^s = 5.0, D_r = D_r^s = 0.1\}$.

While an overall decrease is evident, the plot displays intermittent jumps. This occurrence can be attributed to how the relaxation time is calculated: it is determined as the time value at which the ISF or SISF falls and remains below a threshold of 0.01, accounting for oscillations around zero. This calculation methodology entails certain inaccuracies, thus manifesting in the observed behavior. The SISF for a vanishing circle swimmer frequency likewise displays a similar feature, providing additional evidence supporting the argument that these maxima are a result of the relaxation time calculation itself rather than any inherent characteristic of the ISF or SISF. The figures depicted in Figure (5.25) also exhibit an upper bound of packing fractions that does not surpass the passive critical packing fraction. This discussion builds upon the previous one, emphasizing the crossing of lines and its association with the characteristic feature of the structure factor. As a general trend, elevating the packing fraction results in an exponential increase in the relaxation time. Furthermore, the divergence of the relaxation time in the vicinity of the glass transition becomes evident as well. The relaxation time depicted in Figure (5.26) is obtained by neglecting the influence of the memory kernel and solving the differential equation that arises from analytically setting the memory kernel to zero. This solution is known as the free particle solution, which was previously introduced, cf. Equation (2.49). When considering a truly free particle, that is, a particle characterized by a system with a negligible packing fraction, a remarkable agreement between the analytic solution and the MCT-numerics is observed, even for small wave numbers. As the packing fraction increases, the assumption of a free particle and hence the analytic free particle solution becomes less accurate leading to a deviation between the analytic and numerical solution. However, the plot shows that this difference is relatively small for larger wave numbers.

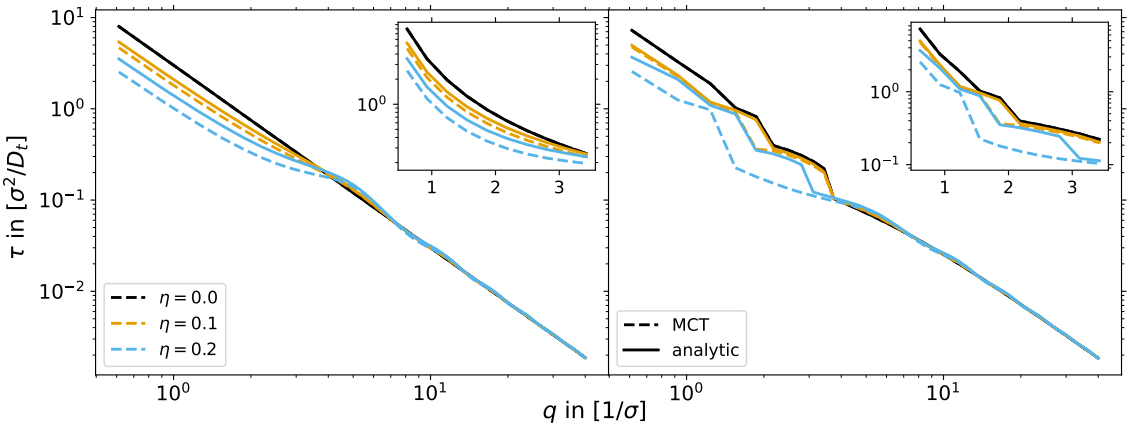

Figure 5.26: Comparison of the relaxation time of the MCT-numerics and the analytic solution of the MCT-equation, that is obtained by setting the memory kernel to zero, for varying η, and different wave numbers q. The left figure illustrates a vanishing circle swimmer frequency, whereas the figure on the right illustrates the relaxation time for a finite frequency of $\nu = \nu^s = 5.0$. The other system parameters are given by the set $\{v = v^s = 5.0, D_r = D_r^s = 0.1\}$.

Finally, Figure (5.27) compares the relaxation times obtained from MCT and ED-BD. An overall satisfactory agreement can be seen that is not more profound in some regions than in others, except for the highest density. It becomes apparent that the MCT-solution relaxes more slow than the ED-BD-solution does, especially prominent in the regime of a high packing fraction of $\eta = 0.7$. The reason for that is that no mapping for the swim velocity is used, resulting in the striking deviation of the relaxation time. This is interesting, because the relaxation time in the considered wave number regime demands the usage of an opposite mapping like the one conducted for the comparison of MCT and ED-BD data, in the regime of very small wave numbers, before.

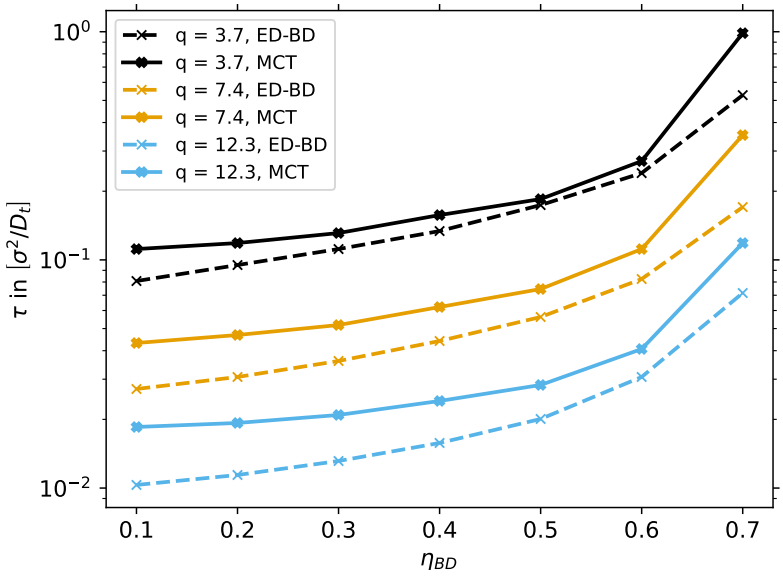

Figure 5.27: Comparison of the relaxation time of the MCT-numerics and the BD simulation. The set of system parameters is given by $\{v = v^s = 5.0, D_r = D_r^s = 0.1, \nu = \nu^s = 5.0\}$.

6. Summary and Perspective

In concluding this thesis, a summary of the attained results is warranted, followed by an overview of unresolved questions and areas that remain open for exploration.

Liluashvili [55] conducted an investigation into active Brownian particles by numerically solving the MCT-equation for such particles. This study delved into the impact of activity and the rotational diffusion constant on a glass-forming liquid. In a similar vein, Reichert [23–25] explored mixtures involving these particles. To be more precise, the investigation focused on a solitary passive or active Brownian particle existing within a medium composed of such particles. The primary emphasis of this research was also on the effects of activity and rotational diffusion. Additionally, ED-BD-simulations were conducted to provide validation for the effectiveness of MCT in addressing this non-equilibrium scenario. An open numerical challenge centered around the problematic cutoff required for a numerical implementation, particularly concerning the accuracy of the inverse translational frequency matrix. The current work addressed this issue by deriving an analytical expression for the matrix, which elucidated that prior studies performed adequately by inverting matrices of sufficient size.

By employing this novel analytical expression, and making use of lookup tables to speed up computation time, the paradigm of ABP was modified to encompass circle swimmers. These swimmers are essentially ABP possessing an intrinsic asymmetric form, resulting in circular motion characterized by an additional rotational term in the Langevin equation. A rationale was presented, contending that the circle swimmer frequency does not contribute to the vertices that is explained by the subsequent application of an orthogonal projection operator, mainly due to its proportionality to the density function. Consequently, it becomes evident that this characteristic influences the memory kernel exclusively through the rotational frequency matrix. The influence of the circle swimmer frequency follows a pattern akin to that of the rotational diffusion constant, a correspondence stemming from their shared units and their distinctive roles within the Péclet number. As both constants increase, they decrease the swim velocity's effectiveness in breaking neighboring confinements, consequently elongating relaxation times and ultimately driving a transition to a glassy state. The contribution of the rotational circle swimmer frequency introduces distinct oscillatory patterns in both the intermediate and self-intermediate scattering functions, particularly when examining wave numbers below a specific threshold. This threshold is inherently defined by the persistence length characteristic to such particles. In a broader context, it can be asserted that the dynamic characteristics of the relaxation process mirror those of ABP, albeit overlaid with oscillations within the effective diffusive regime. This resonance between behaviors was previously evident in the analytical expression for the MSD of a free particle. Here, the initial diffusive regime transitions into a ballistic phase after a certain period. This ballistic feature aligns with ABP-behavior. As time progresses beyond a certain limit, but remains within the ABP persistence time, a temporal window emerges, unveiling an oscillatory behavior. This phenomenon is elucidated by the circular motion of particles, which, due to this inherent motion, eventually return to their prior

positions.

Distinguishing characteristics emerge when comparing the ISF and SISF in relation to the circle swimmer frequency. Specifically, the ISF exhibits oscillatory behavior solely at lower densities, while the SISF displays this behavior across all packing fractions, excluding those proximate to the glass transition. This observation stems from the fundamental notion that individual particles are more likely to lack surrounding neighbors, thus affecting their circular motion. Furthermore, a distinction arises concerning relaxation times between the ISF and SISF. The SISF exhibits a faster, a monotonically decaying relaxation time with increasing wave numbers. Conversely, the ISF exhibits a distinct pattern, resembling that of the SISF yet overlaying oscillations akin to the static structure factor. Moreover, it becomes evident that, for the ISF, higher packing fractions lead to reduced relaxation times at very small wave numbers, a trend contrary to that seen in all other wave number regimes.

The comparison between MCT-data and ED-BD-data reveals a satisfactory level of agreement. However, a significant challenge in this comparison lays in the requirement to investigate the low wave number regime to observe the distinct oscillatory pattern generated by the circular motion of particles. As detailed in the corresponding section, this small wave number range poses a limitation. One primary factor contributing to the challenge is the dependence of the density mapping commonly employed in MCT on wave number. This mapping exhibited a noticeable discrepancy for small wave numbers only. Moreover, a heightened density demonstrates a less favorable agreement in comparison to the two lesser densities. Of paramount significance is the correlation between MCT and ED-BD in relation to the oscillatory phenomenon within the SISF attributed to the contribution of the circular swimmer. An aspect deserving enhancement pertains to a better equilibration of the ED-BD simulation, thereby facilitating a more comprehensive exploration of the glass transition region. Additionally, an improved temporal resolution within the simulation would lead to better depicted oscillations, a matter of considerable importance, particularly for small wave numbers, where the SISF oscillates more quickly. These aspects underscore that MCT serves as a valuable tool to elucidate specific effects such as the oscillatory behavior of correlation functions and mean-squared displacements, as well as to provide insights into the shapes of relaxation times and the overall parameter influences. However, the theory falls short in precisely determining the numerical values of these times and correlations due to the considerable data manipulation required to align the theoretical predictions with simulation data.

The MCT-equation has been successfully addressed within a domain characterized by minute wave numbers, hitherto unexplored. Within this realm, analogous to other wave number domains, numerical instabilities have materialized. Notably, an elevated swim velocity engenders numerical instability in the code, a challenge previously observed in the realm of active MCT at large [24, 55]. Furthermore, the presence of augmented rotational diffusion constants and rotational frequencies also cause instability. This instability extends to the plateaux of the ISF and SISF of a glass-forming liquid. These numerical perturbations transmute a constant function into a state of oscillation around the designated values, with these oscillations asymptotically spiraling towards infinity. The investigation of the effective swim velocity across a broader spectrum of densities remains a persisting puzzle, as does the exploration of motility-induced phase separation with the ITT-framework. The latter endeavor necessitates the scrutiny of higher swim velocities, a task complicated by the prevailing numerical issues. The analytical inversion of the frequency matrix has partially unshackled the predicament, unveiling that the inversion of adequately large matrices offers a robust approximation of the frequency matrix.

Symmetry-based reasoning posits the existence of an reformulated form for the memory kernel. One possessing a more auspicious configuration, replete with real values and assimilating the complex nature of the problem exclusively through sign functions. Indeed, an analytic formulation embodying such characteristics has been successfully devised. To achieve this, the customary bipolar integration was recalibrated, focusing on angles that align with the integration process. Regrettably, this novel configuration precludes the feasibility of precalculation via any type of lookup table, given its profound reliance on an extensive array of indices. Consequently, the computational program finds itself enmeshed in billions of function invocations, thereby engendering a computation duration of such magnitude that program finalization remains a difficult task. As such, the implementation remains an ongoing enigma. It warrants mention that numerical inaccuracies have manifested during the comparison of memory kernel values against their antecedent counterparts in prior code iterations. Resolution of this issue holds the potential to illuminate whether the segregation of imaginary components, thus circumventing the summation of minuscule imaginary values that ultimately yield finite contributions, augurs well for the ISF and SISF. Notably, the heretofore underestimated impact of swim velocity could potentially be attributable to this phenomenon. Conversely, it is plausible that this discrepancy may stem from an inherent systematic error within the MCT-theory framework, surfacing in the truncation of the ISF and SISF in relation to their angular indices. Conceivably, these indices should not have been truncated at such modest levels, thereby enabling higher modes of the correlation function to directly enter the MCT-equation. The reciprocal interaction with the memory kernel merely constitutes one facet of this complex equation. On the whole, the comparative analysis with Brownian dynamics data has demonstrated the necessity for swim velocity corrections, particularly within dense systems. Even the novel integration methodology may not, by itself, yield the projected benefit of heightened stability for augmented swim velocities.

A. Appendix

This appendix contains important calculations that are too extensive to be included in the main chapters of this thesis. To be not too tedious, the calculations presented here are concise but showcase all the essential steps.

The first section of this appendix concerns the computation of the inverse frequency matrix, which is achieved through an analytic calculation. This differs significantly from the previous frequency matrices. Reichert [23] previously derived a formula for the translational frequency matrix of a tagged particle using a numerically exact solution of a recursive relation. Here, the same formula is obtained by inverting a tridiagonal Laurent operator. The unperturbed matrix is defined as the tagged translational frequency matrix, and the deviation from the full translational frequency matrix is considered a perturbation. The Sherman-Morrison formula is then applied, yielding an exact formula that distinguishes itself from the low-q values of the inverse of a translational frequency matrix for large swim speeds.

The subsequent section of this appendix encompasses the rigorous proof of the novel integration scheme designed for active Brownian particles. It demonstrates that the angular integration exclusively yields real values, and introduces functions specifically crafted to account for potential sign changes arising from the multiplication of multiple imaginary units. With this, the derivation of the equations for ABP is resolved, bringing the section to a close.

Moving on to the third section, its primary focus is to provide a comprehensive description of the numerical implementation employed for these newly formulated equations. Notably, this implementation deviates slightly from previous numerical approaches, necessitating a detailed exposition to ensure clarity and accuracy.

A.1 Notes on the Inverse Frequency Matrix

To define the frequency matrix, the action of the adjoint Smoluchowski operator on a microscopic density function, with a subsequent application of a further density function, is considered. The matrix is formulated, in the most general form for mixtures of CABP, as

$$\begin{aligned}\omega_{ll'}^{\alpha\beta}(\boldsymbol{q}) &= -\left\langle \rho_l^{\alpha}(\boldsymbol{q})^* \Omega^{\dagger} \rho_{l'}^{\beta}(\boldsymbol{q}) \right\rangle \\ &= \delta_{\alpha\beta}\delta_{ll'}(D_t^{\alpha}q^2 + D_r^{\alpha}l^2 - \mathrm{i}\, l\nu^{\alpha}) - \mathrm{i}\,\delta_{\alpha\beta}\delta_{|l-l'|,1}\frac{qv^{\alpha}}{2}\,\mathrm{e}^{-\mathrm{i}(l-l')\theta_q}\, S_{ll}^{\alpha\beta}(q).\end{aligned} \tag{A.1}$$

In the MCT-equation, the inverse of the translational part of the frequency matrix is featured. As a result, it is necessary to present the translational part, which is defined by the corresponding adjoint translational Smoluchowski operator in the basis of microscopic density functions

$$\omega_{T,ll'}^{\alpha\beta}(\boldsymbol{q}) = -\left\langle \rho_l^{\alpha}(\boldsymbol{q})^* \Omega_T^{\dagger} \rho_{l'}^{\beta}(\boldsymbol{q}) \right\rangle = \delta_{\alpha\beta}\delta_{ll'} D_t^{\alpha} q^2 - \mathrm{i}\,\delta_{\alpha\beta}\delta_{|l-l'|,1}\frac{qv^{\alpha}}{2}\,\mathrm{e}^{-\mathrm{i}(l-l')\theta_q}\, S_{ll}^{\alpha\beta}(q). \tag{A.2}$$

To simplify the MCT-equation, the vector $\boldsymbol{q}$ can be aligned in the x-direction. This means that the angle between $\boldsymbol{q}$ and the x-axis, denoted by θ_q, is equal to zero, or $\theta_q = 0$. Consequently, the translational frequency matrix utilized in computations can be expressed in terms of the length q of the vector $\boldsymbol{q}$, and is given by the following expression

$$\omega^{\alpha\beta}_{T,ll'}(q) = \delta_{\alpha\beta}\delta_{ll'}D^{\alpha}_{t}q^2 - \mathrm{i}\,\delta_{\alpha\beta}\delta_{|l-l'|,1}\frac{qv^{\alpha}}{2}S^{\alpha\beta}_{ll}(q). \tag{A.3}$$

The translational frequency matrix can be written in a form that resembles a tridiagonal matrix. By letting $b = \delta_{\alpha\beta}D^{\alpha}_{t}q^2$ and $c = -\delta_{\alpha\beta}qv^{\alpha}$, the translational frequency matrix is expressed as

$$\omega_T(q) = \begin{pmatrix} \cdots & \cdots & \cdots & \cdots & \cdots & \cdots & \cdots \\ \cdots & \mathrm{i}\,c/2 & b & \mathrm{i}\,c/2 & 0 & 0 & \cdots \\ \cdots & 0 & \mathrm{i}\,c/2\ S^{\alpha\beta}(q) & b & \mathrm{i}\,c/2\ S^{\alpha\beta}(q) & 0 & \cdots \\ \cdots & 0 & 0 & \mathrm{i}\,c/2 & b & \mathrm{i}\,c/2 & \cdots \\ \cdots & \cdots & \cdots & \cdots & \cdots & \cdots & \cdots \end{pmatrix}. \tag{A.4}$$

This form of the matrix is utilized in all numerical calculations. Although the matrix in question is infinite-dimensional, numerical computations require a cutoff Λ_L to be set for the angular indices, such that $l \in [-\Lambda_L, \Lambda_L]$. However, a problem arises in determining this cutoff. Since taking a cutoff and inverting the matrix are non-commutative operations, the cutoff cannot be taken before inverting the matrix. If $S^{\alpha\beta}(q) \to 1$, then a tridiagonal matrix with equal values on each diagonal is obtained. More precisely, a matrix representation of a Laurent operator is acquired, which is known to be invertible. The calculation for the following scenario will be provided shortly. However, the primary concept of inverting the full translational frequency matrix must be introduced first.

If one notes that the translational frequency matrix with $S^{\alpha\beta}(q) \to 1$ equals the tagged translational frequency matrix, ω^{s}_{T}, its inverse $(\omega^{s}_{T})^{-1}$ can be calculated as the inverse of a Laurent operator [67]. The inverse of the entire matrix can be obtained by applying the Sherman-Morrison formula [66] to the matrix. To do so, one observes that the full matrix can be written as $\omega_T = \omega^{s}_{T} + \boldsymbol{u}\boldsymbol{v}^T$, where

$$u_0 = -\,\mathrm{i}\,\delta_{\alpha\beta}qv^{\alpha}/2(S^{\alpha\beta}(q)-1), \quad \boldsymbol{u}_l = \delta_{0l}u_0, \quad \boldsymbol{v}_l = \delta_{1l}+\delta_{-1l}, \quad (\boldsymbol{u}\boldsymbol{v}^T)_{ll'} = u_0\delta_{0l}(\delta_{1l'}+\delta_{-1l'}). \tag{A.5}$$

Alternatively, it can be written as

$$\boldsymbol{u} = (\cdots, 0, u_0, 0, \cdots)^T, \quad \boldsymbol{v} = (\cdots, 0, 0, 1, 0, 1, 0, 0, \cdots)^T, \tag{A.6}$$

which yields

$$\boldsymbol{u}\boldsymbol{v}^T = \begin{pmatrix} \cdots & \cdots & \cdots & \cdots & \cdots & \cdots & \cdots \\ \cdots & 0 & 0 & 0 & 0 & 0 & \cdots \\ \cdots & 0 & u_0 & 0 & u_0 & 0 & \cdots \\ \cdots & 0 & 0 & 0 & 0 & 0 & \cdots \\ \cdots & \cdots & \cdots & \cdots & \cdots & \cdots & \cdots \end{pmatrix}. \tag{A.7}$$

The Sherman-Morrison formula now yields

$$\begin{aligned} \omega^{-1}_{T,ll'} = (\omega^{s}_{T} + \boldsymbol{u}\boldsymbol{v}^T)^{-1}_{ll'} &= \left((\omega^{s}_{T})^{-1} - \frac{(\omega^{s}_{T})^{-1}\boldsymbol{u}\boldsymbol{v}^T(\omega^{s}_{T})^{-1}}{1+\boldsymbol{v}^T(\omega^{s}_{T})^{-1}\boldsymbol{u}}\right)_{ll'} \\ &= (\omega^{s}_{T})^{-1}_{ll'} - \frac{u_0(\omega^{s}_{T})^{-1}_{l0}((\omega^{s}_{T})^{-1}_{1l'} + (\omega^{s}_{T})^{-1}_{-1l'})}{1+u_0((\omega^{s}_{T})^{-1}_{10} + (\omega^{s}_{T})^{-1}_{-10})}, \end{aligned} \tag{A.8}$$

for the components of the inverse matrix. The components of the tagged inverse translational frequency matrix are denoted by $(\omega_T^s)^{-1}_{ll'} \equiv ((\omega_T^s)^{-1})_{ll'}$.

Now, the attention is turned to the calculation of the inverse of the tagged frequency matrix, which is a crucial component of the Sherman-Morrison formula. To this end, the calculation presented in Reference [72] is revisited, which begins by considering a tridiagonal Laurent matrix with complex coefficients α, β, and γ, given by

$$A = \begin{pmatrix} \cdots & \cdots & \cdots & \cdots & \cdots & \cdots & \cdots \\ \cdots & \alpha & \beta & \gamma & 0 & 0 & \cdots \\ \cdots & 0 & \alpha & \beta & \gamma & 0 & \cdots \\ \cdots & 0 & 0 & \alpha & \beta & \gamma & \cdots \\ \cdots & \cdots & \cdots & \cdots & \cdots & \cdots & \cdots \end{pmatrix}. \tag{A.9}$$

While this matrix is specified for the specific present case shortly, it is more illuminating to first work with the general matrix. A Laurent operator is invertible if and only if its symbol curve does not enclose zero. Here, the symbol curve is an ellipse $\{z \in \mathbb{T} | \frac{\alpha}{z} + \beta + \gamma z\}$. Therefore, A is invertible if $a(z) = \frac{\alpha}{z} + \beta + \gamma z \neq 0$. The formal definition of a Laurent operator can be phrased as follows. A bounded linear operator A on the space $L_2(\mathbb{Z})$ is a Laurent operator if and only if $\langle A\boldsymbol{e}_k, \boldsymbol{e}_j \rangle$ depends on the difference $j - k$ only, where $\{\boldsymbol{e}_j\}_{j=-\infty}^{\infty}$ is the standard orthonormal basis of $L_2(\mathbb{Z})$ [72]. To calculate the inverse,

$$\frac{1}{a(z)} = \frac{1}{\frac{\alpha}{z} + \beta + \gamma z} = \frac{z}{\alpha + \beta z + \gamma z^2} = \frac{z}{\gamma(\frac{\alpha}{\gamma} + \frac{\beta}{\gamma} z + z^2)} \tag{A.10}$$

is calculated at first. The fundamental theorem of algebra states that the denominator can be written as

$$\gamma(z - \lambda_+)(z - \lambda_-), \quad \text{where} \quad \lambda_\pm = -\frac{\beta}{2\gamma} \pm \sqrt{\left(\frac{\beta}{2\gamma}\right)^2 - \frac{\alpha}{\gamma}}. \tag{A.11}$$

It is worth noting that

$$\lambda_+ \lambda_- = \frac{\alpha}{\gamma}, \quad \lambda_+ + \lambda_- = -\frac{\beta}{\gamma}, \quad \text{and} \quad \lambda_+ - \lambda_- = 2\sqrt{\left(\frac{\beta}{2\gamma}\right)^2 - \frac{\alpha}{\gamma}}. \tag{A.12}$$

Motivated by the specific values of α, β, and γ in the present case, $\lambda_1 = \lambda_+$ and $\lambda_2 = \lambda_-$ is defined and it is assumed that $|\lambda_2| < |\lambda_1|$. The calculation proceeds as follows:

$$\begin{aligned} \frac{1}{a(z)} &= \frac{z}{\gamma(z - \lambda_+)(z - \lambda_-)} = \frac{z}{\gamma(\lambda_1 - \lambda_2)} \left(\frac{1}{z - \lambda_1} - \frac{1}{z - \lambda_2} \right) \\ &= \frac{z}{\gamma(\lambda_1 - \lambda_2)} \left(-\frac{1}{\lambda_1} \frac{1}{1 - \frac{z}{\lambda_1}} - \frac{1}{z} \frac{1}{1 - \frac{\lambda_2}{z}} \right) \\ &= \frac{z}{\gamma(\lambda_1 - \lambda_2)} \left(-\frac{1}{\lambda_1} \sum_{n=0}^{\infty} \left(\frac{z}{\lambda_1} \right)^n - \frac{1}{z} \sum_{n=0}^{\infty} \left(\frac{\lambda_2}{z} \right)^n \right) \\ &= \frac{1}{\gamma(\lambda_2 - \lambda_1)} \left(\sum_{n=1}^{\infty} \left(\frac{z}{\lambda_1} \right)^n + \sum_{n=0}^{\infty} \left(\frac{\lambda_2}{z} \right)^n \right). \end{aligned} \tag{A.13}$$

The present case requires that the coefficients of the tridiagonal Laurent matrix are defined as $\beta = D_t^\alpha q^2 = b$ and $\alpha = \gamma = -\mathrm{i}\, q v^\alpha / 2 = \mathrm{i}\, c/2$. The zeros of the matrix are given by

$$\lambda_\pm = \mathrm{i} \left(\frac{b}{c} \pm \sqrt{\frac{b^2}{c^2} + 1} \right). \tag{A.14}$$

The condition $|\lambda_2| < |\lambda_1|$ can be verified by defining $\lambda_1 = \lambda_+$ and $\lambda_2 = \lambda_-$. The prefactor of the equation can then be expressed as $1/(\gamma(\lambda_2 - \lambda_1)) = 1/\Delta$, where $\Delta = \sqrt{b^2 + c^2}$. Since $\alpha = \gamma$, one zero is the inverse of the other, i.e. $\lambda_+\lambda_- = 1$. By collecting the corresponding terms of the order of z, the inverse of the Laurent matrix can be computed

$$\begin{aligned} A^{-1}_{ll'} &= \delta_{ll'}\frac{1}{\Delta} + \frac{1}{\Delta}\sum_{n=1}^{\infty}\left(\delta_{l-l',-n}\left(\frac{1}{\lambda_+}\right)^n + \delta_{l-l',n}\lambda_-^n\right) \\ &= \delta_{ll'}\frac{1}{\Delta} + \frac{1}{\Delta}\sum_{n=1}^{\infty}\left(\delta_{l-l',-n}\left(\frac{1}{\lambda_+}\right)^n + \delta_{l-l',n}\left(\frac{1}{\lambda_+}\right)^n\right) \\ &= (-1)^{|l-l'|}\frac{(\mathrm{i}\,c)^{|l-l'|}}{\Delta(b+\Delta)^{|l-l'|}}. \end{aligned} \tag{A.15}$$

Consequently, the tagged inverse frequency matrix can be expressed as

$$(\omega^s_T)^{-1}_{ll'}(q) = \frac{(\mathrm{i}\,qv^\alpha)^{|l-l'|}}{\Delta(D^\alpha_t q^2 + \Delta)^{|l-l'|}}, \quad \Delta = \sqrt{(D^\alpha_t q^2)^2 + (qv^\alpha)^2}. \tag{A.16}$$

Subsequently, this result can be used to apply the Sherman-Morrison formula for the unperturbed matrix, thus yielding the final expression for the inverse translational frequency matrix. Although the latter lacks a simple form, it can be implemented by defining a function that computes the tagged translational frequency matrix using Equation (3.3), and then applies the Sherman-Morrison formula (3.4).

A.2 Proof of the Improved Integration Method

The proof commences by demonstrating that the integrals over the angle θ_k are real. To achieve this, Figure (2.6) is considered and an angle

$$\tilde{\theta}_p = 2\pi - \theta_p = \arctan\left(\frac{k\sin(\theta_k)}{q - k\cos(\theta_k)}\right) \tag{A.17}$$

is introduced. From either the equation or the diagram, it can be deduced that the angle can be treated as a function $\tilde{\theta}_p(q, k, \theta_k)$ possessing two points of inflection symmetry. One occurs at $\theta_k = 0$, yielding $\tilde{\theta}_p(\theta_k) = -\tilde{\theta}_p(-\theta_k)$, while the other arises at $\theta_k = \pi$, resulting in $\tilde{\theta}_p(\pi + \theta_k) = \tilde{\theta}_p(\theta_k - \pi) = -\tilde{\theta}_p(\pi - \theta_k)$. The domain of integration spans $[0, 2\pi]$. The strategy entails dividing this domain into four quadrants and mapping each quadrant back to the interval $[0, \pi/2]$ using the following substitutions (in sequence): $\theta_k \mapsto \theta_k, \pi - \theta_k, \theta_k - \pi, 2\pi - \theta_k$. Introducing m and n as integers and combining all prefactors into a function $\chi(\theta_k)$, the integral reads

$$\begin{aligned} &\int_0^{2\pi} \mathrm{d}\theta_k \chi(\theta_k)\,\mathrm{e}^{-\mathrm{i}\,m\theta_k}\,\mathrm{e}^{\mathrm{i}\,n\tilde{\theta}_p(\theta_k)} \\ &= \int_0^{\pi/2} \mathrm{d}\theta_k \chi(\theta_k)\,\mathrm{e}^{-\mathrm{i}\,m\theta_k}\,\mathrm{e}^{\mathrm{i}\,n\tilde{\theta}_p(\theta_k)} + \int_0^{\pi/2} \mathrm{d}\theta_k \chi(\pi-\theta_k)(-1)^m\,\mathrm{e}^{\mathrm{i}\,m\theta_k}\,\mathrm{e}^{\mathrm{i}\,n\tilde{\theta}_p(\pi-\theta_k)} \\ &+ \int_0^{\pi/2} \mathrm{d}\theta_k \chi(\theta_k-\pi)(-1)^m\,\mathrm{e}^{-\mathrm{i}\,m\theta_k}\,\mathrm{e}^{\mathrm{i}\,n\tilde{\theta}_p(\theta_k-\pi)} + \int_0^{\pi/2} \mathrm{d}\theta_k \chi(2\pi-\theta_k)\,\mathrm{e}^{\mathrm{i}\,m\theta_k}\,\mathrm{e}^{\mathrm{i}\,n\tilde{\theta}_p(2\pi-\theta_k)} \\ &= \int_0^{\pi/2} \mathrm{d}\theta_k \chi(\theta_k)\,\mathrm{e}^{-\mathrm{i}\,m\theta_k}\,\mathrm{e}^{\mathrm{i}\,n\tilde{\theta}_p(\theta_k)} + \int_0^{\pi/2} \mathrm{d}\theta_k \chi(\pi-\theta_k)(-1)^m\,\mathrm{e}^{\mathrm{i}\,m\theta_k}\,\mathrm{e}^{-\mathrm{i}\,n\tilde{\theta}_p(\pi+\theta_k)} \\ &+ \int_0^{\pi/2} \mathrm{d}\theta_k \chi(\pi-\theta_k)(-1)^m\,\mathrm{e}^{-\mathrm{i}\,m\theta_k}\,\mathrm{e}^{\mathrm{i}\,n\tilde{\theta}_p(\pi+\theta_k)} + \int_0^{\pi/2} \mathrm{d}\theta_k \chi(\theta_k)\,\mathrm{e}^{\mathrm{i}\,m\theta_k}\,\mathrm{e}^{-\mathrm{i}\,n\tilde{\theta}_p(\theta_k)} \\ &= 2\times\int_0^{\pi/2} \mathrm{d}\theta_k\Big(\chi(\theta_k)\cos\Big(m\theta_k - n\tilde{\theta}_p(\theta_k)\Big) + (-1)^m\chi(\pi-\theta_k)\cos\Big(m\theta_k - n\tilde{\theta}_p(\pi+\theta_k)\Big)\Big) \end{aligned}$$

$$
\begin{aligned}
&= 2 \times \Bigg(\int_0^{\pi/2} \mathrm{d}\theta_k \chi(\theta_k) \cos\Big(m\theta_k - n\tilde{\theta}_p(\theta_k)\Big) \\
&\quad + (-1)^m \int_{\pi/2}^{\pi} \mathrm{d}\theta_k \chi(\theta_k) \cos\Big(m(\pi - \theta_k) + n\tilde{\theta}_p(\theta_k)\Big)\Bigg)
\end{aligned}
\tag{A.18}
$$

This particular expression finds utility in the program's implementation as it renders the utilization of the phase terms I_A, I_B, I_C redundant. The function $\chi(\theta_k) = \chi(p(\theta_k))$ is actually a function of the wave number $p(\theta_k)$, that itself is a function of the angle θ_k. The wave number is defined as

$$p = \sqrt{q^2 + k^2 - 2qk\cos(\theta_k)}. \tag{A.19}$$

The angle enters that term only as the argument of the cosine. Therefore, the identities

$$\chi(\theta_k) = \chi(2\pi - \theta_k) \quad \text{and} \quad \chi(\pi - \theta_k) = \chi(\theta_k - \pi), \tag{A.20}$$

hold. The last step makes use of a further substitution $\theta_k \mapsto \pi - \theta_k$. This substitution is essential for the numerical implementation, since the function $\chi(\theta_k)$ is only available for those wave numbers resolved by the underlying grid.

The subsequent step involves an examination of the imaginary units that are introduced into the equation by the ISF through a redefinition

$$
\begin{aligned}
\hat{\Phi}_{ll'}(q,t) &= \mathrm{Re}(\Phi_{ll'}(q,t)) + \mathrm{Im}(\Phi_{ll'}(q,t)), \\
\Phi_{ll'}(q,t) &= \mathrm{i}^{|(l-l')\mathrm{mod}2|}\, \hat{\Phi}_{ll'}(q,t).
\end{aligned}
\tag{A.21}
$$

Initially, there exists the multiplicative factor

$$\mathrm{i}^{|(l_1-l_3)\mathrm{mod}2|}\, \mathrm{i}^{|(l_2-l_4)\mathrm{mod}2|}\, \hat{\Phi}_{l_1 l_3}(k,t) \hat{\Phi}_{l_2 l_4}(p,t), \tag{A.22}$$

which occupies the prominent position in front of everything. The friction kernel's expression in total can be divided into various additive components. The right vertex possesses an imaginary part of null value, thereby also serving as a multiplicative factor. The left vertex can be separated into its real equilibrium component and the non-equilibrium component. An individual imaginary unit is present in front of the latter. Furthermore, it can be further subdivided into three principal segments. This further subdivision is of no importance for the present discussion, since the potential exponential terms have been assimilated into the integrals over θ_k, thereby contributing a real value. Two distinct scenarios necessitate examination. The term

$$\delta_{l_1+l_2,l}\delta_{l_3+l_4,l'}\, \mathrm{i}^{|(l_1-l_3)\mathrm{mod}2|}\, \mathrm{i}^{|(l_2-l_4)\mathrm{mod}2|} \tag{A.23}$$

ought to yield, barring any potential sign discrepancies, the alternating expression $\mathrm{i}^{|(l-l')\mathrm{mod}2|}$ since it corresponds to the combination of the right vertex and the equilibrium part of the left vertex. The prefactor can be inferred from the ensuing table, wherein the values for l and l' have been derived from the Kronecker deltas $\delta_{l_1+l_2,l}, \delta_{l_3+l_4,l'}$. The shaded rows denote instances where a disparity between the term and the desired outcome arises.

l_1	l_2	l_3	l_4	l	l'	$\mathrm{i}^{\lvert(l_1-l_3)\mathrm{mod}2\rvert}\,\mathrm{i}^{\lvert(l_2-l_4)\mathrm{mod}2\rvert}$	$\mathrm{i}^{\lvert(l-l')\mathrm{mod}2\rvert}$
even	even	even	even	even	even	$1 \cdot 1 = 1$	1
even	even	even	odd	even	odd	$1 \cdot i = i$	i
even	even	odd	even	even	odd	$i \cdot 1 = i$	i
even	even	odd	odd	even	even	$i \cdot i = -1$	1
even	odd	even	even	odd	even	$1 \cdot i = i$	i
even	odd	even	odd	odd	odd	$1 \cdot 1 = 1$	1
even	odd	odd	even	odd	odd	$i \cdot i = -1$	1
even	odd	odd	odd	odd	even	$i \cdot 1 = i$	i
odd	even	even	even	odd	even	$i \cdot 1 = i$	i
odd	even	even	odd	odd	odd	$i \cdot i = -1$	1
odd	even	odd	even	odd	odd	$1 \cdot 1 = 1$	1
odd	even	odd	odd	odd	even	$1 \cdot i = i$	i
odd	odd	even	even	even	even	$i \cdot i = -1$	1
odd	odd	even	odd	even	odd	$i \cdot 1 = i$	i
odd	odd	odd	even	even	odd	$1 \cdot i = i$	i
odd	odd	odd	odd	even	even	$1 \cdot 1 = 1$	1

The disparity between them is solely characterized by a negative symbol. Therefore, the function ought to produce a negative sign when both $l_1 - l_3$ and $l_2 - l_4$ are odd. This can be visually represented in the following table:

$l_1 - l_3$	$l_2 - l_4$	$s^a_\pm$
even	even	1
even	odd	1
odd	even	1
odd	odd	-1

An expression that exhibits such alternating behavior can be defined as follows

$$s^a_\pm = (-1)^{(l_1-l_3)(l_2-l_4)}. \tag{A.24}$$

Moving on to the second scenario, it encompasses the terms generated by the multiplication with the non-equilibrium component of the left vertex, accompanied by a prefactor of

$$\delta_{|l-l_1-l_2|,1}\delta_{l_3+l_4,l'}\,\mathrm{i} \times \mathrm{i}^{\lvert(l_1-l_3)\mathrm{mod}2\rvert}\,\mathrm{i}^{\lvert(l_2-l_4)\mathrm{mod}2\rvert}, \tag{A.25}$$

which introduces an additional imaginary unit and involves a distinct Kronecker delta. The procedure mirrors the one described earlier. A table is constructed to assess how this expression deviates from the desired form $\mathrm{i}^{\lvert(l-l')\mathrm{mod}2\rvert}$. The table can be depicted as follows:

l_1	l_2	l_3	l_4	l	l'	$\mathrm{i}\cdot\mathrm{i}^{\lvert(l_1-l_3)\mathrm{mod}2\rvert}\,\mathrm{i}^{\lvert(l_2-l_4)\mathrm{mod}2\rvert}$	$\mathrm{i}^{\lvert(l-l')\mathrm{mod}2\rvert}$
even	even	even	even	odd	even	$i\cdot 1\cdot 1=i$	i
even	even	even	odd	odd	odd	$i\cdot 1\cdot i=-1$	1
even	even	odd	even	odd	odd	$i\cdot i\cdot 1=-1$	1
even	even	odd	odd	odd	even	$i\cdot i\cdot i=-i$	i
even	odd	even	even	even	even	$i\cdot 1\cdot i=-1$	1
even	odd	even	odd	even	odd	$i\cdot 1\cdot 1=i$	i
even	odd	odd	even	even	odd	$i\cdot i\cdot i=-i$	i
even	odd	odd	odd	even	even	$i\cdot i\cdot 1=-1$	1
odd	even	even	even	even	even	$i\cdot i\cdot 1=-1$	1
odd	even	even	odd	even	odd	$i\cdot i\cdot i=-i$	i
odd	even	odd	even	even	odd	$i\cdot 1\cdot 1=i$	i
odd	even	odd	odd	even	even	$i\cdot 1\cdot i=-1$	1
odd	odd	even	even	odd	even	$i\cdot i\cdot i=-i$	i
odd	odd	even	odd	odd	odd	$i\cdot i\cdot 1=-1$	1
odd	odd	odd	even	odd	odd	$i\cdot 1\cdot i=-1$	1
odd	odd	odd	odd	odd	even	$i\cdot 1\cdot 1=i$	i

In this context, the attention should be directed towards the rows that produce the desired outcome. These rows are attained when $l_1 - l_3$ and $l_2 - l_4$ are both even. Consequently, all other rows necessitate correction by means of a negative sign, while these particular rows do not. This logical reasoning can be elucidated through the following chart:

$l_1 - l_3$	$l_2 - l_4$	$s^b_\pm$
even	even	1
even	odd	-1
odd	even	-1
odd	odd	-1

An expression that exemplifies such alternating behavior can be expressed as follows

$$s^b_\pm = (-1)^{(l_1-l_3)+(l_2-l_4)} \times (-1)^{(l_1-l_3)(l_2-l_4)}. \tag{A.26}$$

By employing these alternating functions $s^a_\pm$, the components that are integrated into the equation of the friction kernel are successfully defined.

Finally, the attention is turned towards the exploration of tagged active Brownian particles, specifically focusing on the self-intermediate scattering function. The angular integration process remains consistent with that of the friction kernel for the ISF, obviating the need for repetition. However, it is necessary to investigate potential sign changes that differ from those discussed in the context of the ISF. This arises due to the distinct structure of the friction kernel for the SISF. Nonetheless, the overall prefactor should again be $\mathrm{i}^{\lvert(l-l')\mathrm{mod}2\rvert}$. Two distinct cases warrant examination: the first pertains to the term generated by the equilibrium part of the vertex, while the second concerns the non-equilibrium part.

The equilibrium part incorporates two Kronecker deltas, δ_{ll_2} and δ_{l_10}. It is imperative to verify any potential sign changes that may arise from the term

$$\delta_{ll_2}\delta_{l_10}\,\mathrm{i}^{\lvert l_1\mathrm{mod}2\rvert}\,\mathrm{i}^{\lvert(l_2-l')\mathrm{mod}2\rvert} = \mathrm{i}^{\lvert(l-l')\mathrm{mod}2\rvert}. \tag{A.27}$$

It is revealed that no sign changes occur, and the term evaluates to the desired form due to the presence of the Kronecker deltas.

The second case, pertaining to the non-equilibrium part, is more intricate as it imposes no restrictions on the angular index l'. The term, which should yield $\mathrm{i}^{|(l-l')\mathrm{mod}2|}$ up to an as-yet-determined prefactor, is as follows

$$\delta_{|l-l_1-l_2|,1}\,\mathrm{i}\times\mathrm{i}^{|l_1\mathrm{mod}2|}\,\mathrm{i}^{|(l_2-l')\mathrm{mod}2|}\,. \tag{A.28}$$

A tabular representation of the term can be organized as follows:

l_1	l_2	l	l'	$\mathrm{i}\cdot\mathrm{i}^{\lvert l_1\mathrm{mod}2\rvert}\,\mathrm{i}^{\lvert(l_2-l')\mathrm{mod}2\rvert}$	$\mathrm{i}^{\lvert(l-l')\mathrm{mod}2\rvert}$
even	even	odd	even $\vee$ odd	$i\cdot 1\cdot(1\vee i)=\boxed{i}\vee -1$	$\boxed{i}\vee 1$
even	odd	even	even $\vee$ odd	$i\cdot 1\cdot(i\vee 1)=-1\vee\boxed{i}$	$1\vee\boxed{i}$
odd	even	even	even $\vee$ odd	$i\cdot i\cdot(1\vee i)=-1\vee -i$	$1\vee i$
odd	odd	odd	even $\vee$ odd	$i\cdot i\cdot(i\vee 1)=-i\vee -1$	$i\vee 1$

Highlighted within the boxed entries are the combinations that yield the correct prefactor. All other entries necessitate correction through multiplication by a factor of minus one. The alternating function

$$\begin{aligned} s_\pm &= (1-|l'\mathrm{mod}2|)s^a_\pm + |l'\mathrm{mod}2|s^b_\pm,\\ s^a_\pm &= (-1)^{l_1+l_2}(-1)^{l_1 l_2},\\ s^b_\pm &= (-1)^{l_1+l}(-1)^{l_1 l}, \end{aligned} \tag{A.29}$$

captures this alternating behavior. With this, the proof of the formulas presented in Chapter (3) is completed.

A.3 Notes on the Improved Numerical Implementation

The numerical implementation of the modified integration scheme for active Brownian particles involves tracking the multiplication of matrices of the form

$$\hat{A}_{ll'} = \mathrm{Re}\,A_{ll'} + \mathrm{Im}\,A_{ll'}, \quad A_{ll'} = \mathrm{i}^{|(l-l')\mathrm{mod}2|}\,\hat{A}_{ll'}. \tag{A.30}$$

This particular splitting yields some caution when multiplying two complex matrices, denoted as A and B. The multiplication can be expressed as

$$A_{lj}B_{jl'} = \mathrm{i}^{|(l-j)\mathrm{mod}2|}\,\mathrm{i}^{|(j-l')\mathrm{mod}2|}\,\hat{A}_{lj}\hat{B}_{jl'} = s_\pm\,\mathrm{i}^{|(l-l')\mathrm{mod}2|}\,\hat{A}_{lj}\hat{B}_{jl'}. \tag{A.31}$$

To accomplish this, the function

$$s_\pm = (-1)^{(l-j)(j-l')}, \tag{A.32}$$

is utilized to manage possible minus signs. To validate this function, a table is constructed to assess how the prefactor deviates from the desired form $\mathrm{i}^{|(l-l')\mathrm{mod}2|}$. The table can be presented as follows:

l	j	l'	$\mathrm{i}^{\lvert(l-j)\mathrm{mod}2\rvert}\,\mathrm{i}^{\lvert(j-l')\mathrm{mod}2\rvert}$	$\mathrm{i}^{\lvert(l-l')\mathrm{mod}2\rvert}$
even	even	even	$1\cdot 1=1$	1
even	even	odd	$1\cdot i=i$	i
even	odd	even	$i\cdot i=-1$	1
even	odd	odd	$i\cdot 1=i$	i
odd	even	even	$i\cdot 1=i$	i
odd	even	odd	$i\cdot i=-1$	1
odd	odd	even	$1\cdot i=i$	i
odd	odd	odd	$1\cdot 1=1$	1

Within this context, it is crucial to focus on the rows that produce the incorrect outcome. Such occurrences arise when both $l - j$ and $j - l'$ are odd. The necessary correction is made by leveraging the alternating function $s_{\pm}$ mentioned earlier, which can be clarified using the following chart:

$l - j$	$j - l$	$s_{\pm}$
even	even	1
even	odd	1
odd	even	1
odd	odd	-1

Bibliography

[1] R. Brown. A Brief Account of Microscopical Observations on the Particles contained in the Pollen of Plants and on the General Existence of Active Molecules in Organic and Inorganic Bodies. *Cambridge University Press* **1**(1), 463–486, (1866).

[2] S. Ramaswamy. The Mechanics and Statistics of Active Matter. *Annual Review of Condensed Matter Physics* **1**(1), 323–345, (2010).

[3] S. van Teeffelen and H. Löwen. Dynamics of a Brownian circle swimmer. *Phys. Rev. E* **78**(2), 020101, (2008).

[4] F. Toschi and M. Sega. Flowing Matter. *Springer Cham*, 1st ed., 211–238, (2019).

[5] C. Kurzthaler, S. Leitmann and T. Franosch. Intermediate scattering function of an anisotropic active Brownian particle. *Sci. Rep.* **6**(1), 36702, (2016).

[6] C. Kurzthaler and T. Franosch. Intermediate scattering function of an anisotropic Brownian circle swimmer. *Soft Matter* **13**(37), 6396–6406, (2016).

[7] T. Minamino, K. Imada and K. Namba. Molecular motors of the bacterial flagella. *Current Opinion in Structural Biology* **18**(6), 693–701, (2008).

[8] H.C. Berg. E. coli in Motion. *Springer New York*, 1st ed., (2004).

[9] J. Elgeti, R.G. Winkler and G. Gompper. Physics of microswimmers - single particle motion and collective behavior: a review. *Rep. Prog. Phys.* **78**(5), 056601, (2015).

[10] B. Fabry et al. Scaling the Microrheology of Living Cells. *Phys. Rev. Lett.* **87**(14), (2001).

[11] H.C. Barshilia et al. Depolarized light scattering spectroscopy of $Ca_{0.4}K_{0.6}(NO_3)_{1.4}$: A reexamination of the "knee". *Phys. Rev. E* **59**(5), 5625–5628, (1999).

[12] U. Schneider et al. Broadband dielectric spectroscopy on glass-forming propylene carbonate. *Phys. Rev. E* **59**(6), 6924–6936, (1999).

[13] W. Götze and T. Voigtmann. Universal and nonuniversal features of glassy relaxation in propylene carbonate. *Phys. Rev. E* **61**(4), 4133–4147, (2000).

[14] G. Li et al. Light-scattering investigation of α and β relaxation near the liquid-glass transition of the molecular glass Salol. *Phys. Rev. A* **46**(6), 3343–3356, (1992).

[15] W. van Megen and S.M. Underwood. Glass transition in colloidal hard spheres: Mode-coupling theory analysis. *Phys. Rev. Lett.* **70**(18), 2766–2769, (1993).

[16] W. van Megen and S.M. Underwood. Glass transition in colloidal hard spheres: Measurement and mode-coupling-theory analysis of the coherent intermediate scattering function. *Phys. Rev. E* **49**(5), 4206–4220, (1994).

[17] J. Wuttke et al. Neutron and light scattering study of supercooled glycerol. *Phys. Rev. Lett.* **72**(19), 3052–3055, (1994).

[18] Y. Yang and K.A. Nelson. T_c of the Mode Coupling Theory Evaluated from Impulsive Stimulated Light Scattering on Salol. *Phys. Rev. Lett.* **74**(24), 4883–4886, (1995).

[19] H.Z. Cummins et al. Light Scattering Spectroscopy of Orthoterphenyl: Idealized and Extended Mode Coupling Analysis. *Progress of Theoretical Physics Supplement* **126**(1), 21–34, (1997).

[20] A.P. Singh et al. Structural relaxation in orthoterphenyl: a schematic mode-coupling-theory model analysis. *Journal of Non-Crystalline Solids* **235-237**(1), 66–70, (1998).

[21] P. Lunkenheimer et al. Fast Dynamics of Glass-Forming Glycerol Studied by Dielectric Spectroscopy. *Phys. Rev. Lett.* **77**(2), 318–321, (1996).

[22] T. Voigtmann and J. Horbach. Slow dynamics in ion-conducting sodium silicate melts: Simulation and mode-coupling theory. *Europhysics Letters* **74**(3), 459, (2006).

[23] J. Reichert, S. Mandal and T. Voigtmann. Mode-coupling theory for tagged-particle motion of active Brownian particles. *Phys. Rev. E* **104**(4), 044608, (2021).

[24] J. Reichert and T. Voigtmann. Tracer dynamics in crowded active-particle suspensions. *Soft Matter* **17**(46), 10492–10504, (2021).

[25] J. Reichert, L.F. Granz and T. Voigtmann. Transport coefficients in dense active Brownian particle systems: mode-coupling theory and simulation results. *Eur. Phys. J. E* **44**(3), 27, (2021).

[26] W. Kob and H.C. Andersen. Scaling Behavior in the β-Relaxation Regime of a Supercooled Lennard-Jones Mixture. *Phys. Rev. Lett.* **73**(10), 1376–1379, (1994).

[27] W. Kob and H.C. Andersen. Testing mode-coupling theory for a supercooled binary Lennard-Jones mixture I: The van Hove correlation function. *Phys. Rev. E* **51**(5), 4626–4641, (1995).

[28] F. Sciortino et al. Supercooled water and the kinetic glass transition. *Phys. Rev. E* **54**(6), 6331–6343, (1996).

[29] F. Sciortino et al. Supercooled water and the kinetic glass transition. II. Collective dynamics. *Phys. Rev. E* **56**(5), 5397–5404, (1997).

[30] F. Sciortino and W. Kob. Debye-Waller Factor of Liquid Silica: Theory and Simulation. *Phys. Rev. Lett.* **86**(4), 648–651, (2001).

[31] J. Horbach, W. Kob and K. Binder. Molecular dynamics simulation of the dynamics of supercooled silica. *Philosophical Magazine B* **77**(2), 297–303, (1998).

[32] P. Gallo et al. Slow Dynamics of Water Molecules in Supercooled States. *Phys. Rev. Lett.* **76**(15), 2730–2733, (1996).

[33] S.K. Das, J. Horbach and T. Voigtmann. Structural relaxation in a binary metallic melt: Molecular dynamics computer simulation of undercooled $Al_{80}Ni_{20}$. *Phys. Rev. B* **78**(6), 064208, (2008).

[34] E. Lauga et al. Swimming in circles: motion of bacteria near solid boundaries. *Biophys J.* **90**(2), 400–12, (2006).

[35] B.M. Friedrich and F. Jülicher. Steering Chiral Swimmers along Noisy Helical Paths. *Phys. Rev. Lett.* **103**(6), 068102, (2009).

[36] F. Kümmel et al. Circular Motion of Asymmetric Self-Propelling Particles. *Phys. Rev. Lett.* **110**(19), 198302, (2013).

[37] N.H.P. Nguyen et al. Emergent Collective Phenomena in a Mixture of Hard Shapes through Active Rotation. *Phys. Rev. Lett.* **112**(7), 075701, (2014).

[38] R. Matas-Navarro et al. Hydrodynamic suppression of phase separation in active suspensions. *Phys. Rev. E* **90**(3), 032304, (2014).

[39] Y. Goto and H. Tanaka. Purely hydrodynamic ordering of rotating disks at a finite Reynolds number. *Nature Communications* **6**(1), 5994, (2015).

[40] K. Yeo, E. Lushi and P.M. Vlahovska. Collective Dynamics in a Binary Mixture of Hydrodynamically Coupled Microrotors. *Phys. Rev. Lett.* **114**(18), 188301, (2015).

[41] G.J. Liao, C.K. Hall and S.H.L. Klapp. Dynamical self-assembly of dipolar active Brownian particles in two dimensions. *Soft Matter* **16**(9), 2208–2223, (2020).

[42] G.M. Whitesides and B. Grzybowski. Self-assembly at all scales. *Science* **295**(5564), 2418–21, (2002).

[43] G. Kokot et al. Emergence of reconfigurable wires and spinners via dynamic self-assembly. *PNAS* **5**(9528), 1–8, (2015).

[44] G. Kokot et al. Active turbulence in a gas of self-assembled spinners. *PNAS* **114**(49), 12870–12875, (2017).

[45] W. Yan and J.F. Brady. The swim force as a body force. *Soft Matter* **11**(31), 6235–6244, (2015).

[46] H. Löwen. Inertial effects of self-propelled particles: From active Brownian to active Langevin motion. *The Journal of Chemical Physics* **152**(4), 040901, (2020).

[47] A.R. Sprenger et al. Dynamics of active particles with translational and rotational inertia. *J. Phys.: Condens. Matter* **35**(1-12), 305101, (2020).

[48] K. Ito. On stochastic differential equations. *Memoirs of the American Mathematical Society* **4**(1), 51, (1951).

[49] A.D. Fokker. Die mittlere Energie rotierender elektrischer Dipole im Strahlungsfeld. *Annalen der Physik* **348**(5), 810–820, (1914).

[50] M. Planck. Sitzungsberichte der Preussischen Akademie der Wissenschaften zu Berlin. *Preussische Akademie der Wissenschaften* **1**(1), 324–341, (1917).

[51] L.M.C. Janssen. Mode-coupling theory of the glass transition: A primer. *Frontiers in Physics* **6**(97), 1–18, (2018).

[52] R. Zwanzig. Nonequilibrium Statistical Mechanics. *Oxford University Press*, (2001).

[53] G. Szamel and H. Löwen. Mode-coupling theory of the glass transition in colloidal systems. *Phys. Rev. A* **44**(12), 8215–8219, (1991).

[54] W. Götze. Complex Dynamics of Glass-Forming Liquids: A Mode-Coupling Theory. *Oxford University Press*, 1st ed., 1–576, (2008).

[55] A. Liluashvili, J. Onody and T. Voigtmann. Mode-coupling theory for active Brownian particles. *Phys. Rev. E* **96**(6), 062608, (2017).

[56] J.P. Hansen and I.R. McDonald. Theory of Simple Liquids. *Academic Press*, 4th ed., 1–147, (2013).

[57] A. Einstein. Über die von der molekularkinetischen Theorie der Wärme geforderte Bewegung von in ruhenden Flüssigkeiten suspendierten Teilchen. *Ann. Phys.* **332**(8), 549–560, (1905).

[58] A. Azizi and P.G. Yazdi. White Noise: Applications and Mathematical Modeling. *Springer Singapore*, 1st ed., 25–36, (2019).

[59] R. Kubo. The fluctuation-dissipation theorem. *Rep. Prog. Phys.* **29**(1), 255, (1966).

[60] A.L. Thorneywork et al. Structure factors in a two-dimensional binary colloidal hard sphere system. *Molecular Physics* **116**(21-22), 3245–3257, (2018).

[61] S. Ciarella et al. Multi-component generalized mode-coupling theory: predicting dynamics from structure in glassy mixtures. *Eur. Phys. J. E* **44**(91), (2021).

[62] W. Kob et al. Slow Relaxations and Nonequilibrium Dynamics in Condensed Matter. *Springer Berlin, Heidelberg*, 1st ed., 199–269, (2002).

[63] W. Götze. Recent tests of the mode-coupling theory for glassy dynamics. *Journal of Physics: Condensed Matter* **11**(10A), A1, (1999).

[64] G. Biroli et al. Inhomogeneous Mode-Coupling Theory and Growing Dynamic Length in Supercooled Liquids. *Phys. Rev. Lett.* **97**(19), 195701, (2006).

[65] A. Ben-Naim. The Kirkwood Superposition Approximation, Revisited and reexamined. *JOURNAL OF ADVANCES IN CHEMISTRY* **1**(1), 27–35, (2013).

[66] M. S. Bartlett. An Inverse Matrix Adjustment Arising in Discriminant Analysis. *The Annals of Mathematical Statistics* **22**(1), 107–111, (1951).

[67] A.E. Frazho and W. Bhosri. Toeplitz and Laurent Operators, 1st ed., 23–40, (2010).

[68] U. Bengtzelius, W. Gotze and A. Sjolander. Dynamics of supercooled liquids and the glass transition. *Journal of Physics C: Solid State Physics* **17**(33), 5915, (1984).

[69] P. Frolkovič. Numerical recipes: The art of scientific computing. *Acta. Appl. Math.* **19**(3), 297–299, (1990).

[70] M. Caraglio et al. An Improved Integration Scheme for Mode-Coupling-Theory Equations. *Communications in Computational Physics* **29**(2), 628–648, (2020).

[71] F. Weysser et al. Structural relaxation of polydisperse hard spheres: Comparison of the mode-coupling theory to a Langevin dynamics simulation. *Phys. Rev. E* **82**(1), 011504, (2010).

[72] I. Gohberg, S. Goldberg and M.A. Kaashoek. Basic Classes of Linear Operators. *Springer Basel AG*, 1st ed., 135–166, (2003).

Acknowledgements

This endeavor must conclude by acknowledging all those who have lent their support throughout its conception.

Initially, gratitude is extended to the supervisor, Prof. Dr. Thomas Voigtmann, whose auspicious orchestration facilitated my integration within his academic cohort. Noteworthy, however, is not only his facilitation of my group affiliation, but also his affable and propitious demeanor that I have ardently cherished over the passing years. He displayed unwavering engagement with my endeavors and particularly in the denouement, remained accessible for inquiries without temporal constraints.

Furthermore, recognition is due to Prof. Dr. Hartmut Löwen for his role as the secondary evaluator of this work.

Additionally, appreciation is reserved for the Institute of Materials Physics in Space at DLR, for the allocation of computational resources.

During my tenure at DLR, I had the privilege of acquainting myself with a plethora of esteemed colleagues. Notably, amongst them is Sebastian Steinhäuser, whose companionship during luncheon and office hours I am appreciative of. This camaraderie was accentuated by a shared disposition for refined wit. Furthermore, gratitude is extended to Leon Granz, whose recalibration of BD-simulations enriched this work by enabling a salient juxtaposition with MCT-data. His attuned ear remained receptive as I sought to convey instances of numerical breakthroughs.

Furthermore, my friends warrant acknowledgment as integral constituents of both my personal and professional odyssey. They have unfailingly extended their presence during moments of necessity, rendering my leisure time a sanctuary of reprieve from toil, and equally nurturing my enthusiasm for forthcoming endeavors. Special commendations are hereby directed towards Thomas, Niko, Dennis, Michael, and Ann-Kathrin.

Without question, the preeminent accolades are reserved for my sister, Katrin, and especially my parents, who have steadfastly bolstered me in every conceivable facet throughout my life's journey thus far.